BRNO UNIVERSITY OF TECHNOLOGY
VYSOKÉ UČENÍ TECHNICKÉ V BRNĚ

CENTRAL EUROPEAN INSTITUTE OF TECHNOLOGY BUT
STŘEDOEVROPSKÝ TECHNOLOGICKÝ INSTITUT VUT

ESTIMATION OF MECHANICAL PROPERTIES OF THIN FILMS USING NUMERICAL MODELLING OF EXPERIMENTAL TESTS

STANOVENÍ MECHANICKÝCH VLASTNOSTÍ TENKÝCH FILMŮ POMOCÍ NUMERICKÉHO MODELOVÁNÍ EXPERIMENTÁLNÍCH TESTŮ

DOCTORAL THESIS
DIZERTAČNÍ PRÁCE

AUTHOR
AUTOR PRÁCE
Hector Andres Tinoco Navarro

SUPERVISOR
ŠKOLITEL
doc. Ing. Pavel Hutař, Ph.D.

CO-SUPERVISOR
ŠKOLITEL SPECIALISTA
prof. Mgr. Tomáš Kruml, CSc.

BRNO 2022

I dedicate this dissertation to my family that always believes in my dreams

Nadie rebaje a lágrima o reproche
esta declaración de la maestría
de Dios, que con magnífica ironía
me dio a la vez los libros y la noche.

Jorge Luis Borges

ABSTRACT

Bulge testing is an experimental technique that involves the use of numerical and analytical approaches to characterize the mechanical properties of thin films. This thesis addresses some limitations found in the classical models that describe the behavior of thin films subjected to this test. This required the development of new models and numerical strategies in order to determine several mechanical properties of monolayer and bilayer thin films under different structural conditions, such as elasticity, plasticity, and fracture. By combining finite element analysis and classical analytical solutions, different methodologies for calculating the elastic properties (E and v), residual stresses, yield stress, and fracture toughness were proposed and validated. The mechanical properties of silicon nitride, aluminum, and gold films were characterized using load-deflection experimental data obtained from bulging measurements. The determined properties showed reasonable agreement with materials of known properties, which validated that the proposed methods in this work can be useful for estimating the mechanical properties of freestanding thin films.

KEYWORDS: Bulge test, thin film, finite element analysis, load-deflection, elastic properties, yield stress, fracture toughness

ABSTRAKT

Testování tenkých filmů pomocí "Bulge testu" je experimentální technika která zahrnuje použití numerických a analytických přístupů k charakterizaci mechanických vlastností tenkých vrstev. Tato práce se zabývá některými omezeními nalezenými v klasických modelech, které popisují chování tenkých vrstev podrobených tomuto testu. Za tímto účelem byly vyvinuty nové modely a numerické strategie pro stanovení různých mechanických vlastností jednovrstvých a dvouvrstvých tenkých vrstev za odlišných strukturních podmínek, jako je elasticita, plasticita a lom. Kombinací metody konečných prvků a klasických analytických řešení byly navrženy a ověřeny různé metodiky pro výpočet elastických vlastností (E a v), zbytkových napětí, meze kluzu a lomové houževnatosti. Mechanické vlastnosti filmů z nitridu křemíku, hliníku a zlata byly charakterizovány pomocí experimentálních dat o zatížení-průhybu získaných z měření. Stanovené vlastnosti vykazovaly uspokojivou shodu s což potvrdilo, že metody navržené v této práci mohou být užitečné pro odhad mechanických vlastností se známými materiálovými vlastnostmi tenkých vrstev.

KLÍČOVÁ SLOVA: Bulge, tenký film, analýza metodou konečných prvků, elastické vlastnosti, mez kluzu, Lomová houževnatost

Declaration

I declare that this thesis was written under the supervision of assoc. doc. Ing. Pavel Hutař, Ph.D., and it is an original work with cited literature and other professional sources listed in the text and reference list.

……

Hector Andres Tinoco Navarro

Acknowledgments

I would like to express my sincere appreciation for my supervisor doc. Ing. Pavel Hutař, Ph.D. for giving me the opportunity to be a part of his team. Also, I appreciate his patience, good advice, and the great human bean he is, As well as his continuous support for my Ph.D. studies and research.

Additionally, I would like to thank Prof. Mgr. Tomáš Kruml, CSc. Dr. Ph.D. for involving me in thin film research and sharing many insights about the work's development. I consider him a great person with a lot of knowledge to share.

I am extremely grateful to Universidad Autónoma de Manizales (Colombia) for allowing me to work with them while I was studying, as well as for the financial support that enabled me to participate in conferences and other research activities.

Further, I want to extend my gratitude to CENTRAL EUROPEAN INSTITUTE OF TECHNOLOGY (CEITEC – Brno University of Technology), It has been a great privilege to be part of this research center. Also, I appreciate the help that I have received from Renata Hritzová in my role as a doctoral student.

To my colleagues of Ústavu fyziky materiálů Akademie věd České republiky, Jan Poduška, Tomáš Oplt, Tomáš Vojtek, Jakub Holzer, Pavel Pokorny, Lukáš Trávníček, Pavol Dlhý, Ondrej Slávik, Radek Kubíček, Thank you for your understanding and support, as well as for sharing long laughs with me during our meetings. I am sincerely grateful.

Last but not least, I would like to thank to my family (Mery-Mother, Luis-Brother, and Kate-Sister), my son (alejandro), my daughter (Amelie), and to my wife (Jiřina) to be a constant source of inspiration and love.

Table of Contents

List of Tables 9

List of Figures 10

Chapter 1. Introduction 14

1.1 Motivation and Context 14

1.2 Thin films manufacturing 17

1.3 Manufacturing advantages of the thin films 20

1.4 Thin Film Characterization by mechanical testing 21

1.5 Bulge testing: Fundamental theory 27

1.6 Experimental setup for bulge testing 30

1.7 Statement of the problem 31

1.8 Aims of the thesis 34

1.9 Thesis outline 34

Chapter 2. Determination of the elastic properties using an experimental-numerical approach with two different bulged thin films 36

2.1 Finite element modelling of bulge test for freestanding thin films 36

2.2 Numerical approach for determining elastic properties using two thin film samples 39

2.3 Effects of Young's modulus, Poisson's ratio, residual stress and on load-deflection relation 40

2.4 Results: Young's modulus and Poisson's ratio of Si3N4 thin films with two geometries (square and rectangular) 42

Chapter 3. Determination of the elastic properties using an experimental-numerical approach with one bulged thin film 45

3.1 Finite element modeling of freestanding thin films submitted to bulge test 45

3.2 Numerical approach for determining elastic properties using one thin film sample 46

3.3 Comparisons between solution strategies presented in section 3.1 48

3.4 Identification of Young's modulus and Poisson's ratio for Si_3N_4 50

3.5 Identification of Young's modulus and Poisson's ratio of a rectangular Au thin film 52

Chapter 4. Plasticity characterization in freestanding monolayer thin films 56

4.1 Stress-strain distributions for freestanding square thin films subjected to bulge test 56

4.2 Stress-strain relations at the central point for a bulged square thin film 58

4.3 Description of the elastoplastic behaviour of square thin films 62

4.4 Comparison between stress and strain distributions in an elastic square thin film 63

4.5 Stress model (Eq. 4.23) validation for elastic square thin films 67

4.6 Elastoplastic description of square thin films using stress-strain models 68

Chapter 5. Fracture toughness evaluation of a cracked Au thin film and plasticity assessment of an Al thin film by bulge testing 71

5.1 Experimental setup for a bulge testing of Au (Gold) and Al (Aluminum) thin films 71

5.2 Stress intensity factor K_I and J-integral 72

5.3 Fracture analysis for a pre-cracked and non-cracked Au thin film 74

5.4 Nonlinear fracture results for the Au thin film 75

5.5 Plasticity analysis for an Al thin film 79

Chapter 6. Elastic properties characterization of bilayer thin films subjected to bulge test ... 83

6.1 Finite element model for a bulging test in bilayer thin films 83

6.2 Numerical strategy for determining residual stresses in bilayer thin films 85

6.3 Experimental validation for a bilayer thin film of Si3N4 (substrate) and Al subjected a bulge test 90

Chapter 7. Conclusions 96

Papers Published During the Ph.D. 98

References 101

List of Tables

Table 1.1. Values of constants C_1 and $C_2(v, a/b)$ determined by several authors

Table 2.1. Prediction of C_1 and σ_r with finite element data – square membrane 2×2 *mm*

Table 2.2. Set of parameters that satisfy the experimental data for $P(w_{\max})$ curves

Table 3.1. Determined elastic properties for silicon nitride Si_3N_4 thin films

Table 3.2. Determined elastic properties for silicon nitride silicon nitride Si_3N_4 thin film

Table 4.1. Relative errors for each size of thin film

Table 4.2. Material models

Table 5.1. Residual stress computations with known C_1 values

Table 6.1. Mechanical properties for the six numerical examples

Table 6.2. Predictions determined using the numerical strategy (proposed algorithm)

Table 6.3. Predictions determined for σ_{rA} and σ_{rB} using the numerical strategy

Table 6.4. Silicon nitride Si_3N_4 elastic properties and Al elastic estimations

Table 6.5. Silicon nitride Si_3N_4 elastic properties and Al elastic estimations for FEM models.

Table 6.6. Parameters for FEM models.

List of Figures

Figure 1.1. SEM sketch of a micro-gear Guo et al. (2009)

Figure 1.2. (a) Bulge test setup. (b) Circular Bulged membrane. This image was taken and modified from Elahi et al. (2019).

Figure 1.3. (a) Schematic of a typical CVD system with a horizontal tube reactor. (b) Higher magnification SEM micrograph of SnO2 thin film, showing each individual particle is less than 30 nm Liu et al. (2005) . (c) Cross-sectional view of SnO2 sensor Liu et al. (2005).

Figure 1.4. (a) Schematic of a typical PVD system with a horizontal tube reactor. Images (b) and (c) obtained by Gao et al. (2015) evidence SEM micrographs of the deposited material.

Figure 1.5. (a) Schematic surface micromachining process steps. (b) Single and cumulative laser cycle profiles tests Giorleo et al. (2016). (c) SEM view of an array of 10 lm wide cantilevers built in ON Laconte et al. (2004).

Figure 1.6. (a) Bulge testing scheme. (b) load deflection curve.

Figure 1.7. Typical apparatus used for bulge testing (modified scheme from original reported by Xiang et al. (2005)). Images included were taken from works published by Walmsley et al., (2007), Martins et al. (2009) and Lu et al. (2013).

Figure 1.8. (a) Steps for manufacturing a freestanding thin film. (b) Rectangular window in a silicon wafer, image provided by Peckys et al. (2009). (c) Square window in a silicon wafer, image provided by Martins et al. (2009).

Figure 1.9. (a) Finite element simulation of bulge test for a bilayer circular film, image obtained by Marandi et al. (2017) (b) Displacement field obtained by finite element analysis that illustrates a deflection of 2.68um for a quarter of a bilayer square membrane (1.2mm) under a pressure 6894 Pa (image taken from Orthner et al., 2010).

Figure 1.10. (a) Scheme of indentation process (loading and unloading). (b) Typical graph of indentation process. (c) Atomic force microscopy image of height cross-sectional (image modified and taken of Moharrami & Bull (2014) (d) Height of the demarked lines in the image c (graph taken from Moharrami & Bull (2014).

Figure 1.11. Comparison of real indentation experiments with simulations performed by FEM. (a) Image taken and modified from Eidel (2011) (simulation results show the height compared with a SEM image of the experiment). (a) Image taken and modified from Reuber et al. (2014) (simulation results show In-plane lattice rotation compared with the experiment done by Kysar et al. (2010).

Figure 1.12. (a) Scheme of a micropillar compression tests based on the image provided by Wang et al. (2016) (Finite element model of the micropillar and bulk base). (b) Deformed micropillars of Cu–Fe thin films (image obtained from Wang et al. (2016)). (c) Distribution of principal strains simulated for the Figure 1.12b (Image taken from Wang et al. (2016)).

Figure 1.13. (a) Experimental setup for bulge testing. (b) scheme of the bulge test apparatus. (c) Image of the thin film (Si_3N_4) and Si frame, section A-A. (d) reconstructed displacement field of bulged thin films.

Figure 2.1. (a) Thin film model with extension. (b) Residual stress application. (c) boundaries Γ_b and Γ_f.

Figure 2.2. (a) Rectangular thin film with extension δ . (b) Whole set including sample holder (Si substrate).
(c) Transversal section of thin film with the silicon substrate.

Figure 2.3. (a) Comparison between the model with extension and model with the substrate. (b) Convergence of the maximum relative deflection ($\delta = 0.25\%$) vs percentage of extension of the virtual boundary.

Figure 2.4. Numerical approach to determine both elastic parameter of both thin film geometries (rectangular and square).

Figure 2.5. Influence of (a) residual stress. (b) Young's modulus. (c) Poisson's ratio on load-deflection curves.

Figure 2.6. (a) Error for square thin film. (b) Error for rectangular thin film. (c) Minimum linear error for rectangular and square thin film.

Figure 2.7. Comparison between $P(w_{\max})$ experimental and numerical curves. (a) Square membrane. (b) Rectangular membrane.

Figure 3.1. (a) Bulge test, thin-film section A-A. (b) Thin-film model with extension, called FEM I model. (c) Residual stress application at the boundaries, called FEM II model.

Figure 3.2. Sequential procedure for estimating Young's modulus and Poisson's ratio.

Figure 3.3. (a) Load-deflection comparison between models represented in Figure 3.1a and 3.1b. (b) Maximum principal stress comparison for a $2.5 \times 2.5mm$ film.

Figure 3.4. Experimental measurements of the displacement field z under different pressure conditions.

Figure 3.5. (a) Error function $e_p(E,v)$. (b) RMS cubic error scheme of the experimental setup. (c) Load-deflection curve comparisons.

Figure 3.6. (a) Error function $e_p(E,v)$. (b) RMS cubic error scheme of the experimental setup. (c) Load-deflection curve comparisons.

Figure 3.7. (a) Comparison between experimental data and the linear relation P/w_0 and w_0^2 . (b) Error function with threshold in 0.6%.

Figure 3.8. (a) $e_p(E,v)$ error function. (b) Set of $e_p(E,v)$ values lower than 0.15%.

Figure 3.9. (a) E and v data set for $e_p(E,v) < 0.15\%$. (b) Error function $e_c(E,v)$ evaluated in the central sub-region.

Figure 3.10. (a) Comparisons between FEA and experimental data. (b) Load-deflection. b) Stress vs. Pressure.

Figure 4.1. (a) Scheme of a bulged square membrane represented by the displacement field $w(x,y)$ and its directional curvature radios $\rho_x(x,y)$ and $\rho_y(x,y)$. (b) Representation of the stress state at the central point of a bulged square thin film.

Figure 4.2. Differential element at the central point of a thin square film. (a) Stress state. (b) Kinematic approximations.

Figure 4.3. Linear relation obtained from the load-deflection curve.

Figure 4.4. (a) Relative displacement error between FEM II solutions and $w(x,y)$. (b) Comparison of the maximum principal stress among FEM II and the analytical solution.

Figure 4.5. (a) Comparisons between σ_1 obtained by FEM and the proposed analytical equation. (b) Maximum principal stress determined by FEM. (c) Minimum principal stresses obtained analitically. (d) Von Mises stresses determined analitically.

Figure 4.6. Calculations for $P = 9.57\ \mathrm{kN}$ a) Strain field at *x*- direction. b) Stress field at *x* - direction.

Figure 4.7. (a) Directional curvatures $\kappa_{xx}(x,y)$, $\kappa_{yy}(x,y)$ and $\kappa_{xy}(x,y)$ determined analytically. (b) Comparison among the principal curvatures.

Figure 4.8. (a) Maximum principal stress comparisons. (b) Stress comparisons for different sizes of square films.

Figure 4.9. Comparison between FEM results and analytical models. (a) Equivalent total strains at the central point. (b) Maximum principal stress at the central point.

Figure 4.10. (a) Correlations between P/w and w^2; and relative errors between Y_l and Y_{Nl} (dashed lines). (b) Predicted material models.

Figure 5.1. Experimental setup for the bulging test of the Al thin film.

Figure 5.2. Bulge test on a cracked thin film (half model).

Figure 5.3. (a) Uncertainty of the stresses at the crack tip determined by FEM. (b) Direct method for determining K_I through finite element solutions.

Figure 5.4. Scheme of the solution process by finite element analysis.

Figure 5.5. Comparisons in load-deflection curves for non-cracked and cracked film with the experimental data.

Figure 5.6. (a) Stress intensity factor through thickness obtained by ANSYS. (b) Stress intensity factor vs loading pressure.

Figure 5.7. Sequential procedure for estimating Young's modulus and Poisson's ratio.

Figure 5.8. (a) Stress in *y* direction close to the crack tip for 31.469 *kPa* . (b) Estimation of K_I values from Equation (5) for 31.469 *kPa*.

Figure 5.9. K_I values from different methods.

Figure 5.10. K_I values from different notches for both J- integral fracture methodology

Figure 5.11. (a) Example of 3D experimental displacement field, (b) Displacement fields for different pressure states.

Figure 5.12 (a) The schematics of the membrane loading in six cycles; (b) pressure – deflection curves as the central point.

Figure 5.13. (a) Pressure-stress curve for different loading cycles. (b) Scaled load-deflection relations and relative error for the third loading cycle.

Figure 5.14. (a) Stress and strain curve for different loading cycles. (b) Residual deformations after unloading cycles.

Figure 6.1. (a) Composition of a bilayer thin film. (b) residual stresses in a bilayer thin film. (c) Bulging test scheme in a bilayer thin film.

Figure 6.2. Scheme of the solution process by finite element analysis.

Figure 6.3. (a). Model of a thin film deposited on the substrate. (b) Equilibrium conditions for a differential element of the set are subjected to residual stress. (c) Kinematic conditions are imposed by the residual stresses (compatibility conditions).

Figure 6.4. (a). Model of a thin film deposited on the substrate. (b) Equilibrium conditions for a differential element of the set are subjected to residual stress. (c) Kinematic conditions are imposed by the residual stresses (compatibility conditions).

Figure 6.5. (a). Load-deflection data for three samples (Si3N4/ Al). (b) Measured deflection surface.

Figure 6.6. (a) Finite element approximations for the Sample 1. (b) Root mean square deviation for the FEA approximations for Sample1.

Figure 6.7. (a) Finite element approximations for Sample 1. (b) Non-absolute relative error for the FEA approximations for sample 1.

Figure 6.8. (a) Finite element approximations for the Sample 2. (b) Maximum principal stress in the central point for Al. (c) Maximum principal stress in the central point for Si3N4.

Chapter 1. Introduction

1.1 Motivation and Context

In the last few decades, the engineering applications of modern technology have led to the miniaturization of mechanical elements made up of materials with unique properties (see Figure 1.1), particularly thin films (Prins et al. 1996; Mitzi, 2001; Green, 2007; Mattevi et al., 2011; Eom & Trolier-McKinstry, 2012). In the development of several engineering fields such as microelectronics (integrated circuits), microelectromechanical systems (MEMS), nano-devices, coating applications, biomedical devices, thin films are applied (Ezhilvalavan & Tseng, 1999; Fu et al., 2004; Charitidis, 2010). During the manufacturing process or its application, the mechanical loading conditions on the films can play a crucial role in lifetime prediction. The thickness of a thin film can vary from the nanometric scale to the micrometric scale, it means that failure mechanisms due to the microstructure can be affected by the size effect. Thereby, it is crucial to understand the microstructure and mechanical properties to ensure reliability and lifetime, since these present different properties from bulk materials.

Thin films manufacturing (chemical vapor deposition, physical vapor deposition, micromachining, and others) involves demanding instrumentation to achieve dimensional and mechanical conditions which should be controlled depending on the industrial applications; for this purpose, different materials such as metals are used, for example, semiconductors and dielectric materials (Ohring, 2001; Setter et al., 2006; Charitidis, 2010). However, evaluating the mechanical properties is a difficult task since the materials in small dimensions restrict the implementation of standardized tests appropriate for bulk specimens.

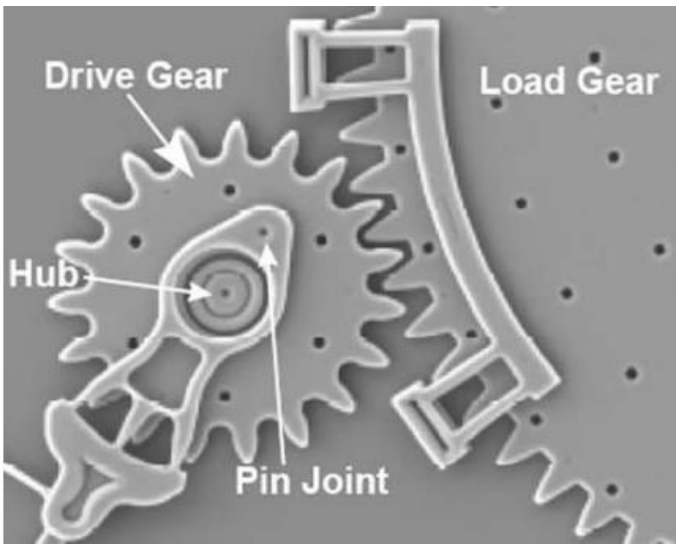

Figure 1.1. SEM sketch of a micro-gear Guo et al. (2009)

Several experimental techniques to determine the mechanical properties of thin films have been developed; among them deflection techniques, nanoindentation, diffraction-based techniques, Raman spectroscopy, etc. (Mitchell et al., 2003; Poelma et al., 2011). The relative advantages and

disadvantages of all the methods and techniques mentioned have been discussed in the literature (Nix, 1989; Huang et al., 2007; Zhang et al., 2015). Nevertheless, some mechanical tests are highlighted; one of these is the bulge testing, a deflection technique that has been well-accepted to characterize the mechanical properties of thin films. The advantages of this technique are given by its easy experimental implementation, monitoring of the transverse loading over the film, and the use of simplified analytical models dependent on the maximum deflection resulting from the bulged process. On the other hand, some disadvantages can be mentioned as uncertainties in the computation of mechanical properties and constant calculations since its values differ among authors.

The bulge testing technique is based on applying gas or liquid pressure to deflect a membrane with the aim to produce a bulged region (Sheng et al. 2017; Lu et al., 2013) as shown in Figure 1.2. The relation between pressure and curvature of the membrane is called load-deflection dependence. It was described by Beams (1959) in 1959 in one of the first models performed for a semi-spherical membrane made with gold and silver. However, the models exhibited several limitations in identifying properties that were contrasted and analyzed numerically via finite element analysis by Small & Nix (1992). Tabata et al. (1989) reported an analytical model for rectangular films, but Vlassak & Nix (1992) developed new expressions obtained from the energy minimization technique to describe the bulge test in rectangular and square membranes. They showed that Young's modulus and residual stress can be obtained by applying least-square regression with experimental data in a simple way. Also, Poisson's ratio was determined from two different membranes with a sufficiently large aspect ratio between them. The constants involved in the mathematical models are computed by analytical solutions (Tabata et al., 1989; Vlassak & Nix, 1992) and finite element approximations (Pan et al., 1990). These solutions provided a reliable basis for determining elastic properties from load-deflection curves since the properties obtained analytically can be inaccurate by selecting input parameters. Maier-Schneider et al. (1995) confirmed the results obtained by Pan et al. (1990), showing that some parameters determined analytically were not computed accurately, which led to higher differences between experimental and calculated curves. Both approaches (i.e. analytical and numerical) presented advantages and limitations for the characterization of elastic properties using bulge testing. But, according to the bulging theory, the Load-deflection model shows that Young's modulus and Poisson's ratio are coupled, which means that different pairs of solutions (E and ν) satisfy the experimental results with great exactness. It indicates that in a traditional bulge testing analysis, only a combination of these two elastic properties could be determined; therefore, there is not a unique solution to solve the problem. This can be verified from the analytical Equation by the number of independent parameters involved if both elastic parameters are unknown. In this sense, there is an opportunity to improve the current elastic-plastic models or the methodology for characterizing mechanical properties (Maier-Schneider et al., 1995, Xiang et al., 2005, Schweitzer & Göken 2007). This means to calculate other mechanical parameters evidenced in the plasticity (Xiang & Vlassak, 2006; Nicola et al., 2006), buckling (Mei et al., 2007; Ghanem et al., 2017), and fracture (Merle & Göken, 2011; Preiß et al., 2017).

Analytical solutions are more suitable for evaluating properties by their simplicity; however, the development of new models was interrupted by the expansion of finite element solutions in the last decades. Finite Element Method (FEM) is a powerful tool that has been widely applied in engineering, which allows performing parametric studies with great accuracy. In the case of bulge tests, several

studies have shown its applications in the analysis of thin films (Mitchell et al., 2003; Xiang, et al., 2005; Paul & Gaspar 2007; Yanfei, et al., 2017). The disadvantage of using FEM is the time-demand in the computations and the scalability for a high number of experiments that will need to be reproduced.

The simulation of the bulge testing by finite element analysis appears to be that is not a difficult task by the conditions of the bulging problem since the geometry of the thin films usually are regular, which allows reducing the size of the models by the symmetries. This reduction positively impacts the calculations because the number of elements is minimized considerably. Additionally, the boundary conditions are delimited to applying fixed support, residual stress, and internal pressure. The determination of the elastic properties is carried out through a reversal engineering process, which means that the bulging experiments are reproduced in the simulations or these are determines by equations, as in the case of analytical solutions. Many authors developed FEM simulations in their studies (Pan et al., 1990; Maier-Schneider et al.,1995; Santos et al., 2010; Shafqat et al, 2018; Rontu et al.; 2018), but the procedure details are not precisely described, which is not a guarantee of obtaining unique solutions for the problem. As discussed before, different combinations of *E* and *v* can reproduce the same load-deflection curve since the bulging analysis is a mechanically coupled problem. However. The challenge is to determine the pair of elastic parameter that satisfies the kinematic of the film, which is experimentally characterized.

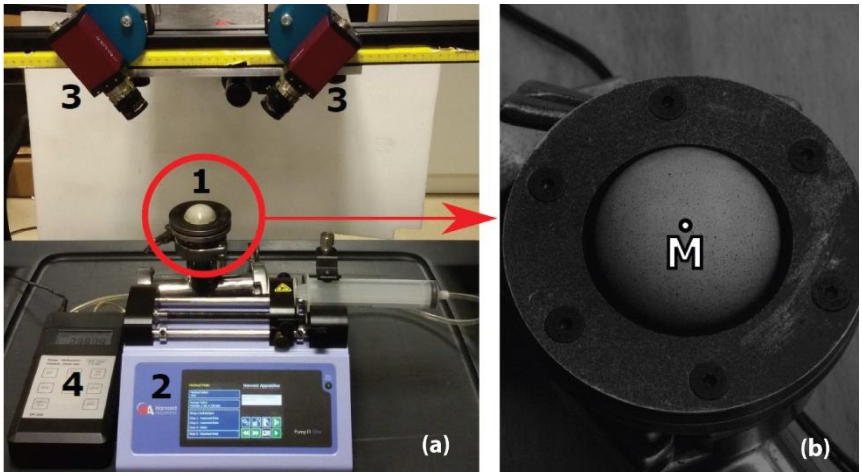

Figure 1.2. (a) Bulge test setup. (b) Circular Bulged membrane. This image was taken and modified from Elahi et al. (2019)

The present thesis focuses on consolidating several numerical methods to determine the mechanical properties of thin films by applying bulge testing, analytical solutions, and finite element analysis. The following main topics were developed in this thesis:

- Two different numerical approaches are presented and assessed to estimate a set of optimal solutions for the elastic properties (E and v), which can be computed using two thin films with different geometries (square and rectangular) or using each experimental data set by separated.
- For square thin films, equations to represent the equi-biaxial stress state (central point) for freestanding square thin films were developed, applied, and validated with

experimental data. In order to validate the applicability of the proposed equations, numerical and experimental data were presented for the linear elastic analysis, and two examples were developed to characterize elastoplastic behavior (bilinear and nonlinear) from load-deflection curves.

- Calculations of the fracture toughness were carried in pre-cracked thin films applying solutions based on sub modeling of finite element analysis. The problem was divided into two stages; the first stage was developing the numerical model on the whole film without pre-crack (elasto-plastic analysis), and the second stage was performed on a film portion that included the pre-crack (sub-modeling stage). Three different notches (rounded, sharp, and V-sharp) were applied to calculate the stress intensity factor around the crack tip using path independent J-integral.
- A methodology to detect plasticity and estimate the yield stress from bulge testing using finite element analysis was developed. The methods to determine the plasticity parameters are based on the load-deflection relation that presents a linear behavior in the elastic regime when scaled with the displacement parameter. The plastic deformation induces nonlinear effects that allow determining the elastic limit of the film, as demonstrated in our research.
- For the Bi-layer thin films, the calculations of the elastic and plastic properties were developed to understand the effects of the substrate over the second deposited thin film. Again, bulging experimental data were used as input parameters.

1.2 Thin films manufacturing

The development of new technologies in the last years and the high demands by the applications from industries of semiconductors, micro-electromechanical systems (MEMS), surface engineering, microelectronics have boosted the advance of new materials in the shape of thin films as well the understanding of its behavior in micro-scale, and nanoscale. The thin films can be defined as structures made of solid layers of a material which presents in one direction a thin thickness (micro and nano) in comparison with the other directions that can be in orders of magnitude of millimeters. There are different processes for manufacturing these structures onto substrates; these produce films with thickness from a few microns until atomic scale (Leskelä & Ritala, 2002; Huang et al. 2004; Puma et al., 2008). A critical characteristic of the thin films is the difference in the physical properties between three-dimensional (bulk shape) and (thin film shape) two-dimensional states of matter, for example, the variation in the conductivity, changes in thermodynamic properties, or the chemical reactivity, which can be in function of the thickness.

In this section, preparation techniques of thin films are discussed and divided into three main processes, as follows: chemical vapor deposition (CVD), physical vapor deposition (PVD), and micromaching.

1.2.1 Chemical vapor deposition (CVD)

Thin films obtained by Chemical Vapor Deposition (CVD) are manufactured from a chemical reaction between a substrate and a gas or by two gases, as shown in the scheme of Figure 1.3. In this process,

two typical chemical reactions are produced, which are oxidation or nitridation. As a result of these processes, the thermo-physical-chemical conditions determine the final membrane properties (Puma et al. 2008; Kim et al., 2011; Liu et al., 2015).

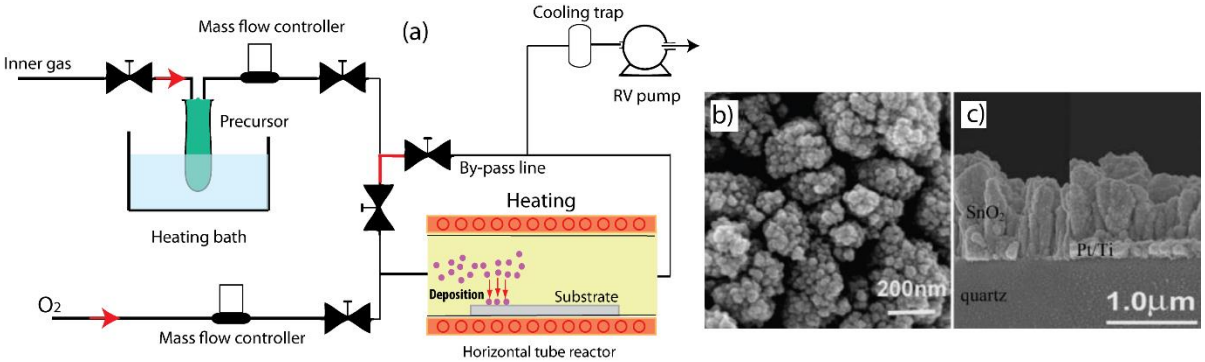

Figure 1.3. (a) Schematic of a typical CVD system with a horizontal tube reactor. (b) Higher magnification SEM micrograph of SnO2 thin film, showing each individual particle is less than 30 nm Liu et al. (2005) . (c) Cross-sectional view of SnO2 sensor Liu et al. (2005).

The technique is based on the deposition of chemical reactants in the vapor phase on the surface of a thermal heated solid substrate to achieve the continuous growth of a solid membrane. By using a CVD process; amorphous, poly- or single crystalline or epitaxial thin films can be deposited respectively (Obraztsov et al.,2007; Wang et al., 2014)

In low pressure (lower than 1 bar), there are obtained films with a low density of defects and uniform thickness. In the case of Plasma Enhanced, the deposition rate at low-temperature increases caused by the reaction with plasma. Both processes yield materials with an amorphous structure (Puma et al. 2008; Larsen, 2015).

Figure 1.3a shows characteristic equipment used in the CVD process, which is composed of a chemical precursor source (gas, liquid or solid), a gas transport line, a thin film growth chamber, a gas dispersion shower, a substrate (wafer); as well as different thermomechanical devices as valves, vacuum pumps, mass flow controller (MFC), a chemical trapping equipment and other elements (Morosanu, 2016).

Thin films produced by CVD are extensively studied due to a considerable number of applications and properties; for example, materials as titanium aluminum nitride (TiAlN material, see Das et al., 2017) presents optimum hardness, wear resistance, higher corrosion strength, low thermal expansion and high conductivity in the shape of the thin film. Important materials as Graphene and others applied in solar cells are obtained via CVD. In the semiconductor industry, CVD processes are used to synthesize 2D materials.

1.2.2 Physical vapor deposition (PVD)

Physical Vapor Deposition (PVD) is a technique to synthesize thin films (material in layers) using an intense energy input into a pure solid material to form a vapor that can be condensed in layers on a

substrate in ultra-high vacuum (UHV). UHV refers to pressures that are on the order of 1 x 10-8 Torr or less. Vacuum is one of the essential parts in the fabrication process of thin films by PVD. Different PVD processes are commonly used, as sputter deposition, arc vapor deposition, vacuum evaporation, and ion plating (Hagerty, 2016; Gao et al., 2015).

In PVD processes, atoms or molecules are ejected from a target material (solid or liquid) through bombarded energetic particles. Figure 1.4a illustrates a schematic drawing of a sputtering system inside a vacuum chamber connected with the exterior by electrodes. Typically, the chamber walls act as an anode, whereas a target, made of the material to be deposited (see figures 1.4b and 1.4c), is connected to the negative terminal of a power supply and serves as the cathode (Reichelt & Jiang, 1990). The object to be coated (the substrate) is placed in front of the target. The substrate can be biased or at a floating potential. An inert working gas such as Argon is introduced into the chamber to form plasma. The Ions of the active gas are accelerated towards the target by the electric field between the electrodes (Mattox, 2010).

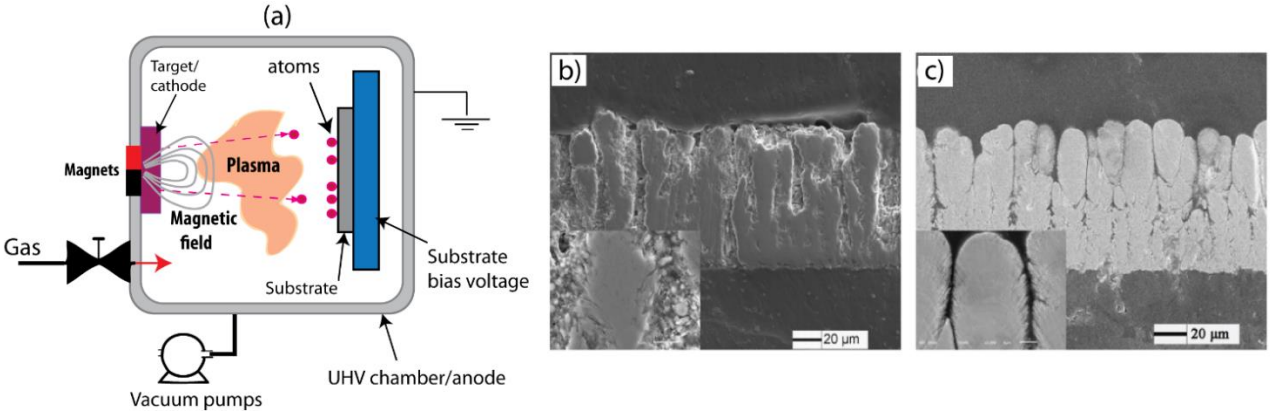

Figure 1.4. (a) Schematic of a typical PVD system with a horizontal tube reactor. Images (b) and (c) obtained by Gao et al. (2015) evidence SEM micrographs of the deposited material.

1.2.3 Micromachining

Micromachining is a technique used to manufacture and modify thin films utilizing ultrafast lasers. These are employed to perform high precision surface micromachining and 3D internal structural modification in different dimensional scales (Giorleo et al., 2016; Pecholt et al., 2008). Figure 1.5a illustrates a scheme of the process of surface micromachining.

Ultrahigh laser intensity is able to produce localized material ablation in ultrashort timescale modifying the superficial and internal shape of a structure composed of thin layers. In principle, micromachining deals with adding layers onto a wafer surface that is marked to carry out a sacrificial etch step to release a miniaturized functional device that becomes a freestanding structure. In the process, the laser removes material through the thickness of the films minimizing the thermal impact on the sacrificial layers, the substrate, and adjacent films (Giorleo et al. 2016; Laconte et al. 2004). Due to the short time that the laser is applied, the heat accumulated in the substrate is proportional to the irradiation time.

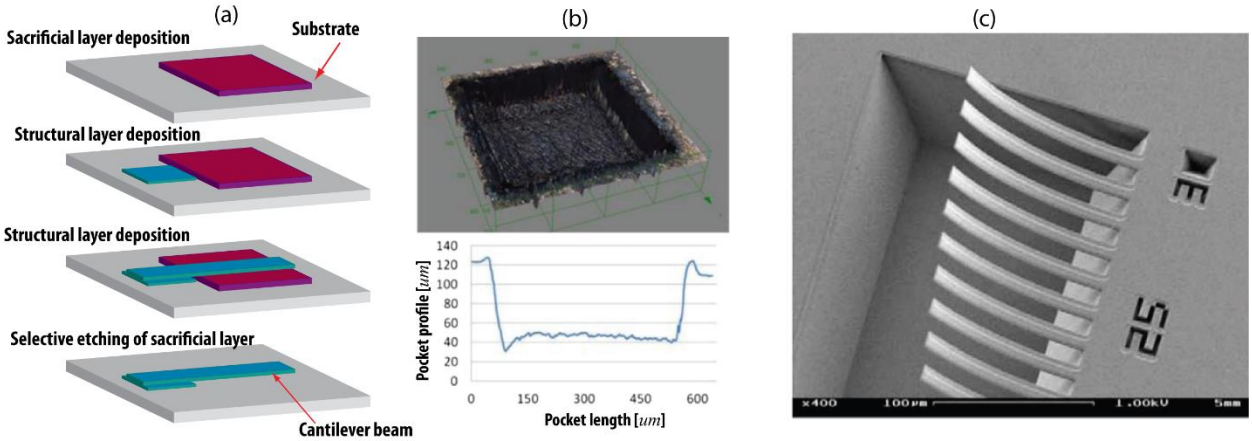

Figure 1.5. (a) Schematic surface micromachining process steps. (b) Single and cumulative laser cycle profiles tests Giorleo et al. (2016). (c) SEM view of an array of 10 lm wide cantilevers built in ON Laconte et al. (2004)

The irradiation time of the laser can be controlled employing a fast beam motion which can be applied either in continuous wave (CW) or pulsed mode. A broad spectrum of materials can be processed by surface micromachining as polymers, glasses, ceramics, metals, and alloys used as either structural, sacrificial or electrical (conductive and insulative). Two examples are shown in Figure 1.5b and 1.5c. Some processing requirements are necessary for the application of micromachining; these are; material processing compatibility, mechanical integrity between layers, and etch selectivity. Different surface or bulk micro-machining processes are mainly based on lithography, chemical or plasma etching, printing, and molding (Linder et al., 1992; Kim & Meng, 2015).

1.3 Manufacturing advantages of the thin films

Thin films in comparison in comparison with bulk materials, present some unique advantages, for instance:

- Electrical properties such as ferroelectric, piezoelectric, and magnetostrictive can be modified at the nanoscale since the coupling mechanisms can be controlled through the dimensions.
- Thin films can be deposited to create composites materials with the advantage of avoiding interface losses as in the bulk form.
- Thin films can be created by combining different structures with crystal lattices very similar, which generates composite films with superlattices. The development of these structures helps to understand the physical coupling at the atomic scale (electro-mechanical, thermo-mechanical, magneto-electrical, among others.)
- Thin films allow a better comprehension of the optical effects of the materials by the dimensional control of the manufacturing process.
- Properties such as ruggedness, durability, and excellent electronic properties are one of the best advantages of thin films.

1.4 Thin Film Characterization by mechanical testing

In the structural design of micro- or nano-devices, the material properties represent a fundamental issue for describing the behavior of these small-scale structures. During the last decades, different experimental techniques have been developed with the aim to characterize the mechanical properties of thin films, which are briefly explained in this section.

1.4.1 Bulge testing

The bulge testing is a technique used to calculate some mechanical properties of thin films, such as Young's modulus, Poisson's ratio, residual stresses, fracture toughness, creep, among other properties (Xiang, & Vlassak, 2006; Zhou et al, 2008; Merle & Göken, 2011; Yanfei et al., 2017). In principle, it consists in applying a uniform pressure over one side of a freestanding thin film window which causes a deflection outwards represented by non-uniform curvature as depicted in Figure 1.6a. The relation of both physical quantities is commonly called in the literature as load-deflection relation which is governed by the residual stresses and the elasticity, as shown in Figure 1.6b.

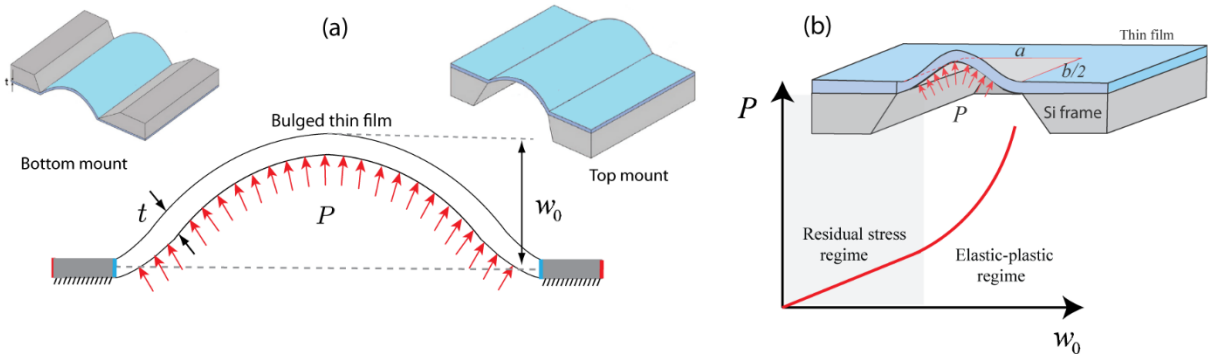

Figure 1.6. (a) Bulge testing scheme. (b) load deflection curve

Circular and rectangular membranes (particular aspect ratio) have been extensively employed in the bulge test applications since the bulged films present an approximated curvature similar to the curvature of a hemispherical cap (Rontu et al., 2018) and an infinite cylinder (Marandi et al., 2017). Therefore, the stresses and strains are calculated on the maximum deflection point (w_0) with simplified equations. Applications on square thin films are not popular since simplified models for stresses and strains are not available, and their computations have been determined through finite element analysis.

Bulge testing was described and reported as an experimental method by Beams (1959), which is considered as one of pioneer's work done in the mechanical properties identification of thin films (gold and silver). Nevertheless, in the beginning, the bulge test presented some limitations due to the problems associated with the sample processing, handling, and data analysis as discussed by Xiang et al. (2005), nevertheless with all this, it is considered as one of the earliest micromechanical tests (Tabata et al., 1989; Vlassak and Nix, 1992; Maier-Schneider et al., 1995).

All technical difficulties were overcome through time by using sophisticated equipment with which high accuracy measurements can be obtained currently (Min et al., 2017; Shafqat et al., 2018). In Figure 1.7 is illustrated a typical scheme of the necessary elements to carry out bulge testing. Almost

all bulge test apparatus is designed with the following principal elements; a sample holder, a pressure system, a deflection measurement system, and a data acquisition system (Tabata al., 1989; Xiang et al., 2005; Walmsley et al., 2007). The pressure system is controlled by an actuator or a control valve that introduces liquid or gas in a pressure chamber to get a differential pressure over the thin film. Additionally, optical methods are the most commonly used techniques to quantify membrane deflections. Deflections are measured by interferometric systems that use He/Ne laser as a light source to determine through a single-mode optical Newton interference fringes detected by a CCD camera as illustrated in the displacement field in Figure 1.7 (Walmsley et al., 2007). Other techniques use systems based on high-resolution optical profilometry (Ghazi & Kysar, 2016, Shafqat et al., 2018), among others (Schweitzer & Göken, 2007; Vucetic et al., 2011; Min et al., 2017). Additionally, in Figure 1.7, there are presented typical experimental curves of load-deflection.

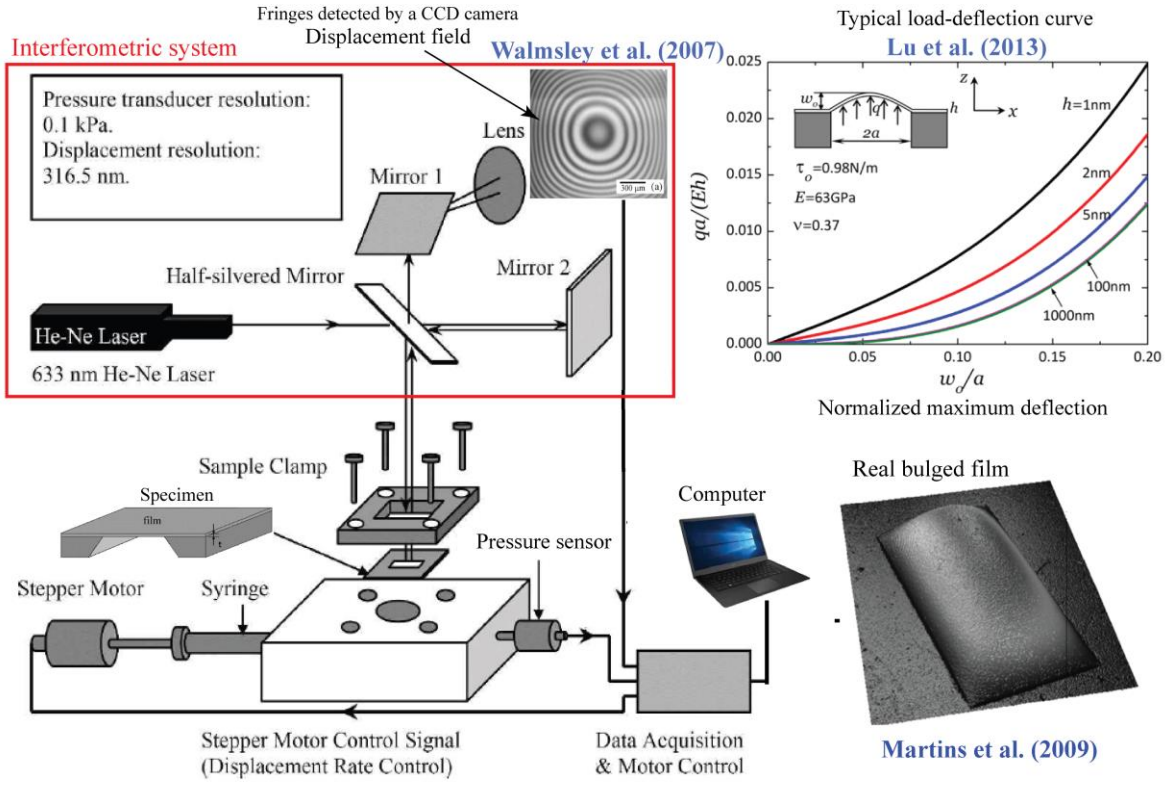

Figure 1.7. Typical apparatus used for bulge testing (modified scheme from original reported by Xiang et al. (2005)). Images included were taken from works published by Walmsley et al., (2007), Martins et al. (2009) and Lu et al. (2013).

In most cases, Silicon nitride (Si_3N_x) is coated and used as the main substrate, and it is a thin material layer deposited on top or bottom of the Si wafer. In Figure 1.8a, there are described the basic steps for producing a freestanding thin film of Si3Nx. In the last step, Si wafer is anisotropically back etched through its thickness to obtain a typical window in the sample, as shown in figures 1.8b and 1.8c. To produce multilayer thin films are applied the same procedures, only that the deposition is carried out with different materials.

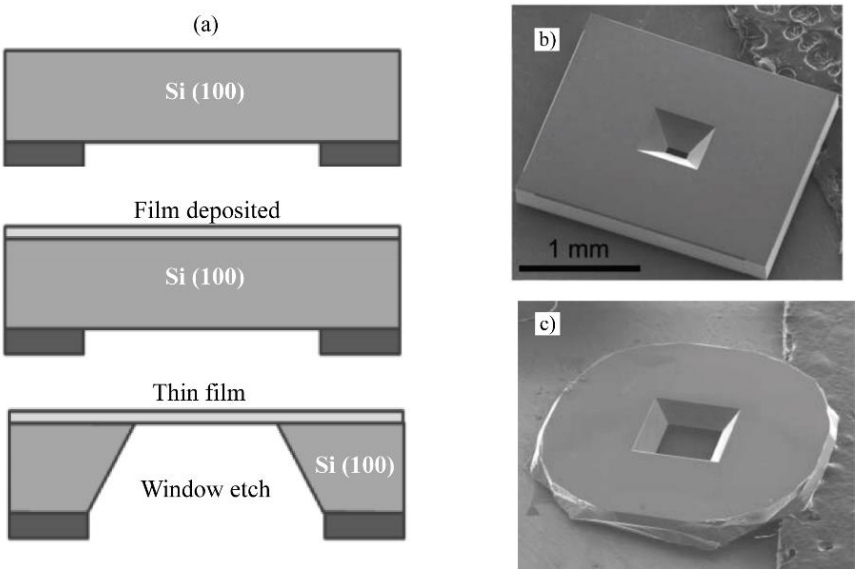

Figure 1.8. (a) Steps for manufacturing a freestanding thin film. (b) Rectangular window in a silicon wafer, image provided by Peckys et al. (2009). (c) Square window in a silicon wafer, image provided by Martins et al. (2009).

Freestanding thin films are prepared to apply standard procedures (Ghazi & Kysar, 2016) of deposition (see section 1.2) that are applied over Silicon wafers with (100) orientation usually (Xiang et al. 2005).

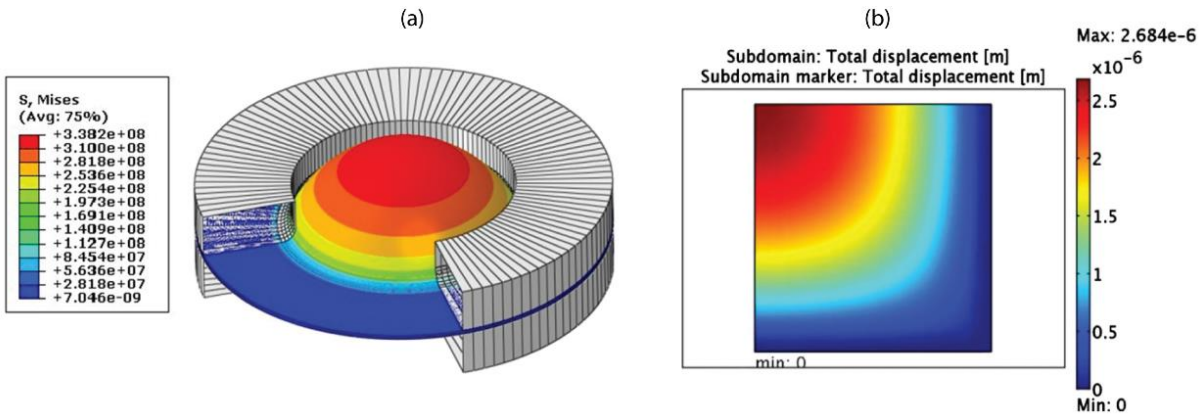

Figure 1.9. (a) Finite element simulation of bulge test for a bilayer circular film, image obtained by Marandi et al. (2017) (b) Displacement field obtained by finite element analysis that illustrates a deflection of 2.68*um* for a quarter of a bilayer square membrane (1.2mm) under a pressure 6894 Pa (image taken from Orthner et al., 2010)

Finite element method (FEM) has been extensively used to characterize mechanical properties of bulk materials, but in bulge testing (thin films see Figure 1.9) the analysis has been focused on the validation of the analytical models and experiments (Vlassak & Nix, 1992, Maier-Schneider et al. 1995, Xiang et al. 2005). It means that finite element analysis is carried out with the identified properties, this have led to realizing simplified correlations among the numerical and experimental results (Orthner et al., 2010; Zhang et al., 2015; Sheng et al., 2017). The identification of mechanical properties by FEM is not an easy task since the calculations require iterative procedures that should satisfy the experiments if the properties are unknown. Another relevant aspect that has been ignored in thin films bulging problem is the elastic coupling between Young's modulus and Poisson's ratio. Since one of these parameters should be known traditionally, this point is considered a limitation for the numerical and theoretical analysis.

1.4.2 Nano and micro indentation

Nanoindentation and micro-indentation are techniques used to determine elastoplastic and time-dependent mechanical properties in small material volumes, in bulk form, and in thin films (Xu & Rowcliffe, 2004). The principle of the technique is to perform a penetration depth on the material with a marker by means of a controlled load (see the scheme of Figure 1.10a). When the load is removed gradually, the load-displacement relation exhibits the stiffness of the material. The applied forces can have an order of magnitude in micro or nano newton and displacements in micro, nano, or angstrom.

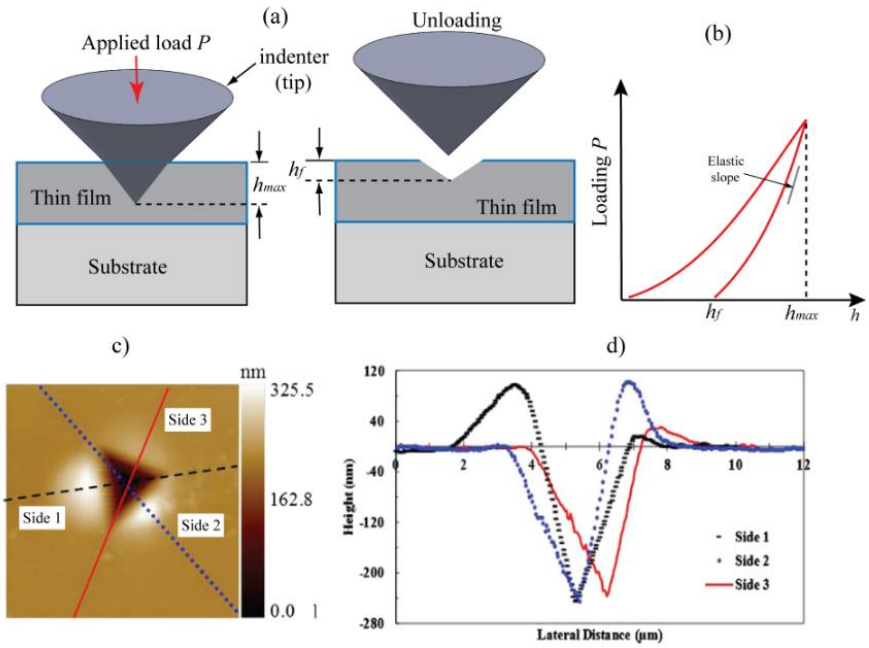

Figure 1.10. (a) Scheme of indentation process (loading and unloading). (b) Typical graph of indentation process. (c) Atomic force microscopy image of height cross-sectional (image modified and taken of Moharrami & Bull (2014) (d) Height of the demarked lines in the image c (graph taken from Moharrami & Bull (2014).

During the loading application, the material undergoes both elastic and plastic deformations as illustrated in the schemes of figures 1.10a and 1.10b. The penetration of the material is made with an instrument called indenter (tip) that can support the applied loads without remaining with permanent strains. The indenter can have different geometries as pyramidal (Berkovich or Vickers, see Figure 1,10c and 1,10d), spherical, conical, and cylindrical (Díez-Pascual et al., 2015). The indentation tests present some advantages with respect to the traditional tests done in bulk materials since they allow in situ testing of mechanical properties (Haggag, 1993; Deuschle et al., 2008; Prevost et al. 2011). In addition, the relative simplicity of the experimental setup, which is based mainly in an indenter, position control, load and displacements sensors, and a data acquisition system can be considered a favorable point in the implementation. Different approaches have been applied to analyze the mechanical properties of the load-displacement measurements (Doerner & Nix 1986, Pharr et al., 1992). Several models have been proposed to determine the substrate effects for deriving the film properties from the experimental data. However, Oliver & Pharr (1992) published the most used method, which is considered a standard procedure for determining the hardness and elastic modulus; this work was originally based on the research done by Doerner & Nix (1986). The theory considers

that the maximum loading point of the curve is used to determine the hardness, and the elastic property is computed from the unloading curve. The hardness (H) is defined as the mean pressure under the indenter (Huang & Pelegri, 2006)

$$H = \frac{P_{\max}}{A_c}, \tag{1.1}$$

where $P_{\max}$ is the maximum load and curvature of the membrane and A_c is the projected contact area of the indenter tip with the material. The contact area is calculated from the geometry of the tip, which can be pyramidal, spherical, conical, or cylindrical. To determine the elastic properties, the initial slope (dP/dh) of the unloading curve (labelled as elastic slope in Figure 1.10b) is used for the calculations. Since the unloading only relates to the elastic response of the system, which is composed of contributions from the indenter, film, and substrate. If the frame compliance is taken into account, the reduced modulus E_r can be calculated as (Doerner & Nix, 1986, Pharr et al., 1992)

$$E_r = \beta \frac{\sqrt{\pi}}{2\sqrt{A_c}} S, \tag{1.2}$$

In which $S = dP/dh$ is the contact stiffness. This parameter reflects elastic response of the system and it can be written in general form as

$$E_r = f(E_i, E_f, E_s, v_i, v_f, v_s, h, t), \tag{1.3}$$

where subscripts i, f, s refer to indenter, film and substrate, respectively. Different assumptions have been proposed to distribute the reduced modulus among elastic contributions done by the indenter, film, and substrate with the aim to extract the elastic modulus of the thin film. A wide review of literature that shows different considerations and analytical formulas was detailed by Wei et al. (2009).

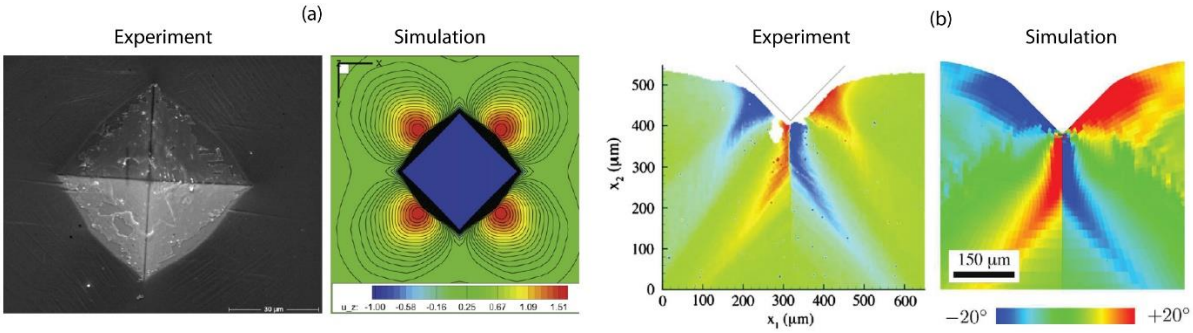

Figure 1.11. Comparison of real indentation experiments with simulations performed by FEM. (a) Image taken and modified from Eidel (2011) (simulation results show the height compared with a SEM image of the experiment). (a) Image taken and modified from Reuber et al. (2014) (simulation results show In-plane lattice rotation compared with the experiment done by Kysar et al. (2010).

Finite element simulation is an appreciable method to describe indentation problem as it has been reported in different papers (Gan et al., 1996; Kysar et al., 2010, Eidel, 2011; Reuber et al. 2014) in the last two decades. FEM has been conducted for different purposes as to study substrate effects on the measurement of the mechanical properties of thin films (Xu & Rowcliffe, 2004), to investigate the

complex stress and strain fields produced by indenter tip (Marchiori et al, 2016), and to identify the mechanical properties of the thin films among others (Alaboodi & Hussain, 2017). Figure 1.11 shows a comparison of real indentation experiments with simulations performed by FEM depending on the numerical approach these approximations can be close to the real mechanical behavior of the indentation.

Indentation presents some limitations as other methodologies applied in the mechanical properties identification, as is the case of the bulge test. Poisson's ratios of the thin film and substrate are not explicitly given (unknown) in the majority of cases, and these are chosen from the properties of the bulk materials. Therefore, a combination of methods has been implemented to overcome this difficulty (Huang & Pelegri, 2006; Alaboodi & Hussain, 2017).

1.4.3 Micropillar compression test

Micropillar compression test is a technique based on the compression of a micro non-cylindrical column that is submitted to controlled loads used to investigate the mechanical behaviour of materials in the micro scale (Bei et al., 2008; Xiao et al. 2017), in Figure 1.12a is illustrated a basic scheme of the test. The size of the micropillar presents a significant role in the stress distributions, and therefore the length should be well defined to avoid bending effects. For other applications, the size of the diameter is reduced to improve the yield effects, and flow stresses (Dimiduk et al. 2005; Shan et al. 2008) since the area decreasing produces higher stresses.

The main element for the test is the fabrication of the micropillars; Uchic et al. (2002) introduced a process applying focused ion beam (FIB) milling, and this has been implemented and improved during the last few years (Grieveson et al 2012; Xiao et al. 2017). One example of a micropillar produced by a FIB process is illustrated in Figure 1.12b. For the force application on the micropillar, traditional nanoindentation devices are used for this purpose. With controlled forces, nominal homogeneous stress states can be developed through the pillar. This is considered an advantage versus to the nanoindentation test since the sharp indenter tip generates nonuniform stress states. This technique has opened up different study routes for the understanding mechanical behaviour of single-crystal metals, nanocrystalline materials, metallic alloys, and multilayer composites.

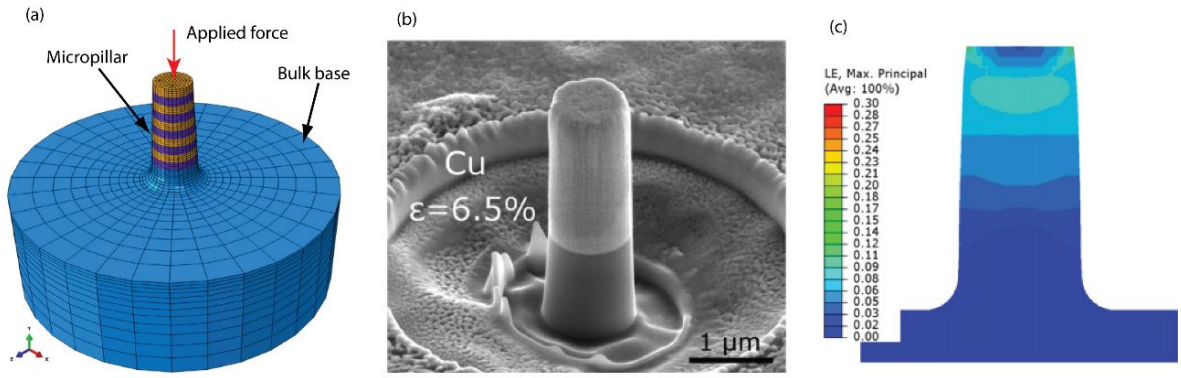

Figure 1.12. (a) Scheme of a micropillar compression tests based on the image provided by Wang et al. (2016) (Finite element model of the micropillar and bulk base). (b) Deformed micropillars of Cu–Fe thin films (image obtained from Wang et al. (2016)). (c) Distribution of principal strains simulated for the Figure 1.12b (Image taken from Wang et al. (2016)).

Finite element models have been developed to simulate micropillar compression tests in order to obtain characteristic information about the material behaviour as well the distribution of strain gradients inside the micropillars as shown in Figure 1.12c (Wang et al., 2016).

1.5 Bulge testing: Fundamental theory

From pressure and maximum displacements measurements determined in the bulge test, it is possible to estimate stresses and strains localized in the maximum deflection zone. The beam theory, and plate and shell theories are commonly used to relate the applied pressure with the maximum deflection w_0 measured. For this purpose, let's consider a thin film (rectangular geometry $2a \times 2b$, where $a \geq b$; circular geometry r) pre-stressed by residual stress σ_r and made of an isotropic elastic material that fulfills a linear stress–strain relationship. Under pressure *P*, the shape of the film is defined by the bulged surface. In those conditions, a classical analytical solution that relates the maximum deflection w_0 and pressure *P* was established in the following way (Beams, 1959; Tabata et al. 1989; Maier-Schneider et al. 1995; Xiang et al. 2005)

$$P = C_1 \frac{\sigma_r t}{a^2} w_0 + C_2(v, a/b) \frac{Et}{a^4} w_0^3, \tag{1.4}$$

Where C_1 and $C_2(v, a/b)$ are constants that depend on the geometry and material parameters, represent the residual stress induced in the deposition process, t the thickness, and E Young's modulus. Different models and numerical estimations have been proposed for both C_1 and $C_2(v, a/b)$ constants as described by Vlassak & Nix (1992), Maier-Schneider et al. (1995), Xiang et al. (2005), Schweitzer & Göken (2007) among other studies. From the theory analytical expressions have been proposed for both constants, which can be generalized by the following expression

$$C_2(v, a/b) = (\alpha + \beta v)/(1 - v), \tag{1.5}$$

Equation (1.5) depends on Poisson's ratio v; where α and β are parameters to be determined, different authors have proposed different constants for known geometries (Mitchell et al., 2003; Xiang, et al., 2005) and others have determined these with finite element analysis (Pan et al., 1990; Maier-Schneider et al. 1995). In the particular case of rectangular films, there are three cases to consider: square films, rectangular films with aspect ratio $b \leq 4a$ **,** and infinite long thin films $b \geq 4a$**.** Vlassak and Nix (1992) demonstrated experimentally that the rectangular thin films with aspect ratio $b \geq 4a$ present the behavior of an infinite film along the length. In Table 1.1 are listed the values assumed by several authors for square thin films and rectangular films with infinite long at the b-direction. The reported values show a discrepancy between constants, demonstrating that there is no unique solution in determining the elastic properties. This coincides with a discussion written by Delfani (2018) for circular films subjected to the bulge test; In his paper also there are listed some constants (including his contribution), other constants were reported by Mitchell et al. (2003).

Table 1.1. Values of constants C_1 and $C_2(v, a/b)$ determined by several authors

Square thin Film		**Rectangular thin film** $b \geq 4a$		**References**
C_1	$C_2(v, a/b)$	C_1	$C_2(v, a/b)$	
3.044	1.473-0.4 v	1.61	0.75-0.442 v	Tabata et al. (1989)

3.41	1.981-0.585 ν	---	---	Pan et al. (1990)
3.393	1/(0.8-0.062 ν)^3	2	4/3(1+ ν)	Vlassak & Nix (1992)
3.45	1.994-0.54 ν	---	---	Maier-Schneider et al. (1995)
3.42	1.91(1-0.207 ν)	---	---	Bonnotte et al. (1997)
3.56	2.03-0.568 ν	2.1	1.994-0.54 ν	Youssef (2011)

In the real applications, experimental data obtained for w_0 and P are adjusted by the least-square regression method to calculate σ_r, E and some cases ν (Karimi et al., 1997; Martins et al., 2009; Huang et al., 2018). In other situations, the deflection and pressure data are used to estimate C_1 and $C_2(v, a/b)$ constants. Beyond that, in the bulging problem, the coupling between Young's modulus and Poisson's ratio has been neglected in the load-deflection analysis. One of the parameters is usually fixed to estimate the other elastic property, as demonstrated by Tinoco et al. (2018). To overcome these challenges, The combination of the analytical model with finite element analysis shows that both elastic parameters could be determined with better accuracy.

The load-deflection model shown in Equation (1.4), also can be used to determine the elastic limits in the bulging problem; for example, if Equation (1.4) is divided by w_0, it is possible to obtain the following linear relationship that permits define where the nonlinear effects introduced in the bulging process start, Equation (1.4) is reorganized as follows

$$Y = C_1 \frac{\sigma_r t}{a^2} + C_2(v, a/b) \frac{Et}{a^4} X, \tag{1.6}$$

Where $Y = P / w_0$ and $X = w_0^2$. To establish an elastic limit during the bulge test, Equation (1.6) should satisfy the linear relation. If there is deviation with respect to the linear part, it indicates that nonlinear material effects are introduced in localized regions of the film. Deviations will define the pressure limit in which plasticity effects are introduced in the bulged membrane. For the material description of a bulged membrane, stresses and strains can be determined in the location of the maximum deflection, which is dependent on the curvature formed by the bulged film (Shih et al., 2003; Xiang et al., 2005; Neggers et al., 2012). From equilibrium equations determined by Hill (1950), the stresses are simplified on the maximum deflection at x-direction as

$$\sigma_{xx} = \frac{P}{t\kappa_{xx}}, \tag{1.7}$$

where κ_{xx} is the curvature of the bulged thin film. The curvatures are related to deflection produced by the bulging effec which depends on the final geometry after deformed. Strains can be determined from the definition (Ventsel & Krauthammer, 2001) as follows

$$\varepsilon_{xx} = \varepsilon_{0x} + \frac{du}{dx} + \frac{1}{2}\left(\frac{dw_0}{dx}\right) + \kappa_{xx} w_0, \tag{1.8}$$

Where ε_{0x} is the initial strain and u is the displacement field at the x-direction. Equations (1.7) and (1.8) have been applied for thin films with rectangular and circular shapes. For rectangular membranes with aspect ratio $b \geq 4a$ with size of $2a \times 2b$ at $x-y$ plane, the stress and strain are calculated with

the following simplification; when the film is deflected, its shape is assumed to be a cylindrical structure, allowing the curvature estimation. Therefore, stress and strain are computed as

$$\sigma_{xx} = \frac{P\left(a^2 + w_0{}^2\right)}{2w_0 t}, \tag{1.9}$$

and

$$\varepsilon_{xx} = \varepsilon_{0x} + \frac{\left(a^2 + w_0{}^2\right)}{2aw_0} \arcsin\left(\frac{2aw_0}{a^2 + w_0{}^2}\right) - 1. \tag{1.10}$$

The stress state at the maximum deflection point is equi-biaxial very; these are described by Marandi et al. (2017) and Sheng et al. (2017). Circular thin films are very adequated for bulge testing since the spherical cap model allows to simplify the analysis; in the case of $w \ll a$ the stress-strain relations are calculated as

$$\sigma = \frac{Pa^2}{4wt}, \ \varepsilon_{xx} = \frac{2w^2}{3a}. \tag{1.11}$$

The equations shown for calculating elastic parameters are advantageous in the characterization process of thin films. But, when the materials present hyperelastic behavior, other theoretical models should be considered to complement analytical models used for bulge testing, for example, neo-Hookean, Arruda–Boyce, Gent, and Fung models (Sheng et al., 2017).

Thin films can be made multilayer, which means that each layer can be of different materials. The calculations for this configuration depend on the relation between the thickness and the material. However, equation (1.4) satisfies the kinematic and static conditions generated over the composite film, only if its behavior is in the linear regime. A simple formula is expressed to relate the Young biaxial modulus of each layer with the global elasticity of the composite thin film (Shojaei and Karimi, 1998; Martins et al., 2008; Lau et al., 2012) as follows

$$\bar{E}_c = \bar{E}_1 \frac{t_1}{t} + \bar{E}_2 \frac{t_2}{t} + \ldots + \bar{E}_n \frac{t_n}{t}, \tag{1.12}$$

Where $\bar{E}_c = E_c/(1-v_c)$ is the global composite Young modulus, and $t = \sum_1^n t_i$ is the total multilayer thickness. Equation (1.12) also can be expressed in terms of the residual stresses σ_r. Several authors have applied the multilayer models for mechanical characterization of thin films by bulge test (Small et al., 1994; Martins et al., 2008; Marandi et al.,2017). However, in multilayer thin films, the manufacturing process affects the determination of mechanical properties since when an additional layer is deposited, the interfacial stresses deform and modify the stress distribution inside these (Zhang, 2008). This concept was introduced by Stoney (1909) which developed the first equation for assessing the stresses in a thin film fabricated on a substrate (bilayer configuration), Stoney's equation is represented by the curvature as

$$\kappa = \frac{6 f_f}{\bar{E}_s h_s^2}, \tag{1.13}$$

Where f_f is the force of the deposited film on the substrate, $\bar{E}_s = E_s/(1-v_s)$ is the substrate's biaxial elastic modulus, h_s is the thickness of the substrate. Equation (1.13) is rewritten considering the residual stress $\sigma_{r(f)}$ of the film, which is reorganized as

$$\sigma_{r(f)} = \frac{\kappa \bar{E}_s h_s^2}{6h_f}, \tag{1.14}$$

Equation (1.11) is assumed on the following considerations, which were summarized by Freund & Suresh (2003); (a) thicknesses are small compared with the lateral dimensions; (b) the deposited thin film thickness is much lower than the substrate thickness; (c) the substrate is considered a homogeneous material, isotropic, and elastic; (d) the edge effect is invariant in the substrate which means that is not debonding effect considered; (e) Stresses along the thickness are neglected; and (f) the strains and rotations are considered infinitesimally small. Considering that the assumptions mentioned above present limitations in the Stoney model's applicability, several authors developed different models to include other mechanical effects in the interaction between the substrate and the deposited film. Chou et al. (2011) describe analytical models that represent extensions of Stoney's model.

1.6 Experimental setup for bulge testing

For the experiments, bulge test equipment was constructed in-house for testing thin films as shown in Figure 1.13a. The test specimens are commercially available silicon nitride (Si_3N_4). For the experiments, membranes of Si_3N_4 monolayer of 2×2 *mm* and 3.5×1.5 *mm* were used.

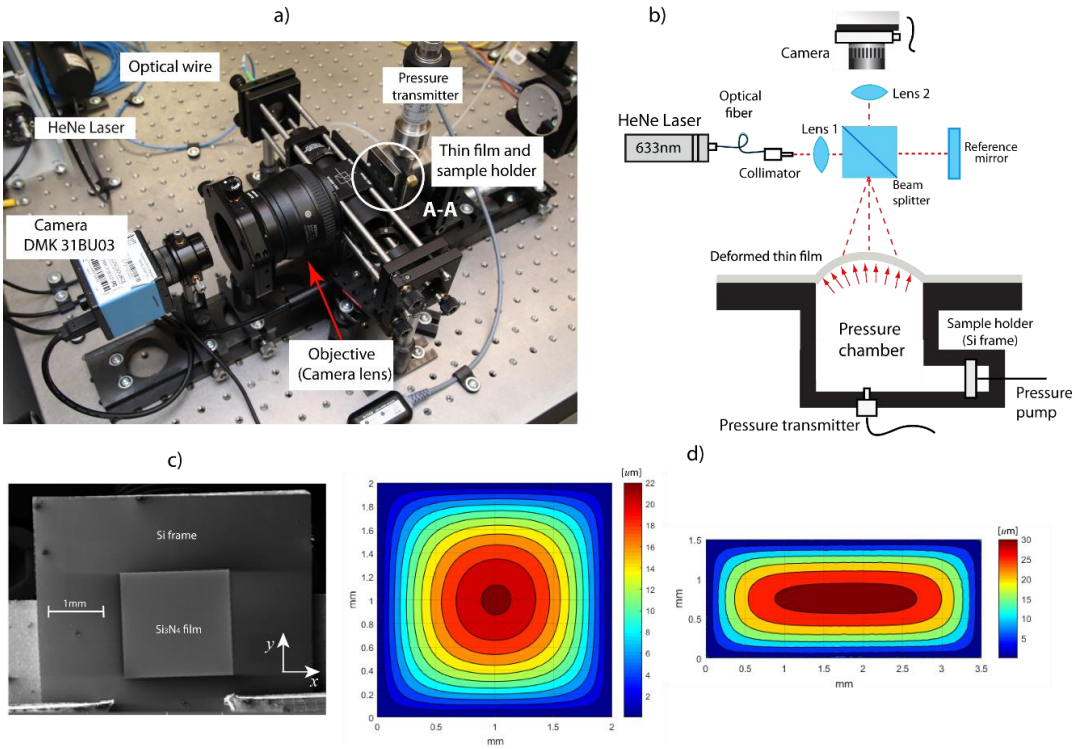

Figure 1.13. (a) Experimental setup for bulge testing. (b) scheme of the bulge test apparatus. (c) Image of the thin film (Si_3N_4) and Si frame, section A-A. (d) reconstructed displacement field of bulged thin films.

Having thicknesses of 500*nm* and 100*nm* for square and rectangular membranes, respectively. These were bonded along its periphery to a supporting Si frame that acts as sample holder as illustrated in Figure 1.13b and labeled as section A-A (see Figure 1.13c). The principle of the test is to apply a differential pressure on a free-standing membrane and to measure the membrane shape in the form of a displacement field for each pressure increment.

The differential pressure is applied using an industrial-grade piston that presses the air by a computer-controlled syringe pump. Pressure is measured by the pressure transmitter with a maximal error of 60Pa connected to a data acquisition system. The shape of the membrane is measured using an interferometric system (Twyman-Green interferometer) in which the light source is a fiber-coupled HeNe laser with wave-length of 633*nm*. The beam is split into a measuring beam reflecting off the measured sample and a reference beam reflecting off a reference mirror with high surface flatness of λ/10. The measuring beam interferes with the planar reference beam at the interferometer's output, forming interference fringes projected onto the camera sensor using an objective (Nikon 50*mm* f/1.4 NIKKOR G). Interference signals captured on each camera pixel are then used to establish the displacement field of the *z* position of the thin film. The number of *x-y* points for which the *z* position is measured depends on the membrane size and geometry but usually exceeds 40000. For the experiment, 10 - 15 measurements per second of membrane shape and pressure are stored. In Figure 1.13b the scheme of the experimental setup is shown. Figure 1.13d represents the reconstructed shape of experimentally measured deformed membranes. It demonstrates that an interferometric configuration permits a precise capture of the whole shape of the membrane. The testing device is also equipped with sensors to measure ambient temperature, pressure, and humidity to calculate the air refractive index. Constructed bulge test apparatus is described in detail in Holzer et al. (2017a). Working principles, theory and applications of bulge testing can be found e.g. in Yang et al. (2008).

1.7 Statement of the problem

Thin-film manufacturing involves demanding instrumentation to achieve dimensional and mechanical conditions, which should be controlled for industrial applications, especially those related to microelectronics (ultra-large-scale integrated circuits), microelectromechanical systems (MEMS), nano-devices, coating applications, biomedical devices, among others (Gunda et al., 2017). Therefore, the knowledge of the mechanical properties is essential for the field of miniaturization, especially if these will be subjected repeatedly to deformations by bending, folding, rolling, twisting, stretching, thermal cycling, and compression stresses. Furthermore, the importance of their characterization lies in understanding the influence of the mechanical properties to improve the reliability in engineering applications.

The assessment of mechanical properties in thin films is considered a difficult task since the small dimensions do not allow the use of well-known standardized tests, which means applying appropriated testing methods for bulk specimens. Furthermore, the residual stresses in thin films will influence the uniaxial tests (traditional test for bulk materials) doing that the characterization of the

material presents a dependency of this parameter. This factor demonstrates that the mechanical properties depend on its manufacturing process (thermal growing, vapor deposition, etc.). Therefore, determining their properties leads to experimental challenges to guarantee the reliability in the dimensional scales, micro, and nano in some cases (Xiang et al., 2005; Xiang & Vlassak et al., 2006).

There are two types of prepared thin film specimens; those as-deposited on substrates and others in freestanding conditions (removed substrate). Both present advantages and disadvantages depending on the experimental approach used to extract its intrinsical properties (Kraft & Volkert, 2001; Gunda et al., 2017; Matějka et al., 2020). For this purpose, several experimental techniques have been developed to determine several properties of thin films as nanoindentation, diffraction-based techniques, Raman spectroscopy, deflection techniques, among others (Mitchell et al., 2003; Poelma et al., 2011). The relative advantages of all the methods mentioned have been discussed in the literature (Nix, 1989; Huang et al., 2007; Zhang et al., 2015), highlighting the benefit of one of the methods for easy implementation called the bulge testing. This technique is considered one of the most promising methods for characterizing the mechanical properties of thin films since analytical models allow the calculation of mechanical parameters using experimental data. Bulge testing is a well-known technique for studying several mechanical properties of thin films (Lin et al., 2014) in which are the residual stresses, Young's modulus, Poisson ratio, fracture toughness, among other properties (Mitchell et al., 2003; Wei et al., 2009; Orthner et al. 2010; Merle & Göken, 2014; Tinoco et al., 2020). Their implementation is considered a practical process since, compared with different techniques, there are less sophisticated technical procedures to be adopted.

The bulge test technique is based on applying gas pressure to deflect a membrane and produce a bulged region (Lu et al., 2013; Sheng et al., 2017). The relation between pressure and curvature of the membrane is called load-deflection dependence. This relation is used to characterize mechanical properties under specific controlled conditions. The effects of the applied pressure, which are reflected in the kinematics of the film, and these are depending on its intrinsic properties; such as the geometry, the material properties, and the residual stresses (Beams, 1959); Small & Nix, 1992, Lee et al., 2007; Min et al., 2017; Tinoco et al., 2019). The variation of these parameters influences the kinematics of a bulged film; it refers to the changes in the displacement field, strains, and curvatures by the loading increments as detailed in one of the earliest works developed by Hill (1950).

In the bulging process, stress-strain distributions are developed over the stretched surface, and their calculations are estimated on the maximum deflection point with the classical equations (Vlassak & Nix, 1992; Xiang et al., 2005; Huang, 2007; Lu et al. 2013; Tinoco et al., 2018a). For these computations, two types of specimen geometries are preferred: i) circular ones treated within a spherical cap model (Small & Nix, 1992; Schalko et al., 2011; Zhang, 2016); ii) Rectangular films with aspect ratio 1/4 are the most used since the curvatures are approximated by a cylindrical profile (Xiang et al., 2005; Javed et al., 2016; Shafqat et al., 2018). For both geometries, the stresses are predicted at the location of maximum deflection, which depends on pressure and their local curvatures (Chang et al., 2009); this means that quasi-static (pressure) and kinematic (deflection field) parameters should be previously known. One of the first models performed for a spherical membrane (Beams, 1959) described these aspects. However, Beams (1959) model exhibited several limitations in identifying properties, which was corroborated numerically via finite element analysis by Small and Nix (1992),

posteriorly. Zhang (2016) reviewed theoretical models for clamped circular plates and membranes; he presented several models with different assumptions to predict the bulging problem. Zhang (2016) demonstrated that other analytical approximations violate, in some cases, the clamped boundary conditions. Therefore, fourth-order models were derived, and the analytical solutions consider the Poisson's ratio as a variable and not as constant.

For rectangular films, Tabata et al. (1989) reported an analytical model, but Vlassak and Nix (1992) developed expressions obtained from the energy minimization technique to describe the bulge test in rectangular and square membranes. They showed that Young's modulus and residual stress could be obtained by applying least-square regression with experimental data in a simple way. Also, Poisson's ratio was determined from two different membranes with a sufficiently large aspect ratio between them. Constants involved in the models were computed by analytical solutions (Tabata et al.,1989; Vlassak and Nix, 1992) and finite element approximations (Pan et al., 1990). This procedure provided a reliable basis for determining elastic properties from load-deflection curves since these obtained analytically were inaccurate. Later, Maier-Schneider et al. (1995) confirmed Pan et al. (1990) results, showing that some parameters obtained analytically were not computed accurately, which led to more significant differences between experimental and calculated curves. Furthermore, Maier-Schneider et al. (1995) presented a kinematic analytical model for the deflected surface as an extended model by Timoshenko and Woinowsky-Krieger (1959), which depends on the maximum displacement only. The proposed kinematic model was not used in direct applications to determine mechanical properties, but in this thesis, the computations of curvatures and strains were applied to estimate the stress field using Maier-Schneider et al. (1995) model since this model bring a better approximation. However, the deflection models are used in other problems related to plates and membranes, as is the case of Zheng et al. (2015) that presented a new deflection shape function that predicts the deflection profiles of Capacitive micromachined ultrasonic transducers (CMUTs) for rectangular membranes. The predictions profiles showed excellent agreements with finite element analysis results. But, in bulge testing, the deflection models have been limited since for rectangular membranes, the deflection shape is very approximated to a cylindrical shape considering the membranes with an aspect ratio higher than 1:4.

In the case of square thin films, there are no reported, neither validated numerically and experimentally analytical models, intending to estimate the stresses and strains since the curvature computations have not been made available for these films. However, experimental evaluations have been reported for their determination (Chang et al., 2009; Neggers et al., 2014). The lack of an adequate deflection field presents a limitation for estimating properties since these depend directly on the stresses developed by the bulging effect. Furthermore, the curvatures have not been predefined in square thin films since the kinematic description of the bulged surface cannot be approximated with a regular shape. Nevertheless, the approximations often do not meet all requirements of a real bulged thin film. Neggers et al. (2012a) mentioned that discrepancies in the results shown by different authors are attributed to erroneous considerations of the curvatures. For square films, the geometry of the bulged surface deflection is more complicated than a simple cylindrical shape, as in the case of rectangular films. Neggers et al. (2012b) demonstrated the errors by calculating the local curvature maps at the boundaries through Digital Image Correlation (DIC) technique. It means that the validity of the bulging equations is subjected to specific regions inside

the deflected surface. One question can be proposed for this challenge: how to approximate the curvatures in a bulged square thin film?

It is well known that analytical models are more suitable if we take into account their simplicity in the evaluation of elastic properties, but the development of new analytical tools was stopped by the advantages of finite element solutions in the last decades. Both approaches (i.e. analytical and numerical) present advantages and limitations in the characterization process of elastic properties using bulge tests. Therefore, there is an excellent possibility of improving the analysis to determine properties using analytical and numerical tools. This thesis focuses on developing tools for determining the mechanical properties of thin films using bulge testing from a numerical and experimental approach.

1.8 Aims of the thesis

The objective of this thesis is to contribute towards the characterization of mechanical properties of thin films by the numerical modeling of mechanical tests. It implies developing new models to describe the mechanical behavior of monolayer and bilayer thin films in different scales and mechanical conditions that include elasticity, plasticity, and fracture. Bulge testing is a well-known technique in mechanical properties identification, however, some challenges have been found in the literature review of theoretical models developed in the last few years, since these are limited and simplified by the film geometry, the plasticity effects, and interaction between layers.

The properties of the materials in form of thin film are significantly different from these properties determined in bulk form, however, other materials can only be manufactured in this way. Therefore, new methodologies that permit to characterize these films is a topic that is in discussion and developing, currently. Additionally, some experimental tests carried out on thin films have shown difficult correlation between numerical models and experimental observations in some cases. To overcome these challenges, in the literature are found approaches that include theoretical models, numerical models and experiments. However, main effort is focused on the development of numerical and analytical tools. In this thesis not only elastic-monolayer thin films are studied but also bi-layer structures are in focus. Important issue is also identification of plasticity based on bulge test.

1.9 Thesis outline

In this thesis, the chapters are organized and described as follows:

- Chapter two is based on a consolidation of a methodology to determine both elastic parameters (Young's modulus and Poisson's ratio) of silicon nitride (Si_3N_4) films using bulge tests, analytical solutions, and finite element analysis. A numerical approach is presented, which permits estimating a unique pair of solutions (E and ν) using two thin films with different geometries, In the chapter is shown an study case using square and rectangular thin films.

- In chapter three, a numerical approach is presented for identifying the elastic properties of thin films. With one monolayer thin film, the main contribution of this chapter corresponds to

determining the Young's modulus and the Poisson's ratio. Experimental data and finite element solutions of commercial silicon nitrate (Si_3N_4) films were compared using the properties.

- Chapter four discusses constitutive models based on an analytical solution for the displacement field for calculating the stresses and strains in bulged films. In the validation process, practical applications were proposed to characterize elastoplastic material models using bulge tests and analytical approximations. Using the proposed deflection field, the curvatures are computed locally in linear and nonlinear material states. A finite element analysis was used to validate the presented models.

- Chapter five presents two study cases, one involving the finite element analysis of a freestanding Au thin film, and the other examining the characterization of plastic parameters in an Al thin film. Both cases were subjected to bulging tests. In the first case, the gold films were analysed to determine their elastoplastic properties and fracture toughness. The problem was divided into two stages; the first stage was developing the numerical model on the whole film without pre-crack (elasto-plastic analysis). The second stage involved a portion of the film that included pre-crack (sub-modeling). By using path independent J-integral, three different notches (rounded, sharp, and V-sharp) were used to calculate the stress intensity factor around the crack tip. In the second study case, an Al thin film was used as the study sample. It was subjected to cycling loading, which meant that different levels of pressure were applied during loading and unloading. With this methodology, it is possible to determine the elastic limit, yield stress, and other mechanical parameters involved in the bulge test.

- Chapter six describes a numerical methodology based on the combination of finite element analysis and classical analytical equations to estimate the elastic properties of a deposited thin film over a known substrate, which configures a bilayer thin films application. Finite element modeling was conducted for bi-layer (Si3N4/Al) membranes to compute its elastic parameters (Young’s modulus and Poisson’s ratio) and the residual stresses in each film. The determination of the residual stresses is the main contribution of this chapter since the conventional analytical models are restricted to the calculation of a global residual stress. This difficult to perform simulations due to that this parameter is an input condition.

Chapter 2. Determination of the elastic properties using an experimental-numerical approach with two different bulged thin films

This chapter describes the computation of Young's modulus and Poisson's ratio using a numerical methodology (FEM and analytical equations) that combined with two independent experiments of bulge testing is possible to determine both parameters. Experimental tests were conducted on rectangular and square thin films in order to determine their unique elasticity constants. The numerical calculations were carried out by a finite element analysis and the classical identification method (analytical equations).

2.1 Finite element modelling of bulge test for freestanding thin films

This section describes a numerical model for simulation of the bulge test of thin films utilizing a finite element analysis. The advantage of carrying out simulations is the parametric conditions that can reproduce the experimental tests when the mechanical properties are modified. Another advantage consists in the measurement and comparison of the displacement field not only of the central point (maximum deflection) as considered by the analytical model presented in equation (1.4). It relates the pressure with the maximum displacement only in one degree of freedom. For this reason, finite element analysis is considered as a powerful tool to predict load-deflection dependency of the whole measured deformed surface, as several works have already demonstrated (Tabata et al.,1989; Pan et al., 1990; Gan et al., 1996) till nowadays (Orthner et al., 2010; Zhang et al., 2016).

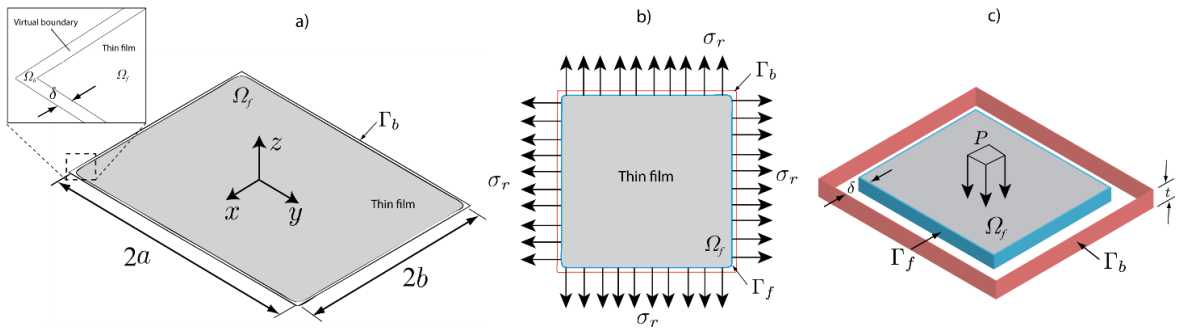

Figure 2.1. (a) Thin film model with extension. (b) Residual stress application. (c) boundaries Γ_b and Γ_f.

Let's consider a rectangular membrane of width $2a$ and length $2b$ ($a > b$) defined by the surface Ω_f as illustrated in Figure 2.1a, where Ω_f is the surface under investigation (thin film). With the aim to apply realistic boundary conditions, an additional surface Ω_b is created with an extension of thickness $\delta = 2\lambda a$, where $\lambda \in (0.01, 0.02)$ joined at the external boundary $\Gamma_f \subset \Omega_f$. The solution process is performed in two stages; the first one is based on the applications of residual stress σ_r, and the second one is the application of pressure levels. The geometric extension δ acts as a virtual boundary and it was defined to permit that σ_r deforms the thin film in the first stage of solution. In Figure 2.1b,

the application of an isotropic residual stress σ_r on the boundary Γ_f composed by the faces $B_i \forall i = 1,...,4$ is shown.

In the second stage, Ω_b is highly pre-stressed by σ_r effects, which in turn acts as a displacement constraint by the deformations caused on Ω_b. It does not present any considerable influence on Ω_f since is pre-stressed constantly in the entire domain. In this stage, a pressure load on the pre-stressed membrane Ω_f as well as displacement restrictions (clamped) on Γ_b are strictly imposed (see Figure 2.1c).

In the numerical model, a geometric nonlinearity is considered, i.e. large deformations are included, indicating that the membrane stiffness can change with the increment of load-deflection. Nevertheless, the membrane material is assumed to be homogeneous and linear. Tetrahedral elements with six nodes by face are imposed as finite elements in the model. It is important to mention that experimental tests are conducted with the bulge test apparatus described in Section 2.2. with the aim to verify the effectiveness of the procedure developed in this study.

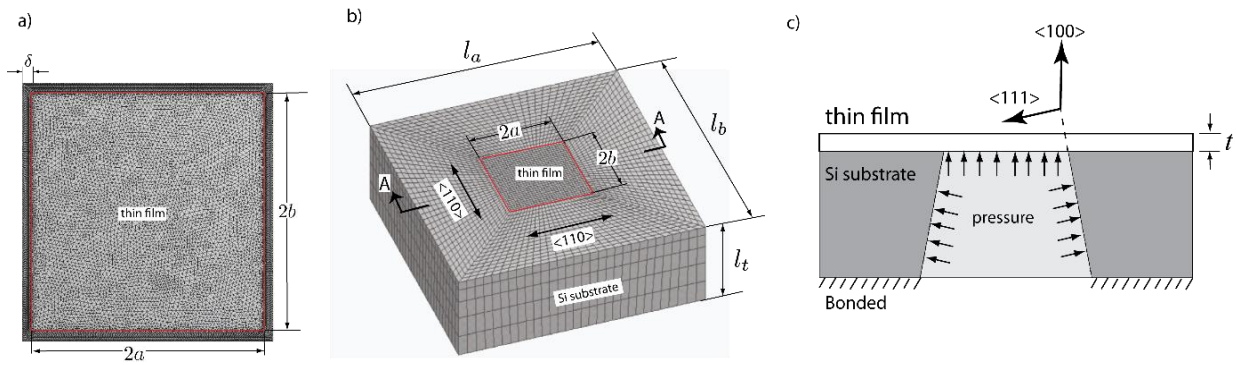

Figure 2.2. (a) Rectangular thin film with extension δ . (b) Whole set including sample holder (Si substrate). (c) Transversal section of thin film with the silicon substrate.

In order to verify the numerical model proposed (model with the extension δ), finite element solutions were obtained with ANSYS 16.1. In addition, a comparison was performed with traditional modeling that includes the thin film adhered to a Si substrate, which acts as the sample holder in the bulge test. Traditional bulge test simulations include the substrate in the model since this supposes a more realistic analysis. However, it is more time-consuming from a computational point of view because more finite elements are necessary, and the computational cost increases in the full model. Figure 2.2a shows the simplified model (model with the extension δ), and Figure 2.2b represents the full 3D model, which includes the Si substrate. A transversal section is shown in Figure 2.2c. Elastic constants $C_{11} = 165.7GPa,\ C_{12} = 63.9GPa$ and $C_{44} = 79.6GPa,$ of the Si substrate are taken from Hirth et al., (1983). Elastic moduli in individual directions $E_{100} = 130GPa,\ E_{110} = 170GPa$ and $E_{111} = 188GPa$ were calculated from these constants. For the whole model, the following dimensions define the experimental tests $l_a = l_b = 6mm$ and $l_t = 2mm$. The following sizes described the thin film: *a=1mm* and *b=1mm.* Boundary conditions are established as clamped (bonded surface) in the bottom part of the substrate.

Both simulations (full and simplified) are shown and compared in Figure 2.3a, in which the left axis is the pressure, and the right axis is the relative error of the maximum displacement between both models. Continuous line represents the relative error of the maximum displacements in the full and simplified model. Triangles represent the maximum displacement of the central zone in relation to the

applied pressure. The following properties were considered in Figure 2.3a: $E = 230GPa$, $\sigma_r = 165MPa$ and $v = 0.26$ to validate and compare the proposed numerical models. From Figure 2.3a, it is evident that at low pressure, the errors reach maxima of 1.33 % and the error takes lowest values (below 0.6%) at the highest pressures. It indicates that both models presented a good correlation in the load-deflection curve, however, its effects are more visible in the first part of the curve where the residual stress dominates. In conclusion, we can highlight that the simplified model is acceptable to simulate bulge testing of thin films with the proposed modeling methodology.

Three numerical models were used to analyze the effects of the virtual boundary (extensión δ) in the simplified model applying the following properties $E = 200GPa$, $\sigma_r = 150MPa$ and $v = 0.25$ for all models. The value δ is determined as a percentage of the larger side ($a > b$) of the pressured surface of the membrane; we suggest taking values between 0.25% to 2% since the errors are less than 0.4 % in the maximum relative deflection. Figure 2.3b illustrates a convergence analysis that evaluates the proposed simple model's relative error (maximum deflection) in Section 2.2.

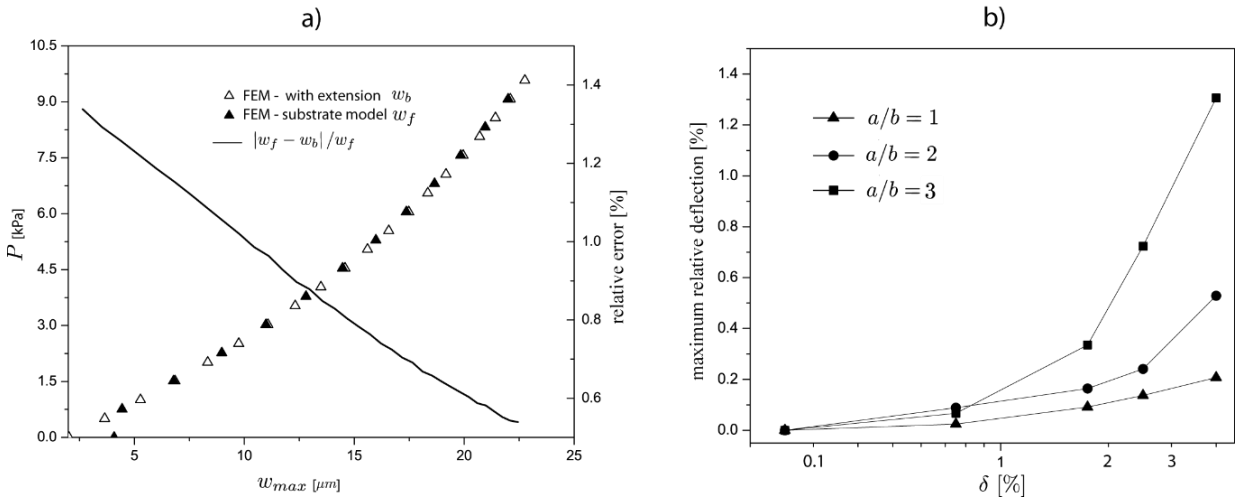

Figure 2.3. (a) Comparison between the model with extension and model with the substrate. (b) Convergence of the maximum relative deflection ($\delta = 0.25\%$) vs percentage of extension of the virtual boundary.

Thin films with ratios $a/b = 1$, $a/b = 2$ and $a/b = 3$ were taken as numerical samples to assess the effects of the extension δ on the convergence of the maximum deflection. These values were established because films used for experimental tests (in this study) are in this range. It can be seen from Figure 2.3b that all studied membranes presented convergence or trend to zero when the extension δ is 0.25%. Maximum errors between 0.25% and 1.4% are observed for $\delta = 4$ %. δ values lower than 2% show that there are relative errors lower than 0.4%, and therefore the proposed modeling shows numerical stability. In our study, $\delta = 0.25$ was used for the finite element computations. It can be concluded that the presence of a virtual boundary does not affect the displacement solutions.

2.2 Numerical approach for determining elastic properties using two thin film samples

The best two set of solutions (E and v) are selected. The chosen criterion is the relative error of the maximum displacement between the curves $P(w_{\max})_{EXP} \approx P(w_{\max})_{FEM}$. Then, with all parameters estimated ($E_i, \sigma_r, C_{1(FEM)}$), $C_2(v_i), \forall i = 1,2$. Equation (1.4) can be completed. Then, parameters α, β are calculated in the following way:

$$\alpha = \frac{v_2 C_2(v_1)(1-v_1) - v_1 C_2(v_2)(1-v_2)}{v_2 - v_1}, \beta = \frac{C_2(v_2)(1-v_2) - C_2(v_1)(1-v_1)}{v_2 - v_1}. \tag{2.1}$$

Using α and β constants, we can establish a function for $C_2(v)$ that defines its values for any known v. However, the determination of v is implicit inside the numerical procedures. Thus, an error function $e_p(E,v)$ is constructed with equation (1.4) and experimental data $(P_{\exp}, w_{\exp})$ to correlate these with parametric values established by (E,v). This error function should be used to find optimal values of (E,v). For example, the following expression defines it as:

$$e_p(E,v) = \sum_{j=1}^{n} \left| \frac{P_{\exp(j)} - P(v, E, w_{\exp(j)})}{P_{\exp(j)}} \right| / n, \tag{2.2}$$

where

$$P(v, E, w_{\exp(j)}) = C_{1(FEM)} \frac{\sigma_r t w_{\exp}}{a^2} + \left(\frac{\alpha + v\beta}{1-v} \right) \frac{E t w_{\exp}^3}{a^4}. \tag{2.3}$$

The result of equation (2.2) is an error surface where the minimum errors should be located where a set of E and v agree precisely with the experimental measurements. According to previous exploratory data analysis done in our study, it was found that a linear approximation can define the set of optimal solutions for E and v as described in the step 6. We will find a set of parameters that approximate the analytical equation and the finite element model until this step. This step demonstrates that the elastic coupling exists between both parameters in the solutions, which means that these depend on each other. To compute a unique solution, the following linear function should be extracted as follows:

$$v_k = mE_k + b, \forall k = 1, \ldots, p. \tag{2.4}$$

where E_k, v_k is a set of values that satisfies the condition of $\min|e_p(E,v)| \approx 0$ or $e_p(E_k, v_k) \approx 0$. These values belong to a linear function which is shown in Equation (2.4). If it is computed for two different geometries i and j, the intersections ($\min|e_{p(i)}(E,v)| \cap \min|e_{p(j)}(E,v)|, \forall i \neq j$) of the linear functions extracted from $e_{p(i)}(E,v)$ and $e_{p(j)}(E,v)$ will define an optimal solution $(E,v)^*$ which is the objective of the step 7.

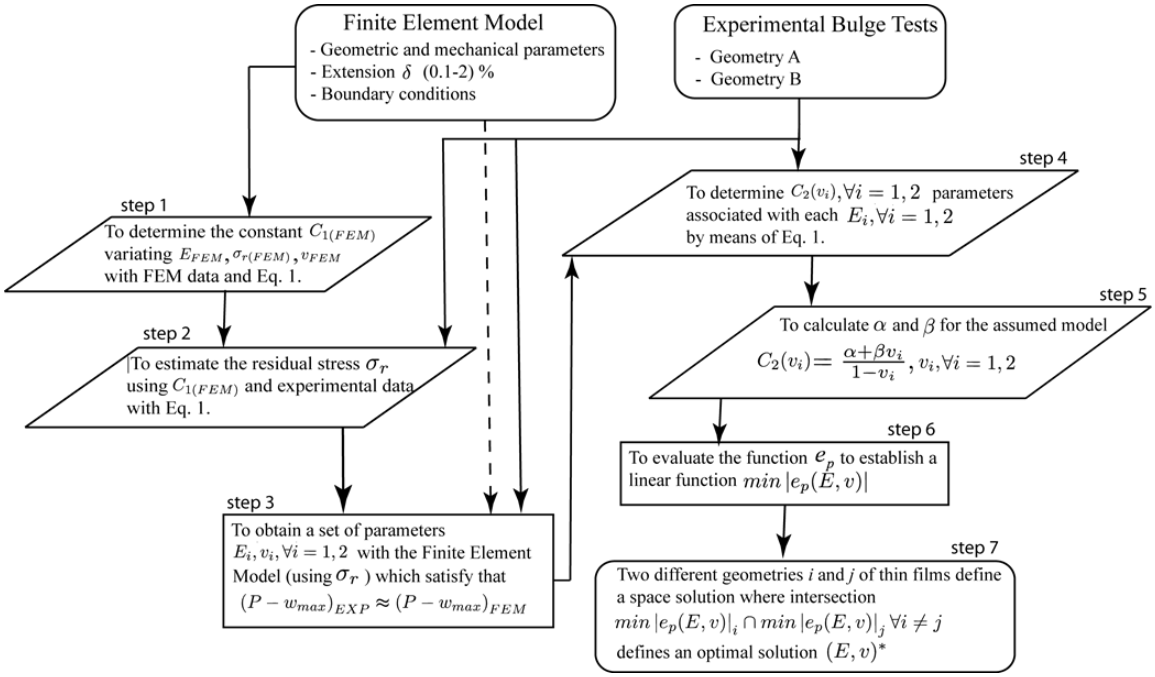

Figure 2.4. Numerical approach to determine both elastic parameter of both thin film geometries (rectangular and square)

2.3 Effects of Young's modulus, Poisson's ratio, residual stress and on load-deflection relation

Numerical analysis by finite elements has been directed to comprehend better the mechanical parameters involved in the bulge test. In Figure 2.5, different curves are obtained for different values of residual stresses, Young's modulus, and Poisson's ratio. The aim was to examine the effect of these parameters on the load-deflection curve defined by the pressure (P) and maximum deflection ($w_{\max}$) for a film of 2×2 *mm* and 500 *nm* of thickness. From the Figure 2.5a, it is seen that when the residual stress increases, the maximum displacements decrease for the same pressure level. According to equation (1.4), σ_r determines the linear part in the relation $P(w_{\max})$. The following elastic properties were used as part of input parameters in the finite element model, $E = 210GPa$ and $v = 0.26$. Figure 2.5b illustrates the changes produced by the variations of Young's modulus in the relation $P(w_{\max})$ in a film with $\sigma_r = 165MPa$ and $v = 0.26$. It is analyzed that when Young's modulus varies between $250GPa$ to $250GPa$, $w_{\max}$ exhibits changes in the region that it is not influenced by the residual stress (i.e. nonlinear region of $P(w_{\max})$) as mentioned before. It means that there is a limit value of pressure under which the mechanical behavior is negligibly influenced by the elastic constants. Specifically, the limit value is defined by the delimitation of the linear relation at low pressures states (internal pressures $< \sigma_r$) as highlighted in Figure 2.5b with the black arrow.

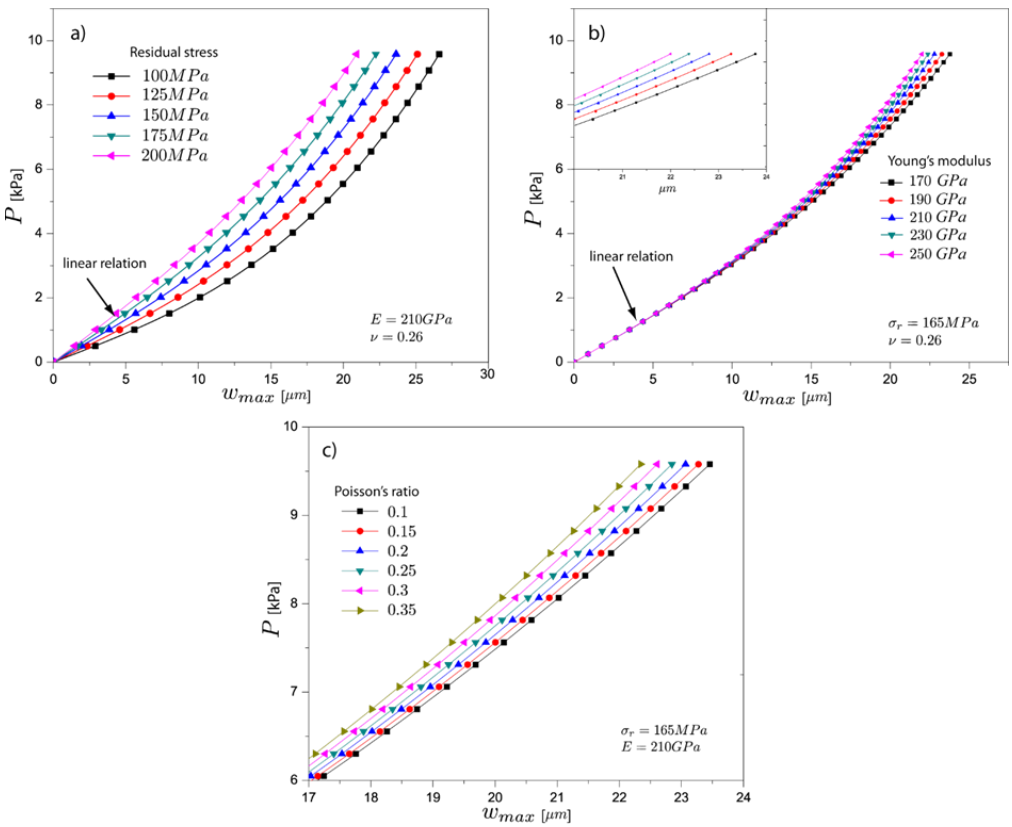

Figure 2.5. Influence of (a) residual stress. (b) Young's modulus. (c) Poisson's ratio on load-deflection curves.

It is evident from equation (1.4), that the cubic part of the displacements is governed by the elastic parameters $C_2(\nu)$ and E. This result shows that in an estimation of the elastic parameters, σ_r present higher effect compared with the influence of E. We can observe the same behavior in Figure 2.5c when ν is varied, however, in the figure the scale of both axis is augmented in a particular region $w_{\max} \in (17,24)um$ and $P \in (6,10)kPa$. It points out that the elastic parameters E and ν are coupled together since the effects on the curve are the same. If both parameters were modified in a way that the curve remains fixed, we observe that there are different pairs of E and ν that satisfy the same solution. This is verified and explained in the next sections.

It was concluded that to conduct a parameter identification (σ_r, E and ν), the easy way to determine σ_r is by means of equation (1.4), since to fit the first stage of the $P(w_{\max})$ curve will demand more time with an iterative process performed by finite element computations. This can be solved simply with one iteration adjusting the experimental data in equation (1.4), as we proposed in the numerical approach in Section 2.3. However, according to the theory established in the bulge analysis, the relation between σ_r and C_1 is intrinsic. So, it should be necessary to know at least C_1 constant. In the literature, there are estimated values for C_1 constant as shown by Tabata et al. (1989), Maier-Schneider et al. (1995), Paul & Gaspar (2007) among others. In our case, the value of C_1 is calculated using a set of simulations with input parameters known, for this case, we created a database of 20 samples. It indicates that the same number of $P(w_{\max})$ curves were adjusted in equation (1.4) by least-square regression obtaining the value $C_1 = 3.373 \pm 0.003$.

Table 2.1. Prediction of C_1 and σ_r with finite element data – square membrane 2×2 *mm*

Input parameters – FEM model			Predictions and relative errors			
Poisson's ratio ν	E [*GPa*] FEM	σ_r [*MPa*] FEM	$\sigma^*_{r(p)}$ ($C_1^* = 3.373$, in Eq. (1))	$\frac{\sigma_r - \sigma^*_{r(p)}}{\sigma_r}$ [%]	$\sigma_{r(p)}$ ($C_1 = 3.45$, in Eq. (1))	$\frac{\sigma_r - \sigma_{r(p)}}{\sigma_r}$ [%]
0.25	170	150	150.29	0.19	146.94	2.04
0.25	200	145	145.34	0.23	142.10	2.00
0.20	100	120	119.47	0.44	116.80	2.66
0.26	230	165	165.17	0.10	161.49	2.12
0.3	300	135	135.47	0.34	132.45	1.88
0.18	250	145	144.97	0.02	141.73	2.25
0.15	350	180	180	0	176.07	2.18

It is important to mention that all calculations were done for a film of 2×2 *mm* and 500 *nm* of thickness because these dimensions were used in the experiments. The correction of C_1 is necessary since for the simulations the value of σ_r will correspond with the results of finite element model. It guarantees the best-fit in the simulations and the experimental data in the linear part.

To validate our considerations, a set of predictions for σ_r are listed in Table 2.1 using finite element (FEM) data as input known parameters and least-square fitting in equation (1.4). The predictions computed with $C_1^* = 3.373$ are compared with predictions done with $C_1 = 3.45$ constant which was proposed by Maier-Schneider et al. (1995) that is the most used value in the literature. In Table 2.1, first three columns correspond to input parameters used in each simulation to obtain curves $P(w_{\max})_{FEM}$ with the aim to establish a database as reference measurements. From equation (1.4), $C_1^* = 3.373$ or $C_1 = 3.45$, $\sigma^*_{r(p)}$ and $\sigma_{r(p)}$ were computed to predict the finite element input values for σ_r. In columns 5 and 7, the following relative errors (σ_r and predictions) 0.19 ± 0.16 % and 2.16 ± 0.25 % were determined with the predictions $\sigma^*_{r(p)}$ and $\sigma_{r(p)}$. It is necessary to note that to approximate σ_r with equation (1.4) will assure best-fit since an estimation from finite element computations will demand more time by the required iterations.

2.4 Results: Young's modulus and Poisson's ratio of Si3N4 thin films with two geometries (square and rectangular)

In this section, the results obtained by application the numerical approach described in above section are shown. Thin films were tested experimentally according to the experimental setup described in Section 1.6 (see Chapter 1) with the aim to determine the elastic properties of Si_3N_4 membranes. Two different samples with dimensions 2×2 *mm* and 3.5×1.5 *mm* with thicknesses of 500 *nm* and 100 *nm* were selected for the experiments. Two different specimen geometries are required for the implementation of the identification method of elastic properties. Five specimens of each film were tested and the experimental data were used in the analysis.

Table 2.2. Set of parameters that satisfy the experimental data for $P(w_{\max})$ curves

	Set 1			Set 2		
Membrane Si_3N_4	$E_{FEM}[MPa]$	ν_{FEM}	C_2	$E_{FEM}[MPa]$	ν_{FEM}	C_2
$2\times 2mm$	240	0.24	2.781	211	0.35	2.445
$3.5\times 1.5mm$	235	0.27	1.435	222	0.35	1.519

The residual stress is the first computed parameter in the identification process, applying the steps 1 and 2 as described in Section 2.2 (see Figure 2.2). Parameters C_1 and σ_r were determined for the square and rectangular films as follows: $C_{1S}=3.373$, $C_{1R}=2.08$, $\sigma_{rS}=166\pm 2MPa$ and $\sigma_{rR}=125\pm 1.5MPa$. Subscripts *S* and *R* refer to the square and rectangular thin films. Then, according to the step 3, we used two sets of parameters $E_i,\nu_i \forall i=1,2$ (see Table 2.2) which satisfy the experimental data. These were obtained from the finite element computations by means of iterative calculations. Each load-deflection curve $P(w_{\max})$ was used to estimate C_2 with equation (1.4), all determined data are listed in Table 2.2.

The variables listed in Table 2.2 are required for numerical approximations (explained in Section 2.2) necessary to determine the parameters α and β from Equation (2.1). For determination of C_2 the following models were used: $C_{2S}=(1.9690-0.4594\nu)/(1-\nu)$ and $C_{2R}=(1.2513-0.7527\nu)/(1-\nu)$. Several studies have accepted this approximation applying different values for α and β (Maier-Schneider et al., 1995; Paul & Gaspar, 2007; Martins et al. 2009).

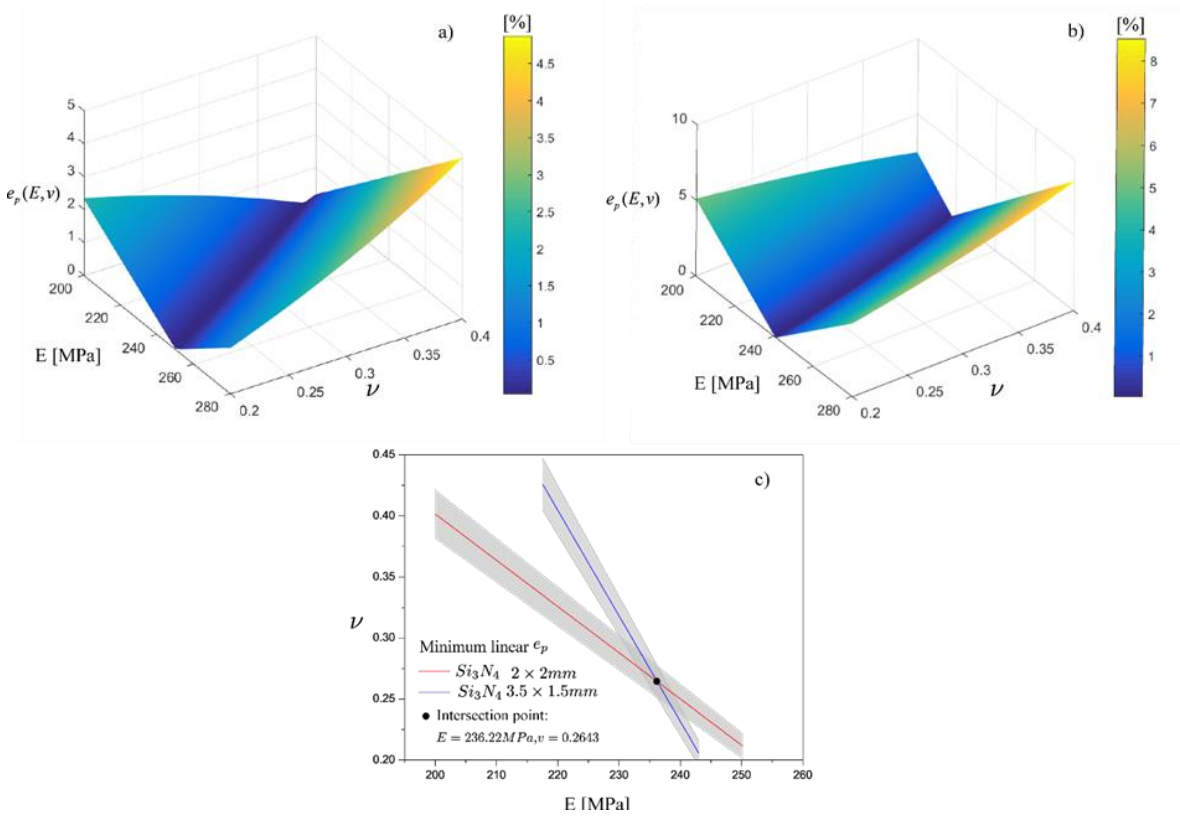

Figure 2.6. (a) Error for square thin film. (b) Error for rectangular thin film. (c) Minimum linear error for rectangular and square thin film.

Applying step 6, error functions $e_p(E,v)$ were constructed using experimental data and all known parameters necessary for the determination of equation (2.2), these are plotted in Figure 2.6a and 2.7b. Basically, both figures evidence that there are pairs of E and v that satisfy equation (1.4) numerically. It indicates that both elastic parameters can generate the same load-deflection curves and therefore there is not a unique solution as demonstrated by $e_p(E,v)$. The reason of testing both specimens (square and rectangular) is to find unique optimal values of *E* and *v* that satisfy the behavior of both membranes.

It is observed that the minimum values converge to a linear function such that $\min\left|e_p(E,v)\right| \approx 0, \forall\{E,v\} \in v_k = mE_k + b, \forall k = 1,...,m$ and therefore these are constructed and illustrated in Figure 2.6c. It is analyzed that both linear functions extracted from Figure 2.6a and 2.6b are intersected in a point in which $E = 236.22GPa$ and $v = 0.264$ is a common solution for both geometries. Grey bands represent confidence intervals of 95% defined from the experiments and numerical computations. Simulations were carried out to validate that the found properties satisfy both experiments (square and rectangular) and these are represented in Figure 2.7a and 2.7b. It is observed that the elastic properties provide solutions of $P(w_{\max})$ which agree accurately for both membranes. Further, the relative errors between the experimental and numerical displacement fields were calculated and mapped (inset in Figure 2.7). For example, for the square membrane, the error of less than 3 % was observed; in the rectangular case, the error in the central region was less than 4%, reaching 6% on membrane boundaries. It can be concluded that the obtained elastic properties are in a fairly good agreement with values reported in the literature, typically 200–260 GPa (Vlassak & Nix, 1992; Karimi et al., 1997; Edwards et al., 2004; Boe et al., 2009; Tinoco et al., 2018a).

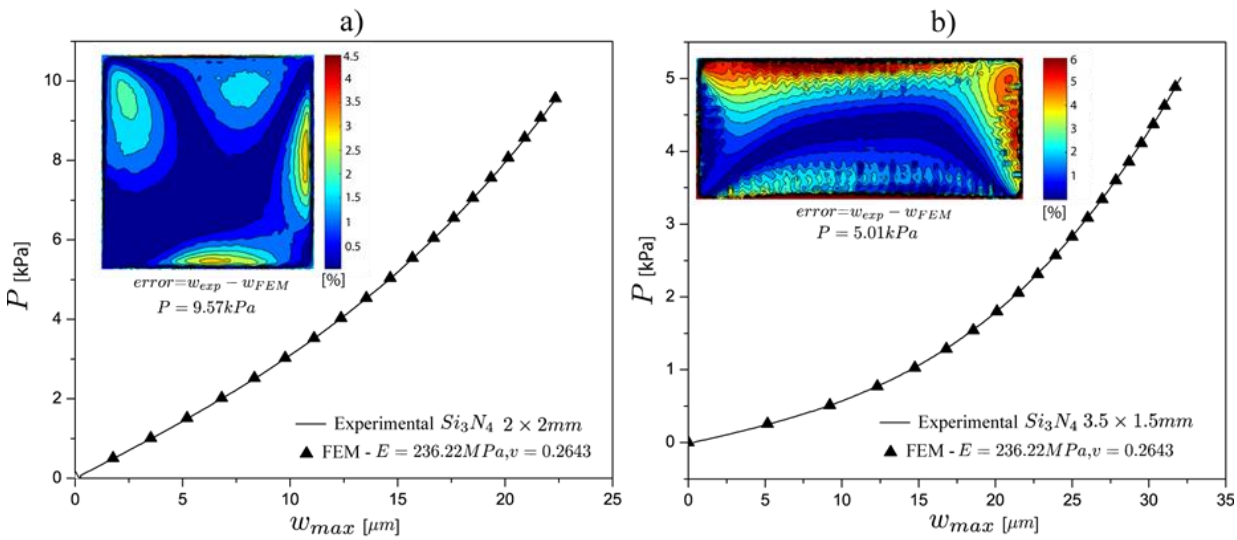

Figure 2.7. Comparison between $P(w_{\max})$ experimental and numerical curves. (a) Square membrane. (b) Rectangular membrane.

Chapter 3. Determination of the elastic properties using an experimental-numerical approach with one bulged thin film

This chapter describes how the elastic coupling conditions of Young's modulus and Poisson's ratio can be used for determining both elastic parameters combining finite element analysis (FEA) with the classical identification method. The presented approach is based on the mapping of both elastic properties with the aim to use only one geometry (one thin film) since, in the chapter, two thin-film geometries were necessary (rectangular and square) to compute these properties. In addition, in this chapter, there are compared two FEA strategies to solve bulge testing problems, this is because the methods presented in chapter two were not validated using traditional methods of simulating it.

3.1 Finite element modeling of freestanding thin films submitted to bulge test

This section describes a comparison between the FEM model developed in Section 2.1 and the traditional way to simulate bulge testing, which has already been implemented in several works (Tabata et al., 1989; Pan et al., 1990; Orthner et al., 2010; Zhang et al., 2015). The main idea is to carry out simulations with both methods which are illustrated in Figure 3.1. The first modeling method is based on considering constant residual stress, this implies that is necessary to impose the residual stress over the whole thin film. Let's consider a rectangular film of size $2a \times 2b$ ($a \leq b$) delimited by the volume Ω_f as illustrated in Figure 3.1a, where Γ_b represents its boundary. In the first method of simulation, residual stress σ_r is applied to each finite element contained within Γ_b.

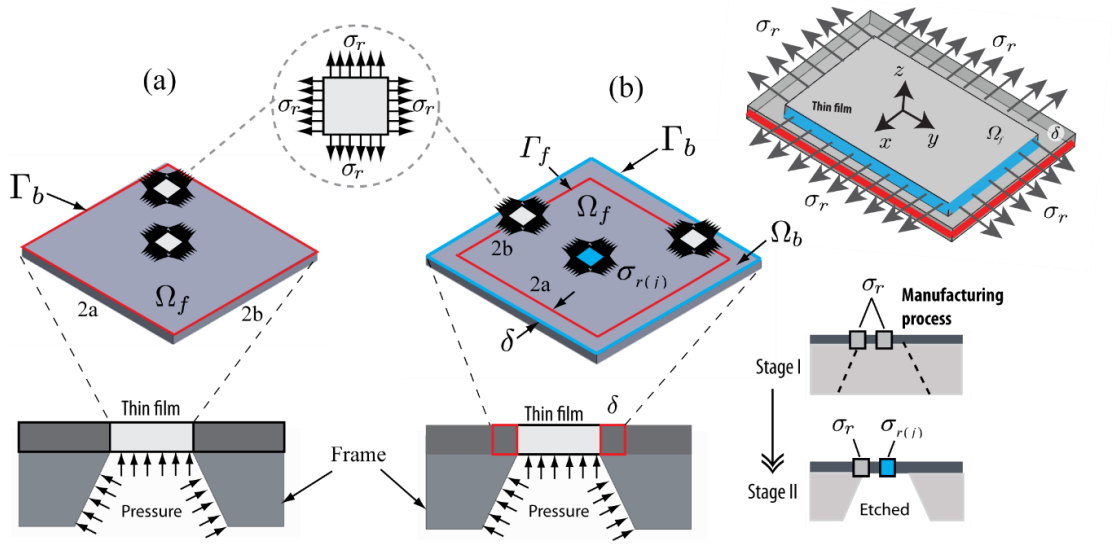

Figure 3.1. (a) Bulge test, thin-film section A-A. (b) Thin-film model with extension, called FEM I model. (c) Residual stress application at the boundaries, called FEM II model.

The method is a traditional way to impose residual stress on a freestanding film that has been deposited over a substrate and has a window. The majority of the studies have reported on this method that simulates the bulging tests (Orthner et al., 2010; Neggers et al., 2014; Zhang et al., 2015;

Shafqat et al., 2018). During the same stage of preprocessing of the model (imposing residual stresses), the pressure is applied over the surface of the film.

The second method of simulation considers the etching process of the substrate (window creation) in which the residual stresses σ_r are redistributed after this process. Therefore, residual stresses are imposed at the film boundaries Γ_f to recreate the two stages of manufacturing, as described in Figure 3.1b. The second approach is considered more realistic in the application of boundary conditions on a freestanding film according to its manufacturing process. The majority of authors that applied FEA to reproduce the bulge test not discussed the details of their models. This is due to the simplicity of the geometry and the parameters involved (pressure and displacement constraint). There are several factors to consider in bulging modeling by FEA, such as the manufacturing process that involves an etching process after the deposition of materials on the substrate, as mentioned before. (Ohring, 2001; Setter et al., 2006).

Let's consider a rectangular membrane of width *a* and length *b* defined by the surface Ω_f as illustrated in Figure 3.1b, where Ω_f is the surface under investigation (thin film). With the aim to apply realistic boundary conditions, an additional surface is created with an extension with thickness $\delta = 2\lambda a$, where $\lambda \in (0.01, 0.02)$ joined at the external boundary $\Gamma_f \subset \Omega_f$ (blue boundary), joined at the external boundary $\Gamma_b \subset \Omega_b$ (red boundary). The solution process is performed in two stages; the first one is based on the applications of residual stress and the second one is the application of pressure levels. The geometric extension δ acts as a virtual boundary which was defined to permit deformations on the thin film in the first stage of the solution. The application of constant residual stresses at the boundary composed of blue faces is illustrated in Figure 3.1b. In the section 2.1 are detailed the numerical procedures that should be carried out to solve a simulation of bulging test by means of finite element analysis. In the numerical model a geometric nonlinearity is taken into account for both methodologies described in Figure 3.1a and Figure 3.1b. In other words, it means that large deformations can be incorporated, indicating that membrane stiffness can change with increasing load-deflection. In order to distinguish the FEA models presented, these will be referred to as FEM I (model shown in Figure 3.1a) and FEM II (model shown in Figure 3.1b).

For all finite element models, tetrahedral elements with six nodes by face were imposed, which are named SOLID95 in the ANSYS database. The thin-film material is assumed as isotropic and homogeneous. Finite element simulations presented in this section were calculated with ANSYS® 19 on an ASUS® ROG Strix GL553VE (Intel Core (TM) i7-7700HQ CPU @ 2.8 GHz, 16 GB RAM) notebook which ran in Windows 10 environment.

3.2 Numerical approach for determining elastic properties using one thin film sample

In this section is presented a sequential numerical procedure that permit through several steps to compute Young's modulus and Poisson's ratio of a thin film under bulging test. A flow diagram is used to explain the procedure. It consists of a set of 10 steps that permit obtaining both parameters combining finite element analysis with the classical analytical solution (see Equation 1.5). Initially, a

finite element model with the required geometric dimensions should be performed including its boundary conditions which are considered clamped in the external domain $\Gamma_b \subset \Omega_b$ of the thin film as illustrated in Figure 3.1b. Modeling the bulge test by finite element analysis is well-established practice (Orthner et al., 2010; Sheng et al., 2017; Shafqat et al., 2018). As long as mechanical parameters are known, numerical analysis is not a complex engineering problem since geometry is very simple and simplified. However, for analysis, large deformations must be considered since the thickness can be very thin, even on a nanometric scale.

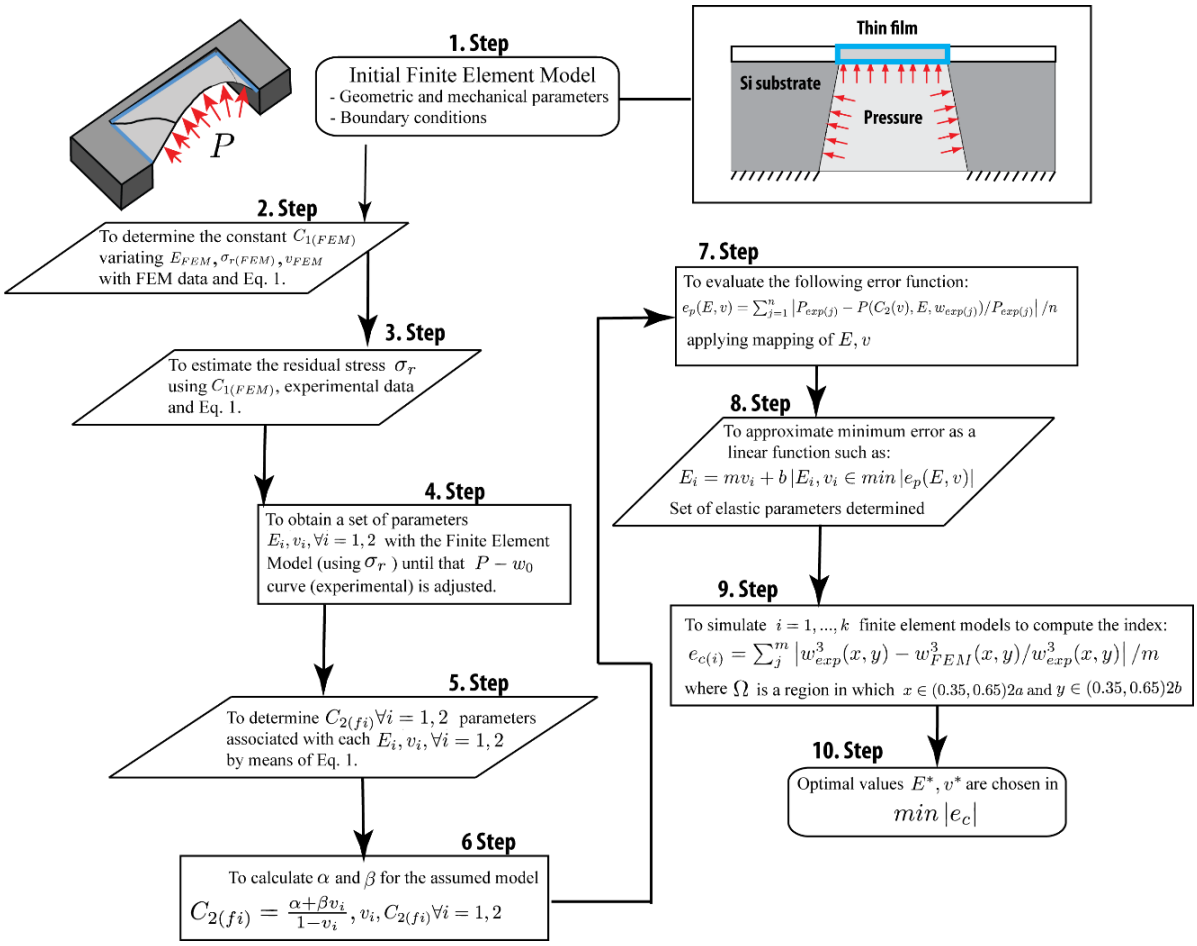

Figure 3.2. Sequential procedure for estimating Young's modulus and Poisson's ratio.

Large deformations mean that the stiffness changes with the level of input load. Following the proposed method, the first three steps deal with the estimation of C_1 and σ_r parameters from the finite element model and experimental data. Knowing that C_1 is dependent on the residual stress σ_r as described in Mitchell et al. (2003). In other words, if a set of output data are computed from the solutions determined by the finite element model, then, m data are created with input parameters known ($E_j, \sigma_{rj}, v_j \forall j = 1,2,..m$), it is possible to determine C_1 adjusting those output data in Equation 1.5. Posteriorly, C_1 is used to compute the residual stress σ_r using the experimental data for any Young's modulus chosen in Equation 1.5. For Young's modulus value, a value similar to materials with analogous mechanical characteristics is recommended, since the true solution is not this initial value.

In steps 4, 5, and 6; the main objective is to establish a model for constant, this is determined only from the simulations. $C_2(v)=(\alpha+\beta v)/(1-v)$ is presented here as a parametric equation, however, it should be noted that different values of of α and β have been calculated with numerical and analytical approximations, as outlined by Mitchell et al. (2003). Other methods for determining the Poisson's ratio have been explored by Tabata & Tsuchiya (1996). In our case, we propose numerical estimations obtaining a set of two parameters E_i and $v_i, \forall i=1,2$ that satisfy the load-deflection curve obtained experimentally. The $v_i, \forall i=1,2$ values can be fixed as a set of values to determine the corresponding Young's modulus as demonstrated in Chapter 2. Then, with all parameters determined (E_i, σ_r, C_1) and experimental data, $C_{2(i)}$ is obtained with both Poisson's ratios found. In this way, the correlated Young moduli are found by choosing the Poisson ratio values as extreme values. So, parameters α, β are calculated as follows

$$\alpha=\frac{v_2 C_{2(1)}\left(1-v_1\right)-v_1 C_{2(2)}\left(1-v_2\right)}{v_2-v_1},\ \beta=\frac{C_{2(2)}\left(1-v_2\right)-C_{2(1)}\left(1-v_1\right)}{v_2-v_1}. \tag{3.1}$$

Using α and β values, we can calculate any value of $C_2(v)$ with values of v_i known. With all parameters calculated until the step 7, the following error function can be mapped such as

$$e_{p(k)}(E,v)=\sqrt{\sum_{j=1}^{n}\left(\frac{P_{\exp(j)}-P(C_{2k}(v_k),E_k,w_{\exp(j)})}{\max(P_{\exp(j)})}\right)^2/n} \tag{3.2}$$

where subscript k means a set of parameters E_k and v_k determined for each load-deflection curve with *n* data. Equation 3.2 represent an error surface in which the minimum errors should be in the places where a set of E and v satisfy the experimental measurements. According to previous exploratory data analysis done in our study, it was found that a linear approximation can define the set of optimal solutions for E_k and v_k such as described in the step 8. Until this step, a set of parameters that approximate the analytical equation and the finite element model is found, this is due to that between both parameters elastic coupling exists. To compute a unique solution the following index is created

$$e_{c(k)}(E_k,v_k)=\sqrt{\sum_{i=1}^{m}\left(\frac{w^3_{\exp(j)}(x,y)-w^3_{FEM}(x,y)}{w^3_{\exp(j)}(x,y)}\right)^2/n}, \tag{3.3}$$

Equation 3.3 was established to compare a 30% of the displacement field between the finite element models and the measured data. The minimum value $\min\left|e_{c(k)}\right|, \forall k=1,2...,p$ indicates that the elastic parameters (E^* and v^*) are the best approximations for the load-deflection curves obtained experimentally. These values should satisfy the best conditions to reproduce the load and displacement curve obtained experimentally.

3.3 Comparisons between solution strategies presented in section 3.1

In order to compare both methodologies of simulation by FEA, several numerical examples were proposed. These are designed for the following film size $2\times2mm$, $2.5\times2.5mm$ and $3\times3mm$ all with a thickness of $v=0.3$. The following properties were considered for both models, such as;

$E = 236.3GPa, \sigma_r = 166MPa$ and $v = 0.3$. The loading conditions were defined by the application of a maximum pressure of $9.57kN$ imposed by 39 steps applied incrementally in the FEM model to guarantee the solving convergence which were obtained with implicit solutions. Figure 3.3a illustrates the results obtained for all proposed simulations, where the pressure and the maximum displacement (central point) are correlated. The label FEM I indicates that the residual stress application was imposed inside the film (Figure 3.1a) and FEM II refers to enforce the residual stress on the boundary. The model includes an extension, as detailed in Figure 3.1b.

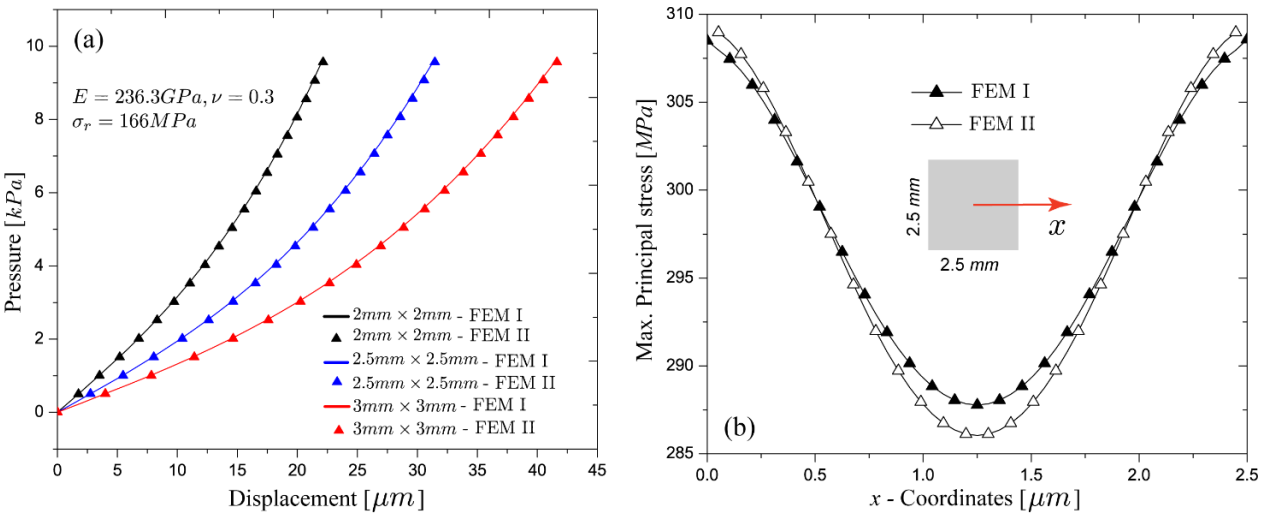

Figure 3.3. (a) Load-deflection comparison between models represented in Figure 3.1a and 3.1b. (b) Maximum principal stress comparison for a $2.5 \times 2.5mm$ film.

Figure 3.3a shows that the comparisons between the load-deflection curves presented small deviations among both, FEM I and FEM II models. However, these differences are caused by the stiffness effects which are introduced in order to impose the residual stress. The curves evidence that both models give very similar results, for example, FEM II present slightly lower stiffness with respect to FEM I model since the curves obtained with FEM II analysis move downward. To examine the variation among the stresses, the maximum principal stresses along the *x*-axis were calculated and represented in Figure 3.3b. A film $2.5 \times 2.5\ mm$ is considered for the calculations. Figure 3.3b illustrates that the stress distributions present two regions where can be distinguished the deviation of both methods. One is noted at the central point ($x = 1.25\ mm$) and then other at the boundaries ($x = 0\ mm$ and $x = 2.5\ mm$. The relative error among the minimal stress values obtained with FEM I (287.76 *MPa*) and FEM II (286 *MPa*) is 0.6%. On the boundaries, the computed error is about 0.25%; and in the rest of the domain were lower. These results demonstrate that both modeling approaches are close to each other, which indicates that both are acceptable to simulate the bulge testing. In this paper, all simulations presented in the following sections were performed using FEM II.

3.4 Identification of Young's modulus and Poisson's ratio for Si_3N_4

For the application of the proposed methodology described in section 3.2, three experiments were conducted on commercial silicon nitrate films (Si_3N_4) with $2\times 2mm^2$ of surface and $500nm$ of thickness. The tests were carried out in the apparatus described in Section 1.6 and the measurements obtained to represent the bulge surface are shown in Figure 3.4.

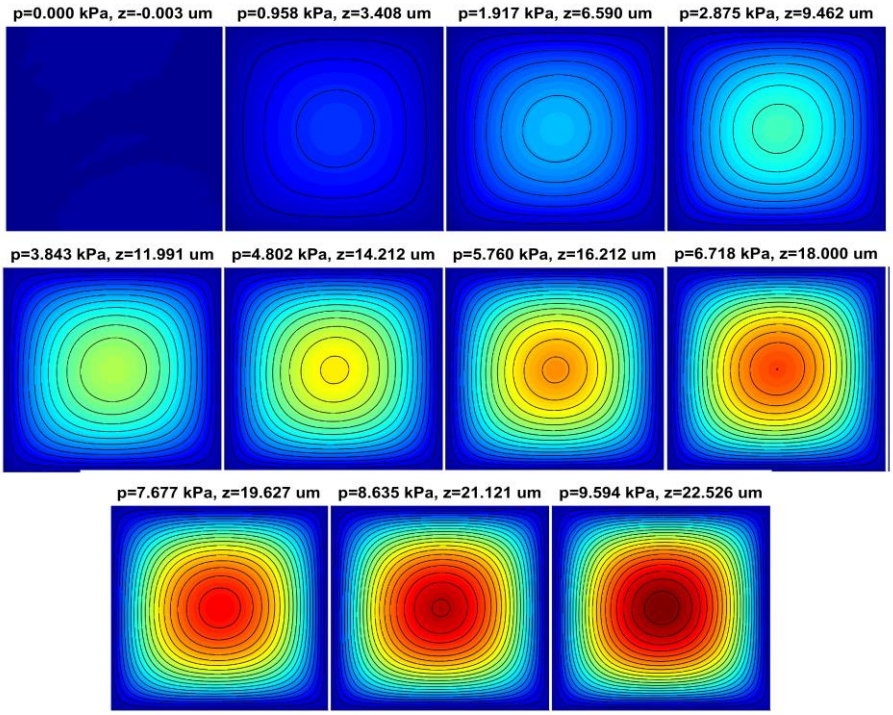

Figure 3.4. Experimental measurements of the displacement field z under different pressure conditions.

The thin films were pressurized until a maximum pressure of $9.59\,\text{kPa}$ which was applied incrementally. Following the procedures outlined in Figure 3.2, the firsts two steps were applied to determine the value of $C_1 = 3.373$ from simulations. Then, applying the step 3, the residual stress was computed as $\sigma_r = 166 \pm 3.6\,\text{MPa}$. Based on the steps 4 through 6 (see Section 3.2), the following constants were determined; $\alpha = 1.9690$ and $\beta = -0.4594$. It is important to denote that these parameters are used to determine the mapped values C_2 with Poisson's values estimated to compute the best approximation with the experimental data, as detailed in the steps 7 and 8. Figure 3.5a shows the error function $e_p(E,v)$ computed with Equation 3.2, this function is mapped with the elastic parameters expressed in the domains $E \in (200, 280)$ MPa and $v \in (0.2, 0.4)$. It is observed that there is a region in which the elastic values minimize the function $e_p(E,v)$. The minimum values are presented by dark blue, in this region $\mathbf{C}=\left\{ E^* \subset E \in \mathbb{R} \middle| v^* \subset v \in \mathbb{R} \right\}$, all pairs (E^*, v^*) satisfy the load-deflection curve with good accuracy, however, to select the best solution all pairs should be evaluated until satisfying $\min e_c(E^*, v^*) \le e_c(E^*, v^*)$. These results demonstrate that all elastic pairs provide a feasible solution to the bulged film, which indicates that the problem is mechanically coupled.

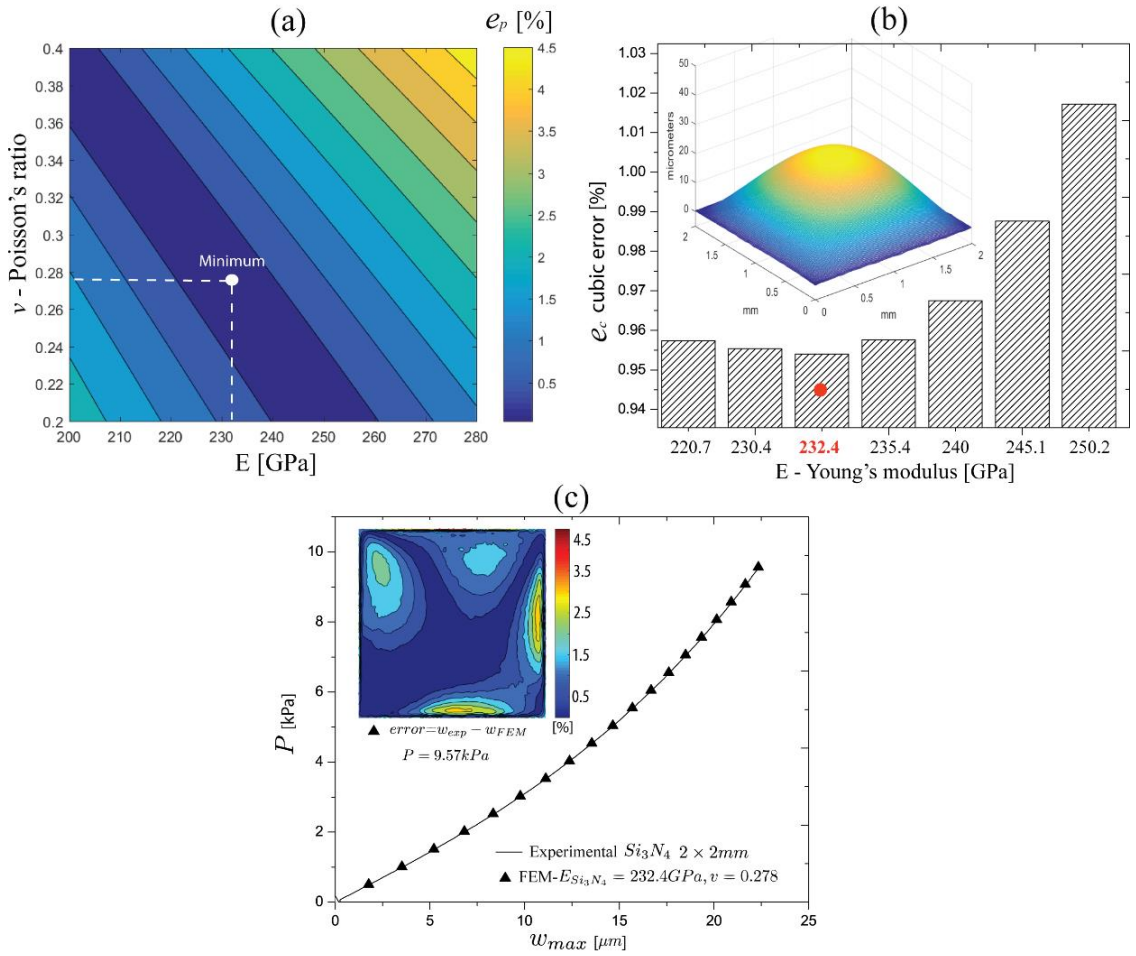

Figure 3.5. (a) Error function $e_p(E,v)$. (b) RMS cubic error scheme of the experimental setup. (c) Load-deflection curve comparisons.

As illustrated in step 9, the set of values that minimize $e_p(E^*,v^*) \approx 0$ (dark blue values) are used to perform finite element simulations to find an optimal solution inside the chosen values. Then, an optimal solution is found in the minimum of $\min e_c(E^*,v^*)$, for our test, it was determined as $E = 232.45 \pm 3$ MPa and $v = 0.278 \pm 0.01$ with three experiments analysed. The results are shown in Figure 3.5b. Based on the solutions found, a new simulation was conducted to compare the load-deflection curve determined by the FEA with experimental results. In Figure 3.5c is observed that the numerical solutions agree with the experimental data, computations were done to verify that calculated solution adjusts the measured data. Additionally, for the maximum state of pressure (9.59 kPa), there is evidenced the absolute error between finite element solution and experimental displacement field present errors less than 1% in most of the bulged domain. To compare the results of the square thin film, other experimental tests were performed on a rectangular thin film (Si_3N_4) of $3.5 \times 1.5mm^2$ of area and 100nm of thickness. Implementing the same procedures performed for the square thin film, the following constants were determined conducting the firts six steps (see Section 3.2); $\sigma_r = 125 \pm 5MPa, C_1 = 2.1, \alpha = 1.2513$, and $\beta = -0.7527$. Figure 3.6a shows the error function $e_p(E,v)$ presented in Equation (2) which in turn was computed with the parameters anteriorly expressed in the domains $E \in (200,280)$MPa and $v \in (0.2,0.4)$. It is observed that there is a region in which the elastic values minimize the function $e_p(E^*,v^*)$. These values are evaluated into cubic error

function $\min e_c(E^*, v^*)$ to determine the best pair of solutions. The best solution for this case was computed as $E = 235.45 \pm 4$ MPa and $v = 0.254 \pm 0.01$ with three experiments analysed. These values are comparable with the values determined for the thin square film. According to Figure 3.6b, the solution determined satisfied the experimental load-deflection curve and the relative error between the displacement fields was less than 2%.

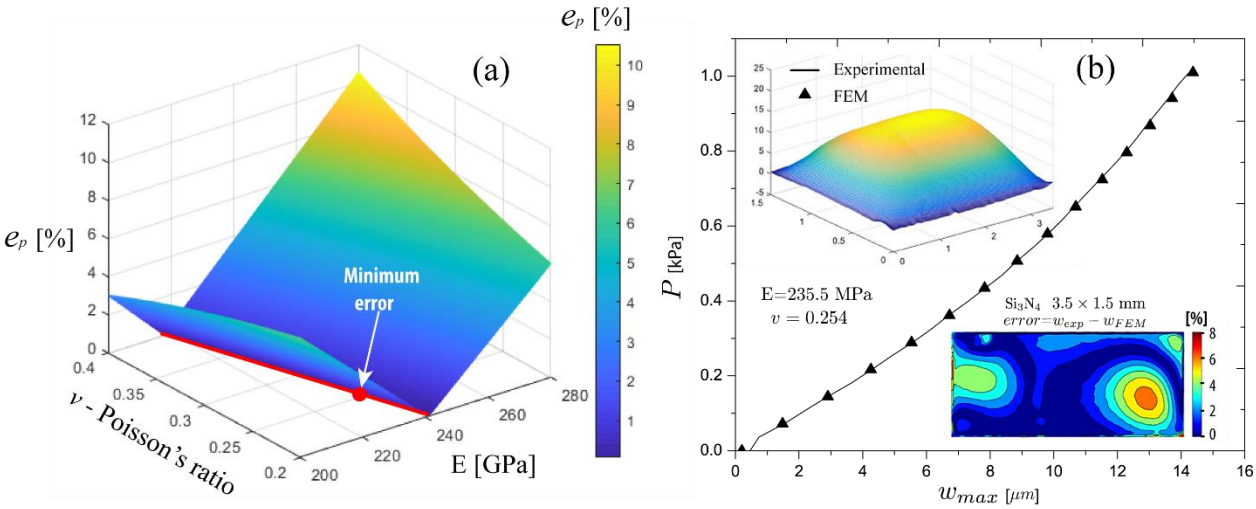

Figure 3.6. (a) Error function $e_p(E, v)$. (b) RMS cubic error scheme of the experimental setup. (c) Load-deflection curve comparisons.

The obtained properties of both commercial silicon nitrate films demonstrate that the procedures established by the proposed methodology satisfy the experimental results. Compared to other studies that set the elastic properties between 200 and 260 GPa (Vlassak & Nix, 1992; Karimi et al., 1997; Edwards et al., 2004; Boe et al., 2009; Tinoco et al., 2018a), the results are comparable. In Table 3.1 are summarized the elastic properties.

Table 3.1. Determined elastic properties for silicon nitride Si_3N_4 thin films

Square thin film		Rectangular thin film	
v	E [MPa]	v	E [MPa]
0.278	232.45 ± 3	0.254 ± 0.01	235.45 ± 4

3.5 Identification of Young's modulus and Poisson's ratio of a rectangular Au thin film

An experimental bulge test was conducted for a Gold (Au) film with $1.056 \times 4mm$ surface and $198.6nm$ of thickness. The experimental details for obtaining load deflection curves of a cracked film are illustrated in Preiß et al. (2017). Measurements of load and deflection were taken until the thin film was damaged. However, the elastic portion of the behaviour was extracted using a consideration on the load-deflection model to determine the elastic limits in the bulge problem (Holzer et al., 2017b). For example, if Equation (1.1) is divided by w_0 (maximum displacement), it is possible to obtain the following linear relationship

$$Y = C_1 \frac{\sigma_r t}{a^2} + C_2(\nu) \frac{Et}{a^4} X, \tag{3.4}$$

Where $Y = P / w_0$ and $X = w_0^2$. To establish an elastic limit during the bulge test (see Figure 3.7a), equation (3.4) should satisfy a linear relation. In Figure 3.7a is shown the relation between $X = w^2$ and $Y = P / w$ which was established from experimental data to validate the linear expression illustrated in Equation (3.4).

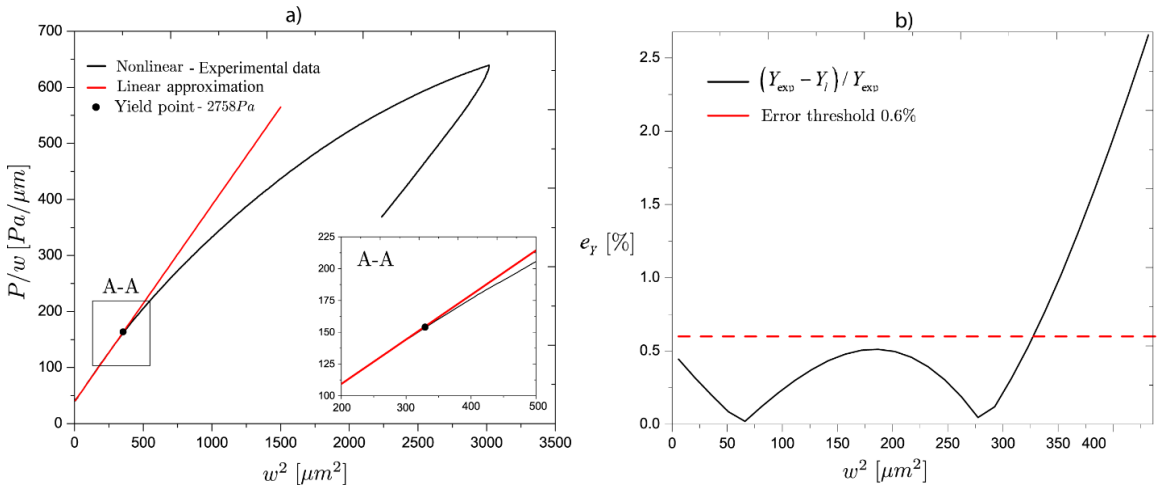

Figure 3.7. (a) Comparison between experimental data and the linear relation P / w_0 and w_0^2. (b) Error function with threshold in 0.6%.

In order to establish a deviation parameter for the linear relation, the data set between $w^2 \in (0, 250)$ was used to fit a linear approximation which is marked with red color in Figure 3.7a.

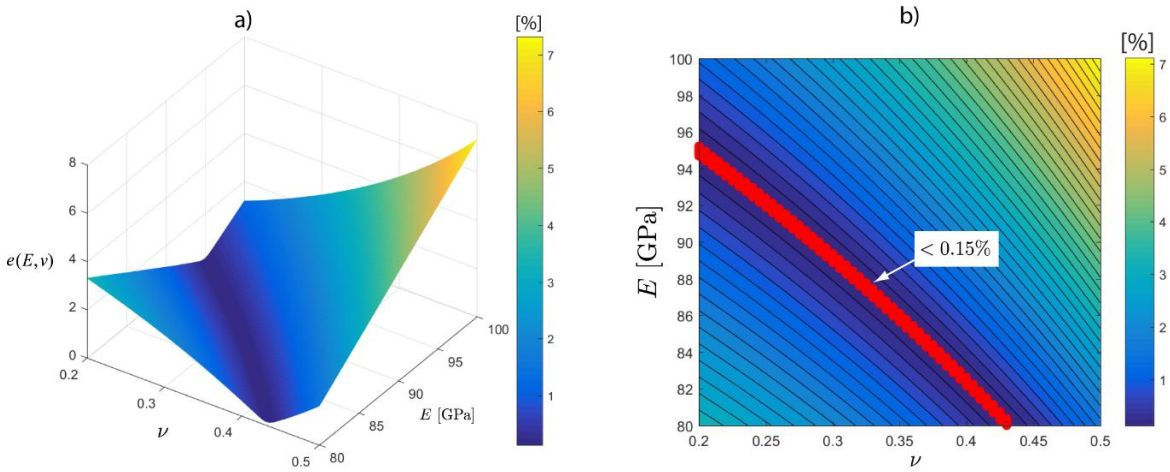

Figure 3.8. (a) $e_p(E,\nu)$ error function. (b) Set of $e_p(E,\nu)$ values lower than 0.15%.

To define a comparison parameter the following error function is established $e_Y = \left(Y_{\exp} - Y_l\right) / Y_{\exp}$, this function quantifies the deviation between Y_l (approximation) and $Y_{\exp}$ (experimental data). A threshold of 0.6 % is chosen to delimit the limit of the linear behavior in the bulge test. It is observed that the experimental data begins to deviate more than 0.6 % in $X = 325 \mu m^2$ as illustrated in Figure 3.7b, .With

this limit point, the load-deflection curve is reduced until 2.758kPa which is the limit pressure obtained from the experimental data. Applying the procedures described in section 3.2, the following constants were determined; for the Gold film $\sigma_r = 30.168MPa, C_1 = 1.83407, \alpha = 1.2809$ and $\beta = -0.7647$. Figure 3.8a shows the error function $e_p(E,v)$ established in Equation (3.2) which in turn was computed with the parameters anteriorly expressed in the domains $E \in (80,100)GPa$ and $v \in (0.2, 0.5)$. It is observed that there is a region in which the elastic values (E^*, v^*) minimize the function $e_p(E,v)$. As shown in Figure 3.8b, these were extracted with an error threshold of 0.15%. Based on these values, all pairs satisfy the load-deflection curve with good accuracy.

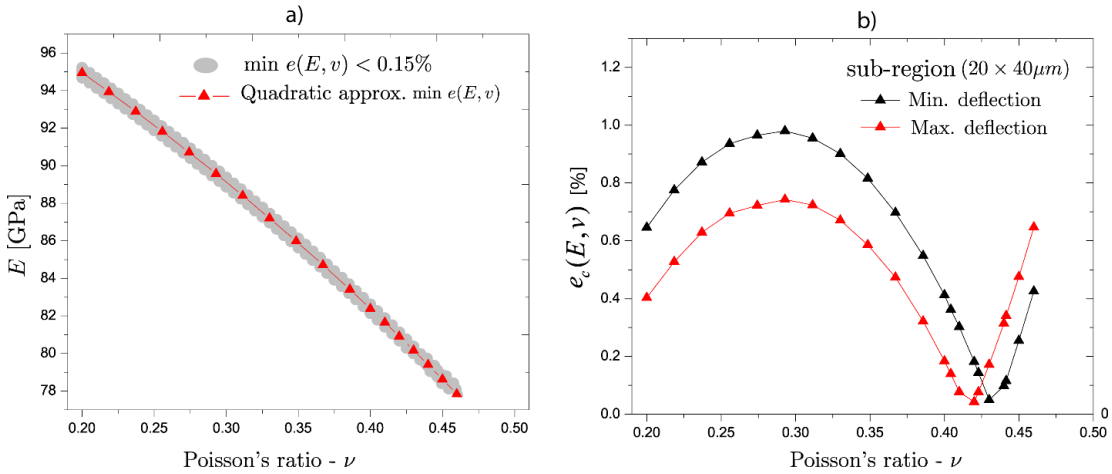

Figure 3.9. (a) E and v data set for $e_p(E,v) < 0.15\%$. (b) Error function $e_c(E,v)$ evaluated in the central sub-region.

To determine which pair (E,v) approximates better the experimental data of load-deflection, finite element simulations were running with the new extracted data set shown in Figure 3.9b and Figure 3.9a.

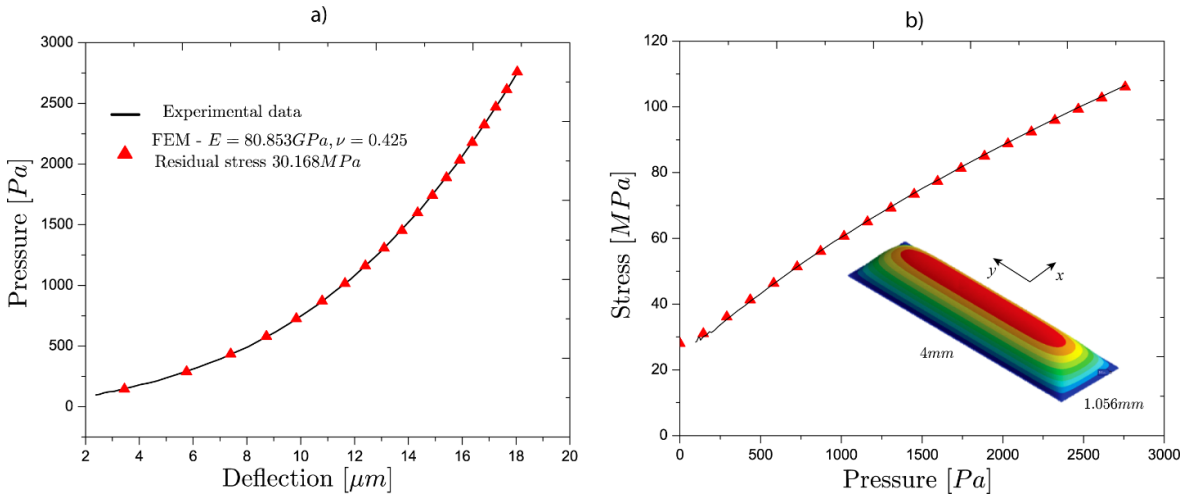

Figure 3.10. (a) Comparisons between FEA and experimental data. (b) Load-deflection. b) Stress vs. Pressure.

All load deflection curves obtained by FEA were compared using the error function $e_c(E,v)$ over a subregion sub-model (sub-region) that presents dimensions of 20x40 um located at the place of the maximum displacement. Comparisons were computed from displacements of 8 um, since after this

value the elastic parameters have more influence over the load-deflection model. Figure 3.9b shows error function $e_c(E,v)$ computed for the central sub-region, it observed that the minimum values of the Poisson's ratio are between 0.42 and 0.43. From these results the following elastic properties were extracted for the Gold film: $E = 80.853 GPa, v = 0.425$.

Table 3.2. Determined elastic properties for silicon nitride silicon nitride Si_3N_4 thin film

Authors	Elastic properties	
	v	E [GPa]
Present study	0.425	80.85
Saraswati et al. (2004)	---	84.4
Birleanu et al. (2016)	---	89
Liang & Prorok (2007)	----	75.9

New simulations were carried out to validate that the found properties satisfy the experimental data. In Figure 3.10 is seen that the elastic properties provide solutions that agree accurately with the pressure-deflection data. Aditionally, Figure 3.10b shows the relation among stress and pressure, in this result is visible in which value the stresses initiated, it means that the residual stresses coincided with the estimated input parameter. Finally, it is observed that the elastic properties of the gold thin film calculated with the current methodology agree with those it reported in Table 3.2. The comparisons shows only values determined for the Young's modulus and not for the Poisson's ration which can be considered as advantage of the proposed methodology in this chapter.

Chapter 4. Plasticity characterization in freestanding monolayer thin films

In this chapter, constitutive models are reviewed in order to calculate the stress and strain of bulged films, treating it as shell structures when deformed. In this way, equations for representing the equiaxial stress state are presented and applied to square films. Based on the deflection field proposed by Maier-Schneider et al. (1995), the curvatures can be computed locally in linear and nonlinear material states. The presented models are validated by virtual experiments using finite element analysis. A practical application based on these equations is presented to characterize elastoplastic material models.

4.1 Stress-strain distributions for freestanding square thin films subjected to bulge test

Bulge testing consists of applying uniform pressure over one side of a freestanding thin film exposed in a window of supporting material. This process causes a deflection outward that is represented by a displacement field $w(x,y)$ as illustrated in Figure 4.1a. In the manufacturing process, the film is deposited on a material stiffer that acts as the main support of it, working as a base substrate. During decades different approximations have been proposed to reproduce the shape of the bulged film to satisfy the equilibrium conditions that involve high-order derivatives. Timoshenko and Woinowsky-Krieger (1959) presented a set of approximations based on series that posteriorly Maier-Schneider et al. (1995) expanded a model with two more terms to improve the proposed solution by Timoshenko and Woinowsky-Krieger (1959). The modification presented a better description of the bulged shape in the evaluated examples. Maier-Schneider et al. (1995) proposed the expression for thin rectangular plates of size $2a \times 2b$, where $a \leq b$, but it was modified for a square thin film $a = b$ as follows

$$w(x,y) = \left(w_0 + w_1 \frac{(x^2+y^2)}{a^2} + w_2 \frac{x^2 y^2}{a^4} \right) \cos\left(\frac{\pi x}{2a}\right) \cos\left(\frac{\pi y}{2a}\right), \forall x, y \in (-a, a) \tag{4.1}$$

where the constants $w_1 = 0.401 w_0$ and $w_2 = 1.161 w_0$ depend on the maximum displacement w_0. In our study, Equation (4.1) is used to approximate the strain distributions (not dependent on the elastic properties) of a bulged square thin film. For this purpose, nonlinear shell theory is applied to assumptions adopted in Sander's shell theory (Budiansky, 1968). A structure can be considered a thin shell if the ratio between length and thickness is higher than 20. In this case, it considers that a bulged membrane is a thin shell since the thickness is minimal compared to transversal dimensions, which means that $2a/t \geq 20$, being a one half of the smaller length of the film and *t* the thickness. A thin shell has dominant flexure stiffness, whereas thick plates provide shear rigidity, which is not required in the bulging problem by the mechanical conditions of a thin structure.

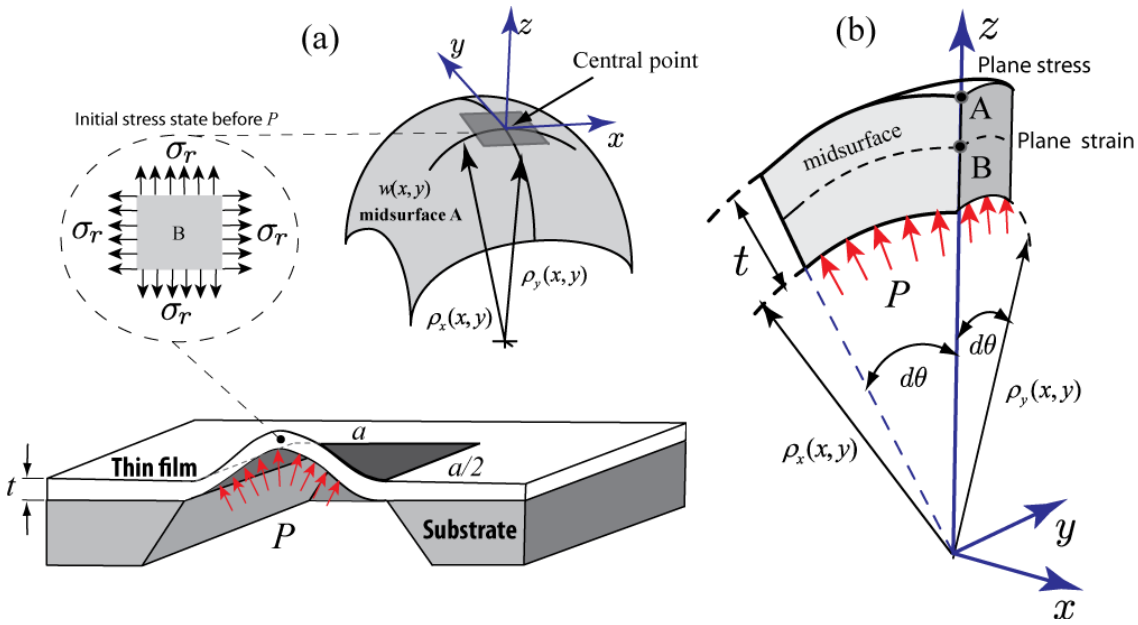

Figure 4.1. (a) Scheme of a bulged square membrane represented by the displacement field $w(x,y)$ and its directional curvature radios $\rho_x(x,y)$ and $\rho_y(x,y)$. (b) Representation of the stress state at the central point of a bulged square thin film.

Therefore, strains in the mid-plane are estimated from different contributions, including the nonlinear effects produced by large deformations; then, strains are computed as;

$$\varepsilon_{xx}(x,y)=\frac{\partial u_0}{\partial x}+\frac{1}{2A}\left(\frac{\partial w(x,y)}{\partial x}\right)^2+\frac{1}{A}\frac{w(x,y)}{\rho_x(x,y)}, \tag{4.2}$$

$$\varepsilon_{yy}(x,y)=\frac{\partial v_0}{\partial y}+\frac{1}{2A}\left(\frac{\partial w(x,y)}{\partial y}\right)^2+\frac{1}{A}\frac{w(x,y)}{\rho_y(x,y)}, \tag{4.3}$$

$$\gamma_{xy}(x,y)=\frac{1}{2A}\left(\frac{\partial w(x,y)}{\partial x}\frac{\partial w(x,y)}{\partial y}\right)^2+\frac{2}{A}\frac{w(x,y)}{\rho_{xy}(x,y)}, \tag{4.4}$$

where u_0, v_0 and $w(x,y)$ are the initial displacements fields at *x, y* and *z* position, $\partial u_0/\partial x$ and $\partial v_0/\partial y$ are initial axial strains. In the bulge test, the initial axial strains are associated with residual stresses corresponding to the manufacturing of the thin film. *A* is a constant that depends on the deformed geometry of shell, i.e. *A*=1 for cylindrical shape as described by Ventsel & Krauthammer (2001). $\rho_x(x,y)$ and $\rho_y(x,y)$ represent the radius of curvature at *x* and *y* directions associated with the curvatures $\kappa_{xx}(x,y)=1/\rho_x(x,y)$ and $\kappa_{yy}(x,y)=1/\rho_y(x,y)$ as illustrated in Figure 4.1b. Axes are oriented according to Figure 4.1. Curvatures of the middle surface are determined by the following relations (Ventsel & Krauthammer, 2001).

$$\kappa_{xx}(x,y) = -\frac{\partial^2 w(x,y)}{\partial x^2},\ \kappa_{yy}(x,y) = -\frac{\partial^2 w(x,y)}{\partial y^2},\ \kappa_{xy}(x,y) = -\frac{1}{2}\frac{\partial^2 w(x,y)}{\partial x \partial y}. \tag{4.5}$$

In a bulged thin film, initial axial strains are caused by residual stress σ_r which appears in the membrane as a consequence of the preparation technique; for a square thin film, it is computed by $\partial u_0/\partial y = \partial v_0/\partial y = \sigma_r(1-\nu)/E$ (in-plane strain state). Equations (4.2), (4.3), (4.4), and (4.5) can be solved using the displacement field $w(x,y)$ described in Equation (4.1). Calculations for the strain fields are detailed in Appendix A. Given the kinematic description of a bulged square thin film, generalized elastic stresses are determined by $\boldsymbol{\sigma} = \mathbf{C}\boldsymbol{\varepsilon}$, where through the middle surface (plane B in Figure 4.1b) the elastic matrix $\mathbf{C}$ for an isotropic material and plane-strain state is given by

$$\mathbf{C} = \frac{E}{(1+\nu)(1-2\nu)}\begin{bmatrix} 1-\nu & \nu & 0 \\ \nu & 1-\nu & 0 \\ 0 & 0 & (1-2\nu)/2 \end{bmatrix}. \tag{4.6}$$

where $\boldsymbol{\sigma} = \left[\sigma_{xx}(x,y) \quad \sigma_{yy}(x,y) \quad \tau_{xy}(x,y)\right]^T$ and $\boldsymbol{\varepsilon} = \left[\varepsilon_{xx}(x,y) \quad \varepsilon_{yy}(x,y) \quad \gamma_{xy}(x,y)\right]^T$. The set of equations described above determines stress-strain distributions in the elastic regime, but only if the elastic properties are known. On the other hand, a plane stress condition at point A (see Figure 4.1b) is considered for

$$\mathbf{C} = \frac{E}{(1-\nu^2)}\begin{bmatrix} 1 & \nu & 0 \\ \nu & 1 & 0 \\ 0 & 0 & (1-\nu)/2 \end{bmatrix}. \tag{4.7}$$

The set of equations described in this section serve to calculate stress-strain relations in the elastic regime if the elastic properties (E,ν) are determined previously by any of reported methods (Pan et al., 1990; Vlassak & Nix, 1992; Maier-Schneider et al., 1995; Edwards et al., 2004; Huang et al., 2007). For a square film, principal stresses are quantified by the following $\sigma_{1,2}(x,y) = \left(\sigma_{xx}(x,y) + \sigma_{yy}(x,y)\right)/2 + \tau_{xy}(x,y)$, and further, at the central point is known that $\tau_{xy} = 0$. Therefore, we can obtain that $\sigma_{1,2} = \sigma_{xx} = \sigma_{yy}$; this is known as equi-biaxial stress state. It indicates that the maximum stress directions are on the orthogonal directions to the sides of the square film (these coincides with *x* and *y*). It is necessary to denote that the equivalent stresses at the central point correspond with stresses at the directions *x* and *y.*

4.2 Stress-strain relations at the central point for a bulged square thin film

The equations presented in section 4.1 describe the elastic behavior of a square bulged film ($2a \times 2a$) with known elastic properties. However, those equations are not useful to characterize the elastic-plastic regime due to the linear nature of the models. Thus, a stress-strain model for freestanding square membranes is developed in this section To overcome this limitation. For this purpose, equation (4.1) is taken as reference or input. Then, let's consider the curvatures of the central point determined with the strain functions obtained as follows:

$$\frac{\partial w(x,y)}{\partial x}=\left(\frac{2w_2xy^2}{a^4}+\frac{2w_1x}{a^2}\right)\cos\left(\frac{\pi x}{2a}\right)\cos\left(\frac{\pi y}{2a}\right)-\frac{\pi}{2a}\sin\left(\frac{\pi x}{2a}\right)\cos\left(\frac{\pi y}{2a}\right)\left(\frac{w_2x^2y^2}{a^4}+\frac{w_1\left(x^2+y^2\right)}{a^2}+w_0\right), \tag{4.8}$$

$$\frac{\partial w(x,y)}{\partial y}=\left(\frac{2w_2x^2y}{a^4}+\frac{2w_1y}{a^2}\right)\cos\left(\frac{\pi x}{2a}\right)\cos\left(\frac{\pi y}{2a}\right)-\frac{\pi}{2a}\cos\left(\frac{\pi x}{2a}\right)\sin\left(\frac{\pi y}{2a}\right)\left(\frac{w_2x^2y^2}{a^4}+\frac{w_1\left(x^2+y^2\right)}{a^2}+w_0\right). \tag{4.9}$$

Acurvatures (second-order derivation) are computed for x - direction:

$$\frac{\partial w^2(x,y)}{\partial x^2}=-\frac{\pi^2}{4a^2}\cos\left(\frac{\pi x}{2a}\right)\cos\left(\frac{\pi y}{2a}\right)\left(w_0+w_1\frac{(x^2+y^2)}{a^2}+w_2\frac{x^2y^2}{a^4}\right)+\left(\frac{2w_2y^2}{a^4}+\frac{2w_1}{a^2}\right)\cos\left(\frac{\pi x}{2a}\right)\cos\left(\frac{\pi y}{2a}\right)-$$
$$\frac{\pi}{a}\cos\left(\frac{\pi y}{2a}\right)\sin\left(\frac{\pi x}{2a}\right)\left(\frac{2w_2xy^2}{a^4}+\frac{2w_1x}{a^2}\right), \tag{4.10}$$

and for y - direction

$$\frac{\partial w^2(x,y)}{\partial y^2}=-\frac{\pi^2}{4a^2}\cos\left(\frac{\pi x}{2a}\right)\cos\left(\frac{\pi y}{2a}\right)\left(w_0+w_1\frac{(x^2+y^2)}{a^2}+w_2\frac{x^2y^2}{a^4}\right)+\left(\frac{2w_2x^2}{a^4}+\frac{2w_1}{a^2}\right)\cos\left(\frac{\pi x}{2a}\right)\cos\left(\frac{\pi y}{2a}\right)-$$
$$\frac{\pi}{a}\cos\left(\frac{\pi x}{2a}\right)\sin\left(\frac{\pi y}{2a}\right)\left(\frac{2w_2x^2y}{a^4}+\frac{2w_1y}{a^2}\right). \tag{4.11}$$

For $x-y$ plane, the mixed curvature is determined as

$$\frac{\partial w^2(x,y)}{\partial x\partial y}==-\frac{4}{a^4}w_2xy\cos\left(\frac{\pi x}{2a}\right)\cos\left(\frac{\pi y}{2a}\right)+\pi^2\sin\left(\frac{\pi x}{2a}\right)\sin\left(\frac{\pi y}{2a}\right)\left(\frac{w_2x^2y^2}{a^4}+\frac{w_1\left(x^2+y^2\right)}{a^2}+w_0\right)-$$
$$\frac{\pi}{2a}\sin\left(\frac{\pi x}{2a}\right)\cos\left(\frac{\pi y}{2a}\right)\left(\frac{2w_2x^2y}{a^4}+\frac{2w_1y}{a^2}\right)-\frac{\pi}{2a}\cos\left(\frac{\pi x}{2a}\right)\sin\left(\frac{\pi y}{2a}\right)\left(\frac{2w_2xy^2}{a^4}+\frac{2w_1x}{a^2}\right). \tag{4.12}$$

To determine a set of kinematic equations that in $x-$direction, the derivatives should be evaluated in $y=0$ such that;

$$\frac{\partial w(x,0)}{\partial x}=\left(\frac{2w_1x}{a^2}\right)\cos\left(\frac{\pi x}{2a}\right)-\frac{\pi}{2a}\sin\left(\frac{\pi x}{2a}\right)\left(\frac{x^2}{a^2}+w_0\right), \tag{4.13}$$

$$\frac{\partial w^2(x,0)}{\partial x^2}=-\frac{\pi^2}{4a^2}\cos\left(\frac{\pi x}{2a}\right)\left(w_0+w_1\frac{x^2}{a^2}\right)+\left(\frac{2w_1}{a^2}\right)\cos\left(\frac{\pi x}{2a}\right)-\frac{\pi}{a}\sin\left(\frac{\pi x}{2a}\right)\left(\frac{2w_1x}{a^2}\right), \tag{4.14}$$

$$\frac{\partial w^3(x,0)}{\partial x^3}=-\frac{w_1x\pi^2}{a^4}\cos\left(\frac{\pi x}{2a}\right)+\left(\frac{\pi^3}{8a^3}w_0-w_1\frac{3\pi}{a^3}+w_1\frac{\pi^3x^2}{8a^5}\right)\sin\left(\frac{\pi x}{2a}\right), \tag{4.15}$$

$$\frac{\partial w^4(x,0)}{\partial x^4} = -w_1 \frac{3x\pi^3}{4a^5}\sin\left(\frac{\pi x}{2a}\right) + \left(\frac{\pi^4}{16a^4}w_0 - w_1\frac{5\pi^2}{2a^4} + w_1\frac{\pi^4 x^2}{16a^6}\right)\cos\left(\frac{\pi x}{2a}\right), \tag{4.16}$$

For the central coordinates $x=0$ and $y=0$ (localization at the central point), we have that

$$\kappa_{xx}(0,0) = \kappa_{yy}(0,0) = \frac{\pi^2 w_0}{4a^2} - \frac{2w_1}{a^2} \approx \frac{5\pi^2}{30}\frac{w_0}{a^2}, \ \kappa_{xy}(0,0) = 0. \tag{4.17}$$

It is important to point out that for a freestanding square film under bulging pressure, the stress state at the central point does not contain shear stress, at least from a theoretical point of view.

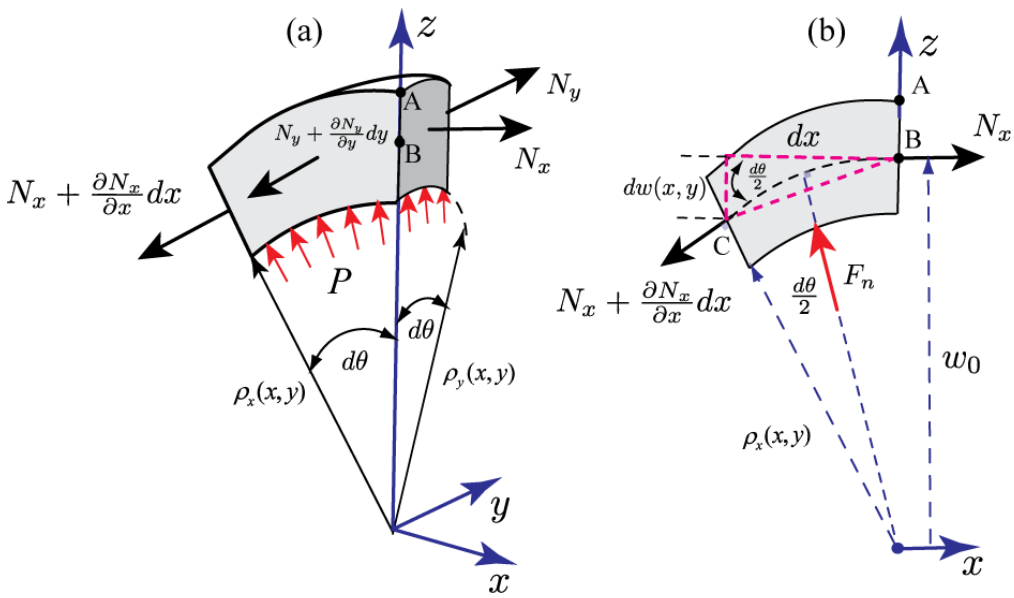

Figure 4.2. Differential element at the central point of a square thin film. (a) Stress state. (b) Kinematic approximations.

This is due to that there are no rotations, and its curvature κ_{xy} is null at the central point, it can be verified with equation (5). At the central point, the bulging effect produces an equi-biaxial stress state in-plane stress (point A, see Figure 4.2) and a triaxial stress state in-plane strain (point B). In Figure 4.2, a differential element that describes the equilibrium at the intersection of central planes *x-z* and *y-z* is represented. Moments are not considered in the central part by the equi-biaxial stress effect in a square film since in the bulging conditions; the thin films present negligible bending stiffness in this location. The force caused by the pressure *P* is calculated by $F_n = Pd\theta^2\rho_{x0}\rho_{y0}$, and the stretching axial force at *x*-direction is given by $N_x = \sigma_{xx0}\rho_{y0}td\theta$, where $\rho_{x0} = \rho_x(0,0)$, $\rho_{y0} = \rho_y(0,0)$ and $\sigma_{xx0} = \sigma_{xx}(0,0)$. Applying equilibrium conditions, specifically evaluating resultant moments about point C (*y*-direction), it is determined that

$$-N_x\left(\left(\rho_{x0} + \frac{t}{2}\right)d\theta\cos\left(\frac{d\theta}{2}\right)\right) + F_n\left(\rho_{x0} + \frac{t}{2}\right)\frac{d\theta}{2} = 0\,. \tag{4.18}$$

By solving equation (4.18), the following expression is obtained

$$\sigma_{xx0} = \frac{P}{2t}\rho_{xx0} = \frac{P}{2t\kappa_{xx0}}\ , \tag{4.19}$$

where $\kappa_{xx0} = \kappa_{xx}(0,0)$. Equation (4.19) represents a classical solution reviewed by different authors (Xu and Liechti, 2010; Santos et al., 2010; Ghanem et al. 2017; Shafqat et al., 2018) which demonstrated that the stresses depend on the curvatures generated by bulged surface. If these are known, stresses can be estimated as in the case of circular (equal to σ_{xx0}) and long rectangular films ($2\sigma_{xx0}$). Note that elastic constants of the film are not present in the Eq. (4.19); stresses are derived from the known value of applied pressure and curvature. In order to complete the calculation of the stress, equation (4.17) is replaced into equation (4.19) obtaining that

$$\sigma_{xx0} = \frac{4Pa^2}{2\left(\pi^2 w_0 - 8w_1\right)t} \approx \frac{3}{10}\frac{Pa^2}{w_0 t},\ \text{ If }\ \sigma_r < \sigma_{xx0}. \tag{4.20}$$

In equations (4.2), (4.3) and (4.4), strains were derived from the shell theory. Then, by replacing rotations and curvatures at the central point, the strain expression is calculated as follows

$$\varepsilon_{xx0} = \frac{\partial u_0}{\partial x} + \frac{1}{2A}\left(\frac{\partial w(0,0)}{\partial x}\right)^2 - \kappa_{xx0}\frac{1}{A}\left(w_0 + z\right), \tag{4.21}$$

By substituting equation (4.17) into (4.21), the strain at the central point is computed finally as

$$\varepsilon_{xx0} = \frac{(1-\nu)\sigma_r}{E} + \frac{5\pi^2}{30\sqrt{3}}\frac{{w_0}^2}{a^2}. \tag{4.22}$$

It is important to mention that equations (4.20) and (4.22) represent the stress-strain relations at the maximum deflection point (mid-surface) of a freestanding square thin film. In the last few years, the characterization of rectangular films was preferably performed for membranes with aspect ratio $b \geq 4a$. The basis for this preference was the simplicity of assuming a bulged film shape as a cylindrical portion (Schweitzer & Göken et al., 2007; Javed et al., 2016). With this consideration, the curvatures were estimated in a simple way; therefore early-stage works (Tabata et al., 1989; Vlassak & Nix, 1992; Xiang et al., 2005) presented the following relations for the stress, as follows

$$\sigma_0 = \frac{1}{2}\frac{Pa^2}{w_0 t}, \tag{4.23}$$

and for the strain as

$$\varepsilon_0 = \frac{\partial u_0}{\partial x} + \frac{2}{3}\frac{{w_0}^2}{a^2}. \tag{4.24}$$

Establishing a stress relation between stress models (equations (4.20) and (4.23)) established for membranes with aspect ratio $b/a = 1$ and $b/a = 4$, it is obtained that

$$\frac{\sigma_{xx0}}{\sigma_0} = \frac{3}{5}. \tag{4.25}$$

Equations (4.20) and (4.22) represent new models for characterizing the stress-strain relations of freestanding square thin films. In relation to a rectangular membrane $a/b = 4$, the stresses generated in a square film are less of approximately 40% for the same pressure state, as described the relation between stress models. It verifies that aspect ratio influences the bulged shape (Vlassak & Nix, 1992; Lee et al., 2007). The main conclusion denotes that stresses are higher in rectangular membranes.

4.3 Description of the elastoplastic behaviour of square thin films

Let's consider a rectangular thin film $2a \times 2b$, such that $a \leq b$, pre-stressed by residual stress σ_r and made of an isotropic elastic material that fulfills linear stress-strain relation. Under a pressure *P*, the film is deformed by the action of the bulged surface. In those conditions, Tabata et al. (1989) proposed a classical analytical solution that relates w_0 and *P* as described in Equation (1.4).

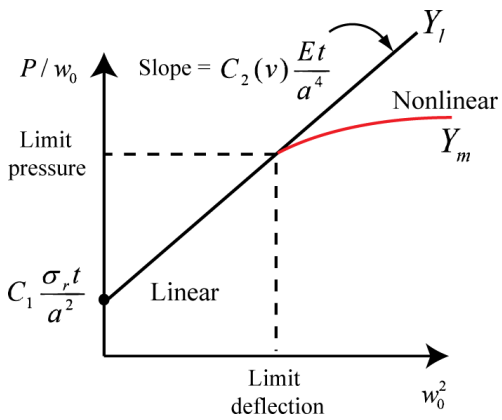

Figure 4.3. Linear relation obtained from the load-deflection curve.

Several models and numerical estimations have been discussed and proposed for both C_1 and $C_2(v)$ (Maier-Schneider et al., 1995; Mitchell et al., 2003; Overman et al., 2019), in our study, $C_2(v)$ is represented by the general equation presented in Equation (1.5), which depends on Poisson's ratio v ; α and β are constants to be determined. In real applications, experimental data obtained for w_0 and *P* are adjusted by least-square fitting with the aim to determine σ_r and *E*. This is possible if C_1 and $C_2(v)$ are known. However, the values of C_1 and $C_2(v)$ differs as reported by Mitchell et al. (2003). Considering all the mentioned parameters, we can divide Equation (1.4) by w_0 obtaining that

$$Y = C_1 \frac{\sigma_r t}{a^2} + C_2(v)\frac{Et}{a^4} X, \tag{4.26}$$

where $Y = P / w_0$ and $X = w_0^2$. Equation (4.19) is a linear expression that can be used to establish an elastic limit during the bulge test (Huang et al., 2007; Youssef et al., 2010; Holzer et al., 2017b). According to Figure 4.3, if there is deviation respect to the linear part, it indicates that nonlinear material effects (plastic stresses) are introduced on the thin film in the bulging process. To establish a deviation between Y_l (linear) and Y_m (measured), the following error is established as follows

$e_Y = (Y_m - Y_l)/Y_m$. To define a threshold error among Y_l and Y_m, we will consider an error $e_Y \geq \phi$ to determine the limit pressure P_l and limit displacement w_l. The threshold defines the pressure limit in which plasticity effects are introduced in the bulged membrane. Therefore, the yield stress σ_{yp} (Eq. 4.20) and total strain in the elastic threshold ε_{yp} (Eq. 4.21) are computed as follows

$$\sigma_{yp} \approx \frac{3}{10}\frac{P_l a^2}{w_l t},\ \varepsilon_{yp} = \frac{(1-\nu)\sigma_r}{E} + \frac{5\pi^2}{30\sqrt{3}}\frac{w_l^2}{a^2}. \tag{4.27}$$

To reconstruct the plastic material behavior a correction should be done in the total strain using yield stress and Young modulus (know values), then

$$\varepsilon_{pl} = (\varepsilon_{xx,0} - \varepsilon_{yp}) + \frac{\sigma_y}{E}.\forall \varepsilon_{xx,0} > \varepsilon_{yp}. \tag{4.28}$$

The analytical equations reviewed and developed show that with the classical load-deflection model is possible to reconstruct the material model for the plastic regime computed with equations (4.27) and (4.28).

4.4 Comparison between stress and strain distributions in an elastic square thin film

In section 4.1, Equations (4.2) and (4.6) were introduced to calculate the elastic linear relations among the stress and strain fields in a bulged thin film which can be determined if the elastic properties are known. It is most favorable to calculate these distributions from analytical solutions since finite element computations require a high time-demand if large volumes of thin films are tested. Equation (4.1) represents the displacement field that follows the membrane shape after being bulged and the simplicity of $w(x,y)$ is due to that it is only dependent on the maximum deflection w_0. So, if maximum displacements are known from the load-deflection curve, it is possible to reproduce the tridimensional shape of each deformed state in any regime.

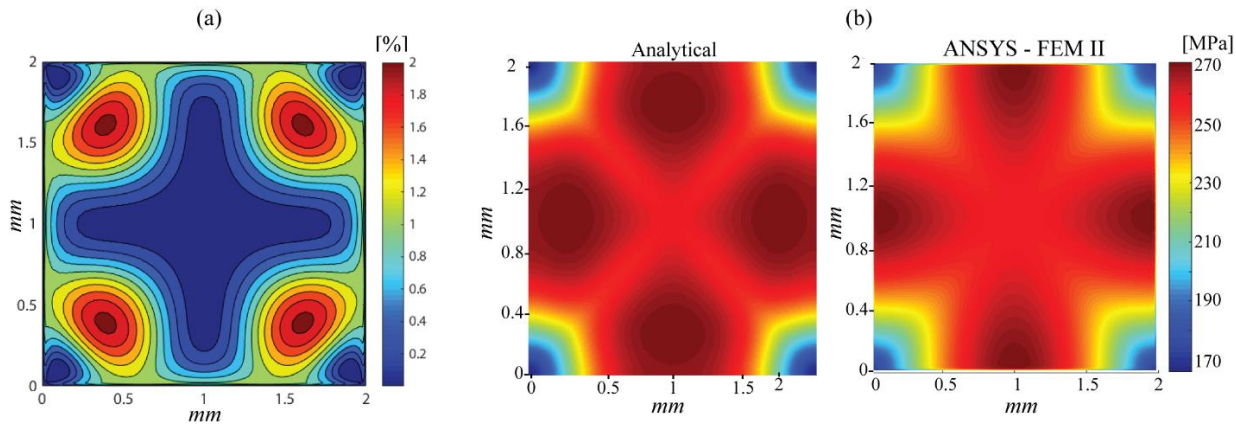

Figure 4.4. (a) Relative displacement error between FEM II solutions and $w(x,y)$. (b) Comparison of the maximum principal stress among FEM II and the analytical solution.

Maier-Schneider et al. (1995) proposed some values for the following constants $w_1 = 0.401 w_0$ and $w_2 = 1.1611 w_0$, and they demonstrated that $w(x,y)$ presented an accurate experimental correlation with the bulged shape in the studied cases. Authors did not report how w_1 and w_2 were obtained; but, these can be determined by minimization between experimental data and $w(x,y)$.

Let´s consider a thin film of size 2×2 *mm* and thickness of $500\ \mathrm{nm}$ subjected to a bulge test that achieves a maximum pressure state of $P = 9.57\ \mathrm{kPa}$. The material properties are the following $E = 236.3\ \mathrm{MPa}, v = 0.3$ and $\sigma_{r(j)} = 166\ \mathrm{MPa}$. The bulge test was simulated by means of FEA (proposed method explained in above Chapters 2 and 3) obtaining a maximum deflection of $w_0 = 22.154\ \mu\mathrm{m}$ for the maximum pressure. Then, the displacement field $w(x,y)$ (see eq. 4.1) is compared with the bulge surface calculated by FEA using the absolute relative error, as shown in the colormap shown in Figure 4.4a. The result indicates that the central region agrees quite well with numerical solutions since the relative errors (analytical solutions) are quite acceptable (less than 0.2%). Largest errors are found close to the corners, which reach 2% in its maximum; it can be concluded that the finite element solutions approximated with high accuracy the described bulged shape. In order to verify these differences in detail, we computed maximum principal stresses $\sigma_{1,2}$ for comparison between the FEM results and the analytical expressions presented, using the following computation of principal stresses as a reference:

$$\sigma_{1,2} = \frac{\sigma_{xx}(x,y) + \sigma_{yy}(x,y)}{2} \pm \sqrt{\left(\frac{\sigma_{xx}(x,y) - \sigma_{yy}(x.y)}{2}\right)^2 + \tau_{xy}^2(x,y)}, \tag{4.29}$$

Figure 4.4b depicts the maximum principal stress distributions calculated analytically and by FEM. It is evidenced by simple inspection that the largest principal stresses appeared at the central part of the boundaries for both cases. However, remarkable differences in the way that stresses are distributed over the film domain are noticed. The deviations correspond with second-order derivatives since the stress calculations depend directly on the strains, and it relates the contributions of each deformation, axial, bending, and large deflections on the function $w(x,y)$. The principal stresses distribution are shown in figures 4.5a, 4.5b, and 4.5c, where Figure 4.5a (analytical results) and Figure 4.5b (FEA results) σ_1 is visualized as a 3D surface. To compare the FEA results quantitatively, the curves correspoding along of the x -direction are related in Figure 4.5a. It is observed that from $x \in (0.25, 1.75)$ mm both results are well correlated, specially the central point of the film. It confirms the numerical solution obtained by FEM is reproduced by the analytical model. Furthermore, Figure 4.5c and 4.5d represent the minimum principal stress and Von Mises stress, which are commonly used for stress analyses. In Figure 4.6a, $\varepsilon_{xx}(x,1)$ obtained from Equation (4.2) is compared with the numerical solutions (FEM results).

The correlations of both solutions exhibit the same trend, but the analytical solution underestimates the strains with a maximum relative error of 3.5% on the boundaries. In the middle region $x \in (0.5, 1.5)$ *mm*, strains overestimate the numerical results. Given that the calculated curve is a projection of the strain field, inside the figure, the strained surface $\varepsilon_{xx}(x,y)$ is illustrated. It is important to remark that numerical computations are approximations and these are taken as reference in our case, since $w(x,y)$ is determined by the parameters w_0, w_1 and w_2.

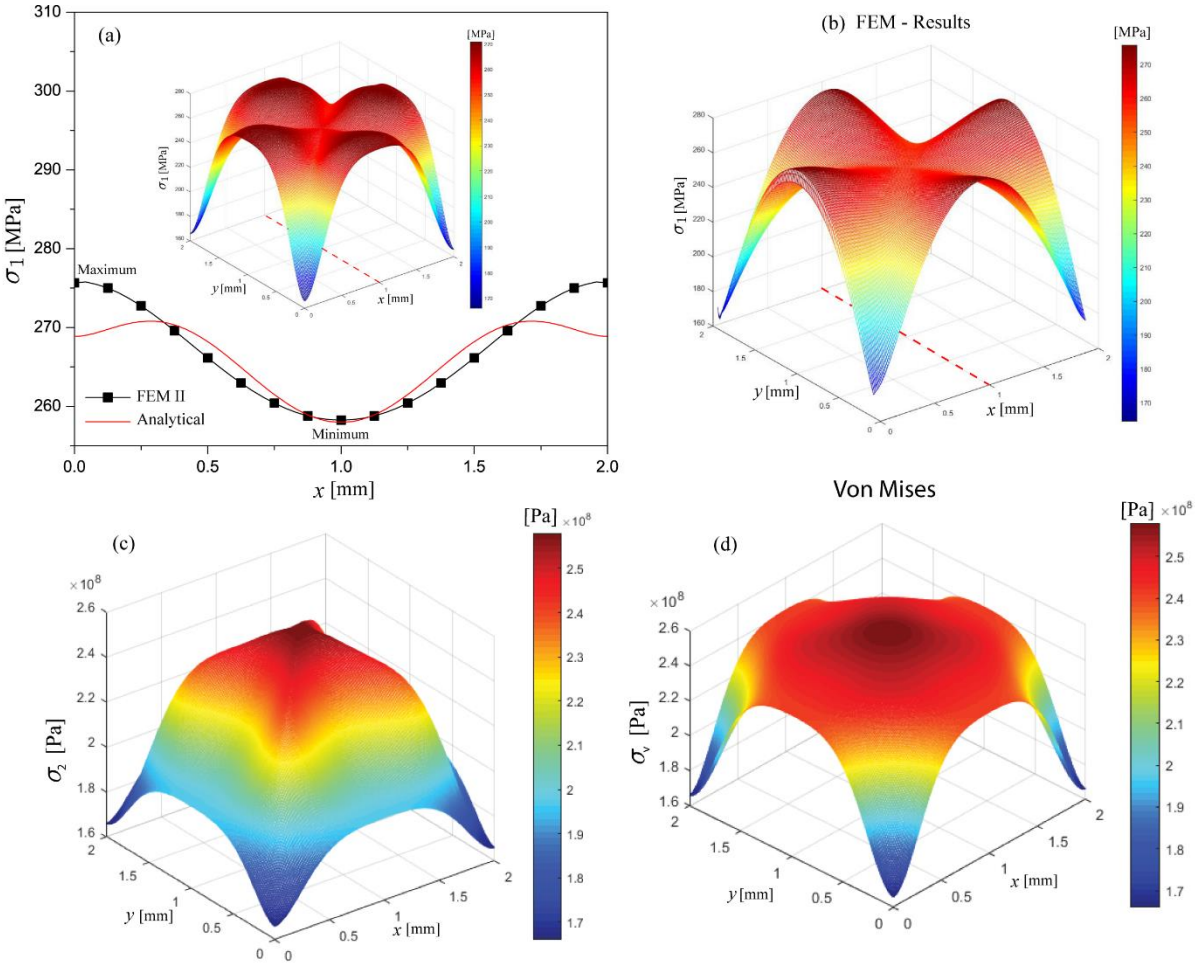

Figure 4.5. (a) Comparisons between σ_1 obtained by FEM and the proposed analytical equation. (b) Maximum principal stress determined by FEM. (c) Minimum principal stresses obtained analitically. (d) Von Mises stresses determined analitically.

In practical applications, these parameters should be fitted from the experimental data that are used. The stress field and its projection on $(x,1)$ are computed applying Equation (4.7). Both are illustrated in Figure 4.6b in the same way as for strains. It is seen that the difference in the boundary stresses is 10 MPa, and the relative errors are minimized close to the central part of the film. Comparisons showed in Figure 4.6 can be used for the determination of better relations between w_0, w_1 and w_2. In order to observe if the curvatures obtained through $w(x,y)$ are well correlated with the numerical results, an interest region delimited by $x \in (0.5, 1.5)$ *mm* is demarked in gray color in Figure 4.6. Applying equation (4.5) and equations (4.10), (4.11) and (4.12), the curvatures $\kappa_{xx}(x,y)$, $\kappa_{yy}(x,y)$ and $\kappa_{xy}(x,y)$ were calculated, and these are depicted in Figure 4.7a. The axes (x,y) are shifted by 1 to set the zero as the central point.

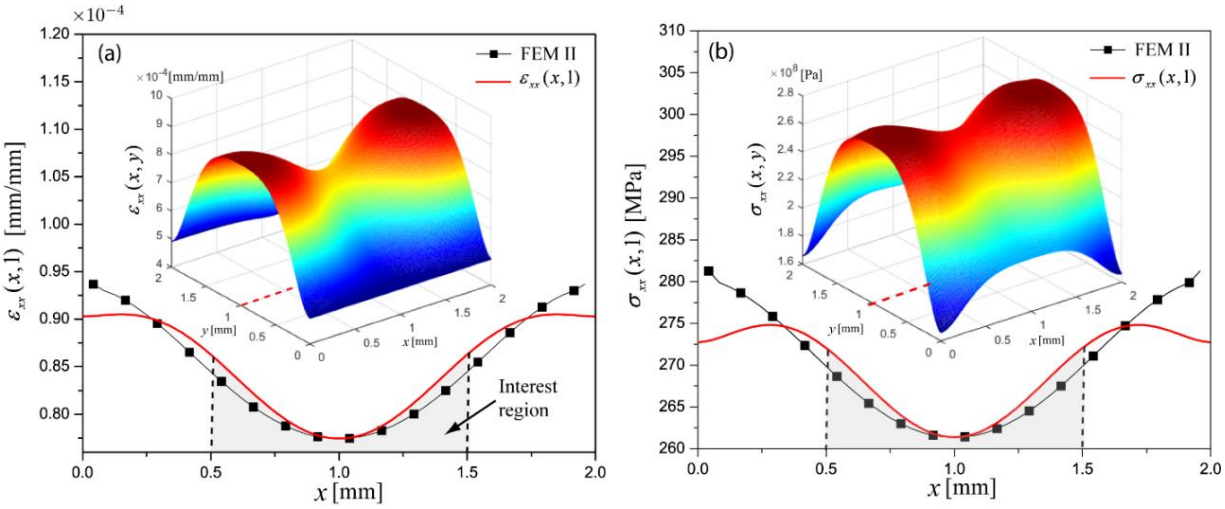

Figure 4.6. Calculations for $P = 9.57\ \mathrm{kN}$ a) Strain field at *x*- direction. b) Stress field at *x* - direction.

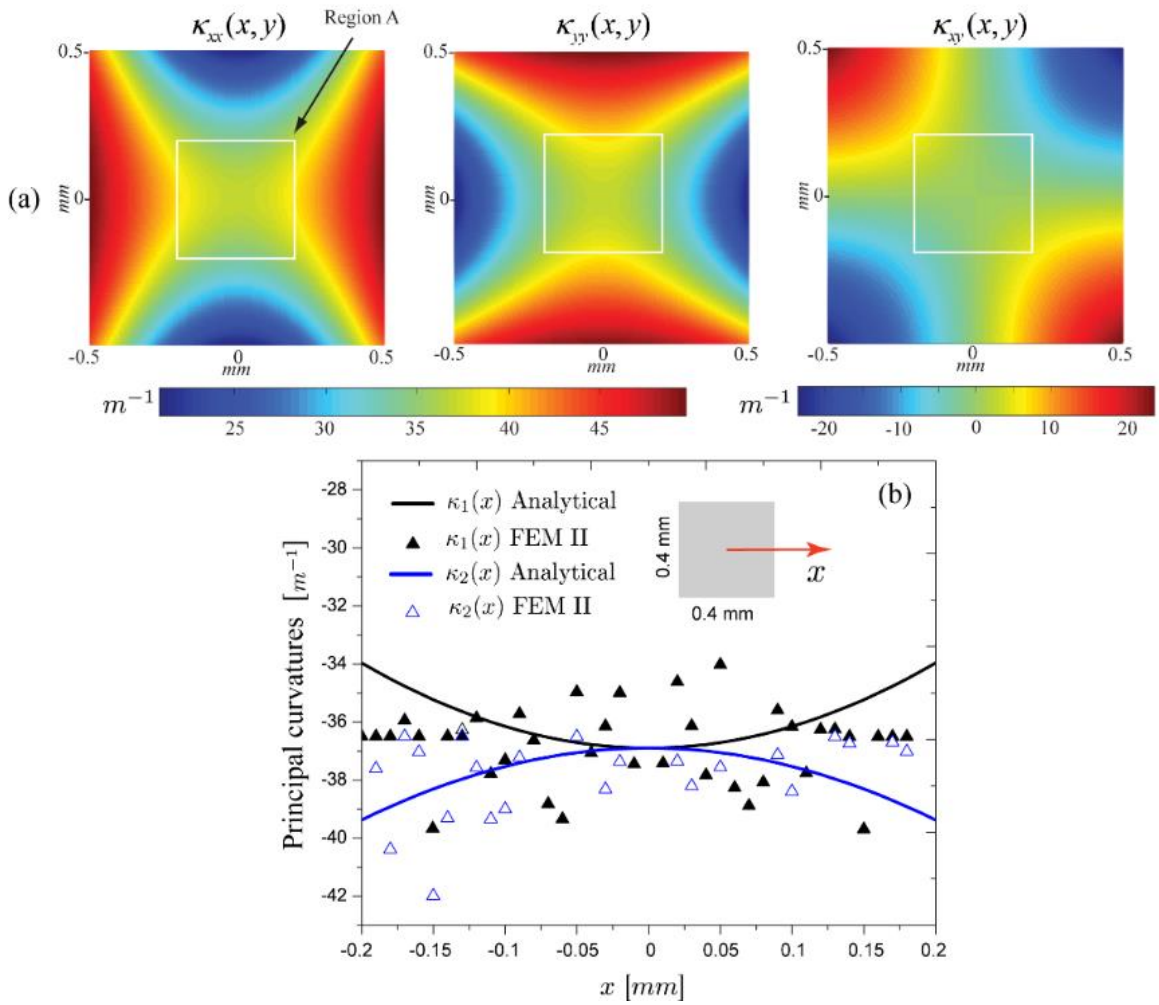

Figure 4.7. (a) Directional curvatures $\kappa_{xx}(x,y)$, $\kappa_{yy}(x,y)$ and $\kappa_{xy}(x,y)$ determined analytically. (b) Comparison among the principal curvatures.

The segmented region A (interest region) in the image shows that the directional curvatures oscillate between 34 m^{-1} and 39 m^{-1} in the central part, where $\kappa_{xx}(x,y)$ and $\kappa_{yy}(x,y)$ evidence the symmetrical nature of the bulged surface. Further, $\kappa_{xy}(x,y)$ it indicates that over the central part there are no twist curvatures since these are zero. Principal curvatures κ_1 and κ_2 were determined for both approaches to compare their deviations, as shown in Figure 4.7b. It is noted that curvatures determined by FEM II are scattered. This is due to that the calculations were done over the displacement results that use second-order functions, which produces constant curvatures on each finite element. On the other hand, analytical solutions are represented by high order functions; for this reason, these are continuous. It is observed that only a small region presents a good correlation among the curvatures $x \in (-0.2, 0.2)$, which means that $w(x,y)$ it only satisfies the second derivative in a limited area. It is essential to point out that all results shown in this section can only be used in the elastic regime.

4.5 Stress model (Eq. 4.20) validation for elastic square thin films

Equation (4.20) developed to calculate the stresses located on the central point of a square thin film is evaluated for different membrane sizes in this section. The elastic square film $2mm \times 2mm$ used in the previous section is considered a first comparison example, including their pressure states. Figure 4.8 shows the maximum principal stresses obtained by FEM analysis, equations (4.20) for square thin films, and (4.23) for rectangular thin films. Both solutions (FEM and Eq. 4.20) demonstrate a numerical correspondence from specific pressure values, specifically 4.5kPa; which indicates that the deviation among these diminished when the elastic effects are more effective . It is pointed out that at the beginning of a load-deflection curve, the residual stress is predominant in the bulging problem (Mehregany et al, 1997; Shojaei et al. 1998; Ghanem et al., 2017). The deviations evidence that a correction model could be introduced to act in the first part of the load-deflection curve.

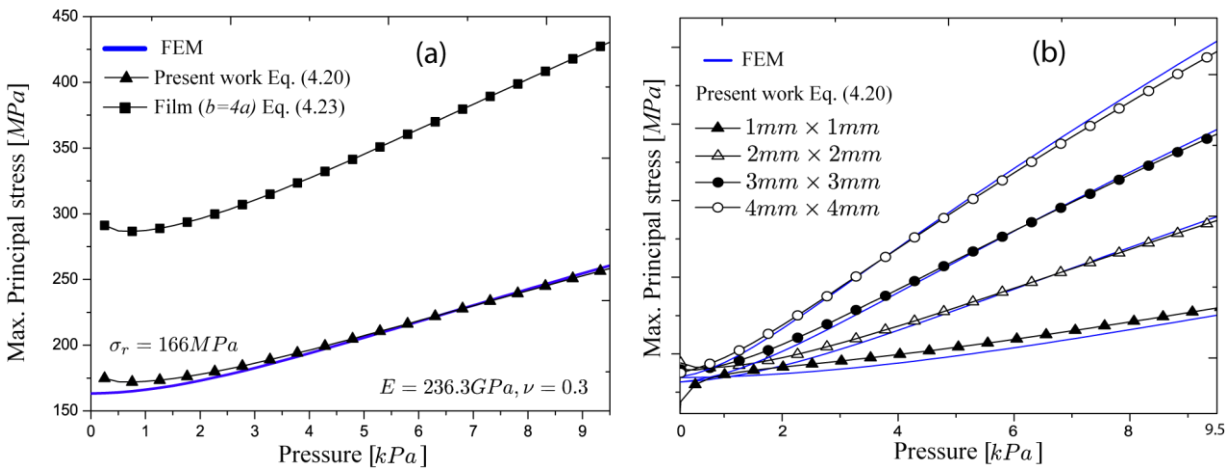

Figure 4.8. (a) Maximum principal stress comparisons. (b) Stress comparisons for different sizes of square films.

The classical equation (4.23) was applied for the $2 \times 2mm$ to compare the solutions with the proposed model in (4.20); equation (4.23) was developed for rectangular films, which is applied for aspect ratio *b/a* equal or higher than 4. Our purpose is to show the differences between stress values since both stress models present dependency with the parameter *a.* In the showed results, we observe that the differences are remarkable among the curves with triangular (square film) and square (rectangular) markers; the main characteristic is that stresses are clearly over-dimensioned.

In this example, the residual stress is assumed as unknown to impose the same pressure and deflection condition on both equations. According to the classical work done by Tabata et al. (1989), equation (4.23) is valid only for films with the aspect ratio $b/a >= 4$ as discussed in section 4.2. However, the same model has been used for square geometries in some cases since a stress equation for square films is not available in the reviewed literature as mentioned above, this is not a correct approach as is clearly seen in Figure 4.8a. Additional information about the validity and limitations of the rectangular model used to determine the stresses are discussed by Neggers et al. (2012b).

Figure 4.8b shows approximations for different sizes, with fixed thickness, and considering the elastic properties and residual stress as in Figure 4.8a. For square films of side 1*mm*, 2*mm*, 3*mm*, and 4*mm;* it is observed that the results determined with equation (4.20) presents a satisfactory agreement with finite element results, as demonstrated by the low relative errors listed in Table 4.1. These indicate that there are small deviations between the analytical and numerical solutions. Nevertheless, it is noted that the analytical solution approximates the stresses better beyond the effects of the residual stress, which means that the results correlated better when elasticity is more effective in the bulging process; this is highlighted in the film $1\times1mm^2$. The explanation is the nature of the equation since, for small deflections (residual stress is effective), the displacement field (Eq. 4.1) does not satisfy the high curvatures. Holzer et al. (2017b) described how the two parts (residuals stress and elasticity) contribute to the load-deflection process.

In general terms, it is denoted that all approximations are consistent, as was verified for different square film sizes. Neggers et al (2012a) explained that in the rectangular film ($b/a >= 4$), the bulge equations are not valid at the beginning of the bulging since the cylindricity is not satisfied in that regime and the accuracy of curvatures limits the validity of the approximations.

Table 4.1. Relative errors for each size of thin film

Size [mm^2]	Error [%]	SD [%]
1×1	2.33	0.55
2×2	1.35	1.28
3×3	1.09	1.16
4×4	0.97	1.00

The results suggest that the correlation in the active region of the residual stress can be improved with an auxiliary function designed to minimize the differences of the beginning. Finally, the reported results in this section show that the proposed stress model follows the maximum principal stress determined by FEM, which verifies that there is a numerical agreement between obtained solutions for elastic square thin films.

4.6 Elastoplastic description of square thin films using stress-strain models

Several methods to describe the elastoplastic parameters of rectangular thin films have been recognized and adopted in different studies of bulge testing (Neggers, 2012b; Min et al., 2017). On the other hand, the elastoplastic characterization from load-deflection experimental data is not well

known in square thin films. For this reason, the methodology described in section 4.3 is applied to contribute to the modeling of stress and strain in the plastic regime.

Finite element models are assumed as numerical experiments to provide the load-deflection data with known material models listed in Table 4.1. This process is carried out to validate the developed equations (4.20), (4.22), (4.27) and (4.28). The finite element simulations were performed for two material models (bilinear and nonlinear) considering these as isotropic hardening elastoplastic models. The variables listed in Table 4.2 are mentioned in the above sections, except $\tan(\alpha)$ that corresponds with the slope of the stress-strain curve after the yield limit.

Table 4.2. Material models

Material model	σ_r [*MPa*]	E [*GPa*]	ν	σ_{yp} [*MPa*]	$\tan(\alpha)$ [*GPa*]	Size [mm^2]
Bilinear	166	236.30	0.3	90	23.6	2×2
Nonlinear	60	258.80	0.3	130	See Fig. 4.10b	2×2

Figure 4.9a illustrates a comparison between the numerical and analytical results determined for the strains, in the case of FEA, these are Equivalent total strains (Von Mises).

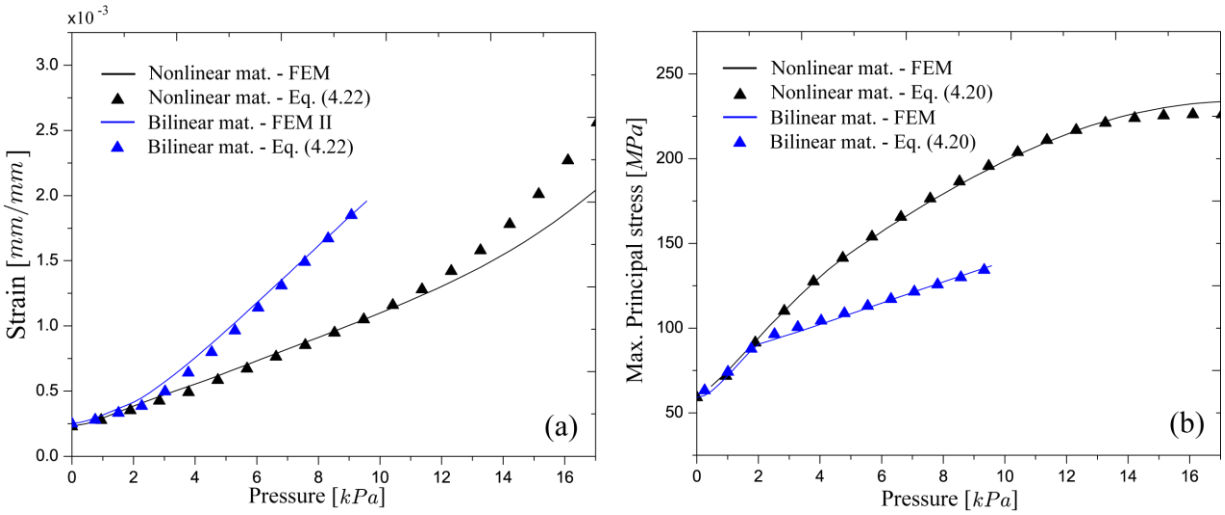

Figure 4.9. Comparison between FEM results and analytical models. (a) Equivalent total strains at the central point. (b) Maximum principal stress at the central point.

Using the load-deflection data of both numerical models (bilinear and nonlinear), equation (4.22) is evaluated. The mean relative deviations presented in the calculations are 5.8% for the bilinear and 4% for the nonlinear (until pressure of 11 kPa). The percentual difference increases considerably above 11 kPa pressure in the nonlinear correlation. This can be caused by the localized plasticization that changes the bulged surface to an irregular shape that cannot be reproduced by the curvatures calculated with equation (4.1). Neggers et al. (2012b) discuss that strains present higher inaccuracies by the error induced in the deflection field that not satisfies the bulged surface

The maximum principal stresses also were calculated as shown in Figure 4.9b. It indicates that the tensions present better approximations to the finite element solutions since the relative errors were 4.7% and 1.5% for bilinear and nonlinear material models. Similar to the strains, the stress deviation presents an inflection in the pressure of 11*kPa*. The results indicate that the stresses can be estimated without performing additional numerical calculations (FEA) since only load-deflection data and the film geometry are enough to determine the state stresses, as demonstrated in Figure 4.8b. It is concluded that the analytical Equation (4.20) and (4.22) converged in a good agreement with the numerical results obtained by FEM.

Equations (4.20) and (4.28) were proposed to predict the material models in the plastic regime from load-deflection data. The first step is to determine the elastic limits with the relation shown in Equation (4.26). According to the proposed methodology, P/w and w^2 keep a linear correlation in the elastic regime which means that there is no plasticization in the bulged surface. The interpolation of the linear function Y_l is built from the first data (initial part of the load-deflection curve), and its domain is extrapolated until the total value of applied pressure. The data set Y_{Nl} corresponds to the load-deflection data mapped overall domain Y_l. These functions are related through the absolute value of relative error $e_Y = (Y_{Nl} - Y_l)/Y_{Nl}$ to estimate the deviations in each pressure state.

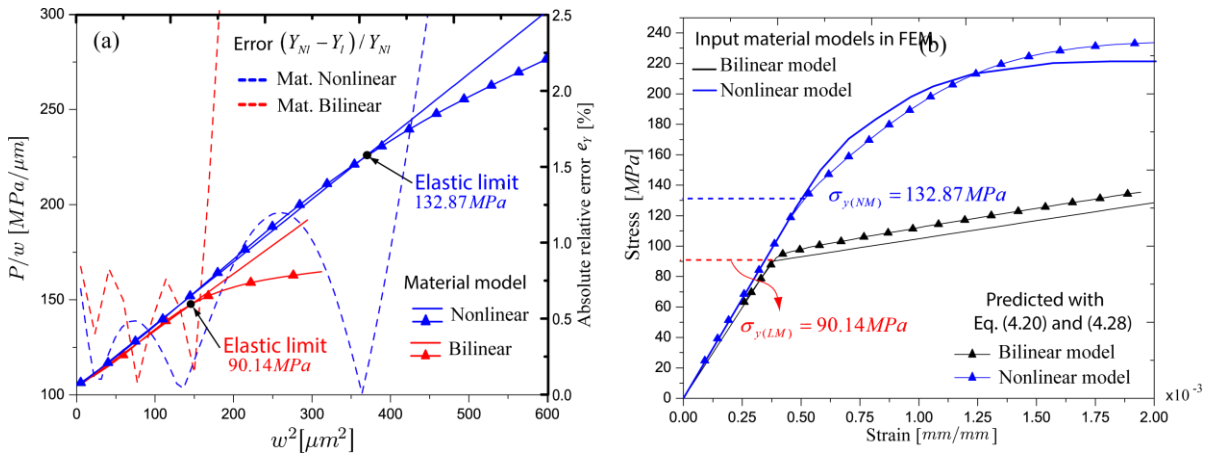

Figure 4.10. (a) Correlations between P/w and w^2; and relative errors between Y_l and Y_{Nl} (dashed lines). (b) Predicted material models.

In Figure 4.10a is observed that relative errors (right axis) present repeated minimum values close to zero, and the last one establishes a starting point in which the error increases indefinitely. This point is considered as the limit point since the last intersection among the linear and nonlinear functions is delimited visibly. The elastic limits determined for the bilinear material model is computed as 90.14*MPa* (initial yield stress *90* MPa) and 132.87 MPa (initial yield stress 130 MPa) for the nonlinear material model as shown in Figure 4.10b (left axis). Equations (4.20) and (4.28) were used to predict the material models calculated and represented in Figure 4.10b. There is observed that the approximation follows the trend of the material models assumed in the proposed finite element experiments. In practical terms, it means that with load-deflection data, stress-strain models can be predicted. We concluded that the methodology presented can be used to characterize the plastic regime after the yield point to study the plastic effects in bulged thin films.

Chapter 5. Fracture toughness evaluation of a cracked Au thin film and plasticity assessment of an Al thin film by bulge testing

This chapter is divided into two main sections that correspond with the applications related to fracture toughness determination and plasticity estimations in thin films under bulging test, two different materials are used as study cases. First, a finite element analysis of a pre-cracked gold thin film was subjected to a bulge test. These tests were conducted in order to determine the elastoplastic properties and fracture toughness of the gold films. For the numerical fracture analysis, the problem was divided into stages; the first stage was the development of the numerical model on the whole film without pre-crack (elasto-plastic analysis) and the second one was performed on a film portion that included the pre-crack (sub-modeling stage). To calculate the stress intensity factor around the crack tip, three different notches (rounded, sharp, and V-sharp) were used. In addition, an improved method for determining the yield stress and residual stress in a freestanding thin aluminum (Al) film is presented based on the results of the bulging test. The film was cyclically loaded with increasing maximum gas pressure. The method to determine plasticity parameters relies on the load-deflection relationship that presents a linear behavior in the elastic regime when scaled with the displacement parameter.

5.1 Experimental setup for a bulge testing of Au (Gold) and Al (Aluminum) thin films

The experimental setup for Al thin film tests was custom-built at the Institute of Scientific Instruments of Czech Academy of Sciences (see Figure 5.1). It comprises a Twyman-Green laser interferometer with a wide collimated beam, pressure transmitter, pressure pump, and digital camera. The interferometer equipment uses a fiber-coupled HeNe laser with a wavelength of 633 nm. The laser beam is split into a measuring beam that reflects off the specimen surface and a reference beam that reflects off a reference mirror (surface flatness of λ/10).

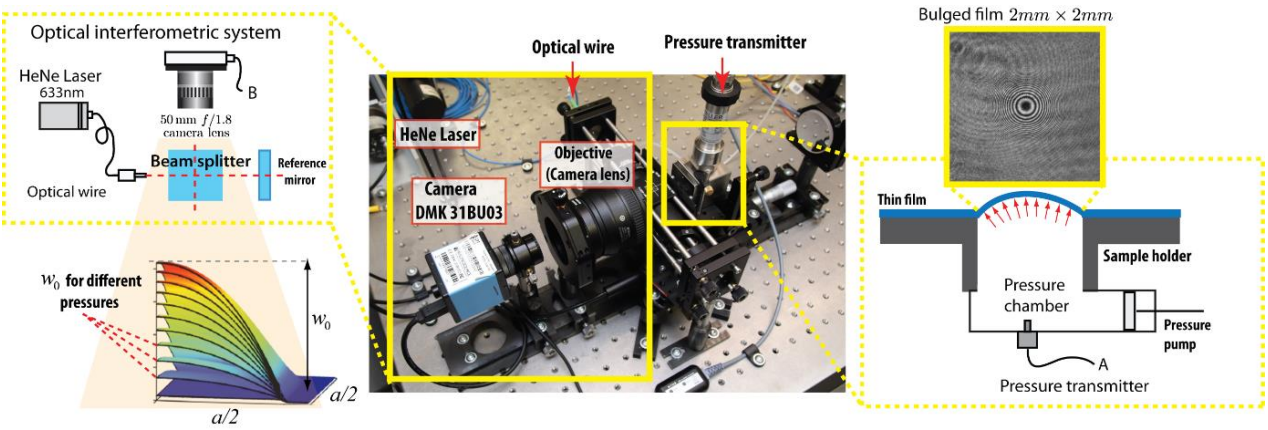

Figure 5.1. Experimental setup for the bulging test of the Al thin film.

The measuring beam interferes with the reference beam at the interferometer output and forms interference fringes projected onto the sensor via camera lens (Nikon 50mm f/1.4 Nikkor G). The test specimen was prepared following the procedure by Vlassak and Nix (1992). A layer of amorphous silicon nitride layer with stoichiometry close to Si_3N_4 and thickness of 525 nm was deposited by low-pressure chemical vapor deposition on Si monocrystalline wafer. A square window of 2 x 2 mm was opened in the Si wafer by wet anisotropic etching. The exact dimension of the window covered by the nitride membrane was 2.02 x 2.03 mm. An aluminum film with a thickness of 1.74 µm was deposited by magnetron sputtering on the nitride (deposition was done for 141 minutes at 500 W at magnetron in an oscillating regime with argon pressure of 0.38 Pa). Finally, the Si_3N_4 layer was etched out, so only the freestanding Al membrane was subjected to the bulge experiments.

For the gold (Au) preparation thin film, the substrates were acquired from Silson Ltd. Southam, UK) which are silicon-rich silicon nitride (SiNx) manufactured by low-pressure chemical vapor deposition (LPCVD). The details of the experimental setup are described in the doctoral thesis of Preiß et al. (2017).

5.2 Stress intensity factor K_I and J-integral

In linear-elastic materials, the stress singularities at crack tips or slit tips can also be explained by stress intensity factors (SIFs). This concept can be observed in corner notches (e.g. V-notch, stepped bar, weld toe notches). In the crack tip, it is observed asymptotic stress decreases from the singularity and it is can be described by the inverse square root of the radial distance r from the crack tip (Irwin, 1968). Stress intensity factors can be used to describe the stress fields near corner notches and crack tips.

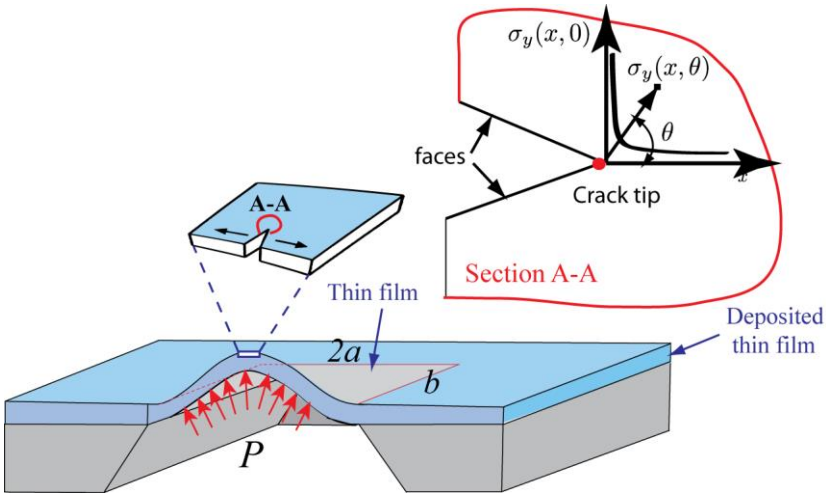

Figure 5.2. Bulge test on a cracked thin film (half model).

There are three modes of notch loading: in-plane tensile loading, in-plane shear loading, and out-of-plane shear loading. Let's consider a bulged film with a pre-crack over the place with the maximum displacement as illustrated in Figure 5.2. The stress field $\sigma_y(r,\theta)$ in the vicinity of an sharp crack tip is described mathematically for the first mode by the following expression Irwin (1968).

$$\sigma_y(x,\theta) = \frac{K_I}{\sqrt{2\pi x}}\cos\left(\frac{\theta}{2}\right)\left(1-\sin\left(\frac{\theta}{2}\right)\sin\left(\frac{3\theta}{2}\right)\right), \tag{5.1}$$

where K_I is the stress intensity factor (SIF), θ and x are the direction and position of the stress field $\sigma_y(x,\theta)$. In the crack tip ($x=0$), K_I can be estimated in a sharp notch as $K_I(x)=\sigma_y(x,0)\sqrt{2\pi x}$. The above expression shows that stress values should be known to compute K_I. There are several methods for computing $K_I(x)$ and one of these is called the direct method. For this purpose different techniques have been proposed as discussed in Qian et al. (2016). This method is based on finite element solutions obtained for $\sigma_y(x,\theta), \forall x \in (x_1, x_2)$. The idea is to choose an interval (x_1, x_2) where stress values are used to compute K_I. Figure 5.3a describes the stress behavior obtained by FEM. The cut domain defined in $(0, x_1)$ is an uncertainty domain because stress values are not defined properly by the numerical singularity that represents the crack front. To calculate K_I in $x=0$, an extrapolation is proposed to project the value of K_I using stress values obtained by finite element solutions as shown in Figure 5.3b.

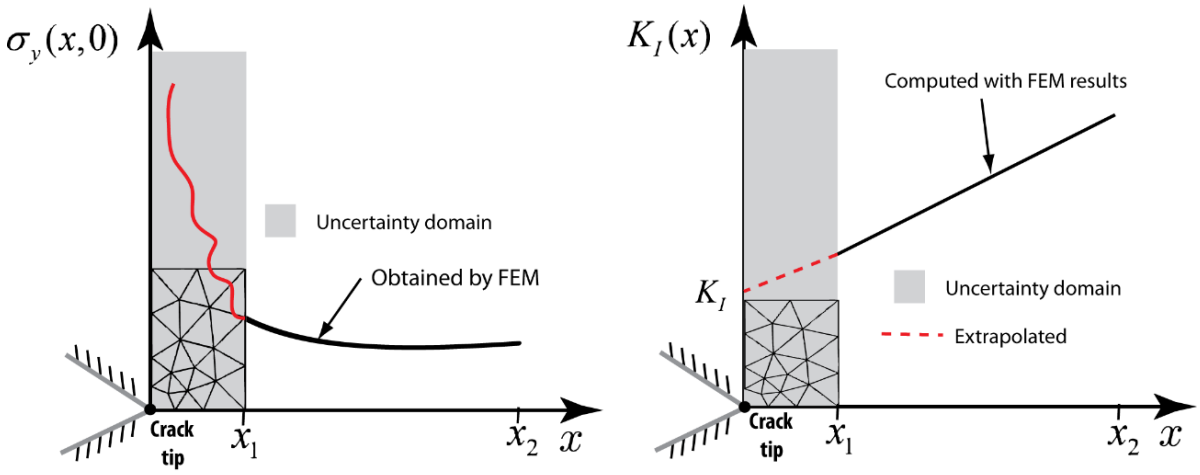

Figure 5.3. (a) Uncertainty of the stresses at the crack tip determined by FEM. (b) Direct method for determining K_I through finite element solutions.

However, the direct method is very sensitive in the vicinity of the crack tip since there is a dependence with the meshing as well as with the shape of the crack root. Therefore, in this study elastic part of J - integral was used. J-integral value is determined by the strain energy release rate close to the crack tip. The J-integral is a fracture parameter that denotes the release rate of the potential energy-related with crack growth. J - integral theory was proposed by Rice (1968), the theory describes the mechanical strength around a crack tip which is defined in a two-dimensional problem by the following expression

$$J = \int_\Gamma \left[W\left(\varepsilon_{ij}\right)dy - T_i\left(\frac{\partial u_i}{\partial x}\right)\right]ds. \tag{5.2}$$

where $W\left(\varepsilon_{ij}\right)$ is strain energy density, T_i are the components of the traction vector over a part of the space delimited by $x-y$, u_i are the components of the displacement vector and s is the distance along any contour Γ traversed in counter-clockwise direction from the lower face of the crack tip. In the

linear elastic plane stress case, J - integral is determined by the strain energy release rate close to the crack tip, being the relationship between K_I (stress intensity factor) and J in the following way (Nuismer, 1975)

$$J = K_I^2 E. \tag{5.3}$$

Where E is the Young's modulus. For plane strain conditions, $J = K_I^2 E / (1 - v^2)$.

5.3 Fracture analysis for a pre-cracked and non-cracked Au thin film

In Figure 5.4, a brief scheme of a numerical approach proposed to simulate a bulged film with a pre-crack that passes through the thickness is described. The approach is based on two solution stages; the first stage is developed on a film without crack and the second one on a film portion that includes the pre-crack (sub-model). A geometric division of the membrane is carried out with the aim to control the meshing parameters around the crack.

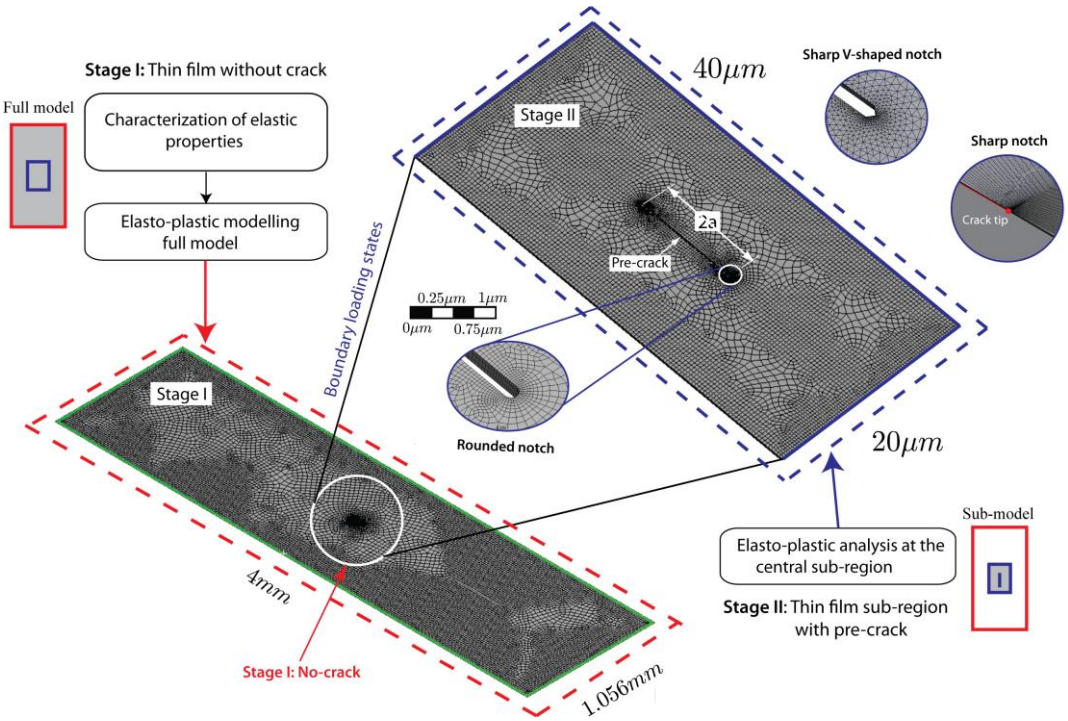

Figure 5.4. Scheme of the solution process by finite element analysis

The film is divided into two geometric sections that are composed by a scaled section (sub-region of 1% of the size film – sub-model) located in the center of the film and the second one part is the complement of it, as illustrated in Figure 5.4. It is very important to point out that the sub-section contains the crack, further, three notch types are considered for the fracture analysis; rounded, V-sharp and sharp.

In the solution stage I, the model without pre-crack is used to characterize the elasto-plastic properties with the aim to approximate the load-deflection curve measured experimentally. For the stage II, the

loading states (those obtained in the stage I) are applied at the boundaries of the sub-region that includes the pre-crack. It means that only the solution for the chosen subregion will be computed. The sub-modelling process has the advantage of reducing computations in the entire geometry. In addition, the fracture problem can be classified as a multi-scale problem because the finite element solution can be weighed computationally. Only if it is solved in one stage. This problem occurs when the mesh should satisfy multiple dimensional scales in the same problem, such as micro- to milli-scale. In both cases, the sub-modeling is based on Saint-Venant's principle which guarantees the same load state in the boundaries of the sub-regions. The technique has been used in several studies (Norman et al., 2011; Narvydas & Puodziuniene, 2014; Bozkurt et al., 2016; Zhao et al., 2019). For the analysis, a gold thin film is considered since experimental data of bulge tests were available for this purpose (Preiß et al, 2017). In Figure 5.4, the overall views of both finite element models are shown, the whole model (stage I) and sub-region (stage II). The size of the thin film is 1.056x4 *mm* with 198.6 *nm* of thickness. A crack of 10 μm in length and 100*nm* in width is included in the sub-model (sub-region) with dimensions of 20x40 μm as the figure describes it.

5.4 Nonlinear fracture results for the Au thin film

With the elastic properties determined in the chapter 3 for the Gold (Au) membrane, the estimation of elasto-plastic behaviour is achieved from the calculations of stresses and strains proposed by Vlassak & Nix (1992) for long rectangular membranes (see Chapter 4). The stresses were computed in the central part at *x*-direction as indicated in Figure 3.10b.

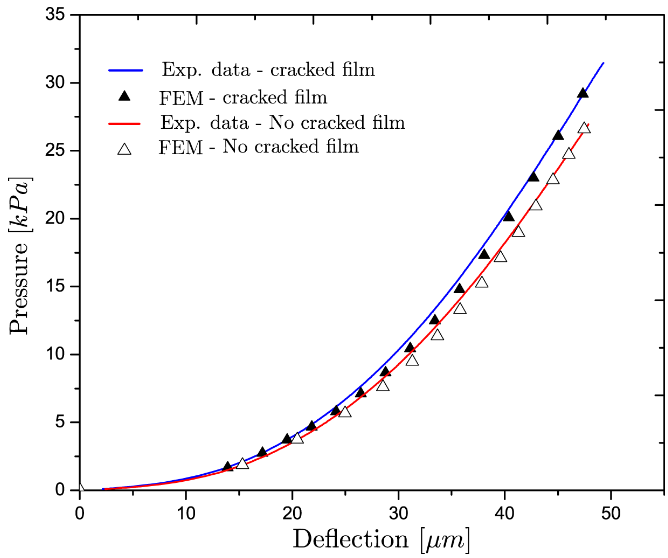

Figure 5.5. Comparisons in load-deflection curves for non-cracked and cracked film with the experimental data

Using all mechanical properties determined in the section 3 and applying the proposed methodology described in section 5.3, there were computed the deflections for the films without crack (full model) and with the pre-crack, the obtained results are shown in Figure 5.5. The simulation procedures for the film without crack are described in the chapters 2 and 3, these included the characterization process of the elastic properties determined in chapter 3, section 3.5. It is seen that the load-deflection curve agrees with the experimental data. Although there are some differences between the displacement intervals 30 *um* and 45 *um*, the correlation is acceptable for this purpose because despite all nonlinear effects at that load level the correlation presented good accuracy. The

experimental details of obtaining load-deflection curves of a cracked film are described in Preiß et al. (2017). Figure 5.5 shows that damage pressure was determined at 31.46 kPa, which corresponds to a broken film.

It is noted in Figure 5.5 that there are some differences between the simulations and the experimental data. It is primarily identified that the stiffness in the film is higher when there is a presence of the pre-crack and therefore, the displacements are lower, it is primarily identified that the stiffness is higher when there is a crack on the membrane. Both experiments were approximated with the same material model, it indicates that the numerical computations likely approximated both bulging tests. Additionally, in the stage II, fracture parameters were computed with ANSYS 16.1 which supplies the maximum and the minimum values of the K_I and J distributions along the crack front, the results are illustrated in figures 5.5 and 5.6. In Figure 5.6a is illustrated K_I along crack front in the pressure level of $27kPa$, the point A indicates that the crack tip on the top surface (no pressure), B point is located with the minimum value of K_I and C is the crack tip on the bottom surface subjected to different pressure levels. According to the distribution of K_I, it seen that the fracture mechanism is not symmetric through the thickness, which means that the crack probably can be propagated from the top surface firstly.

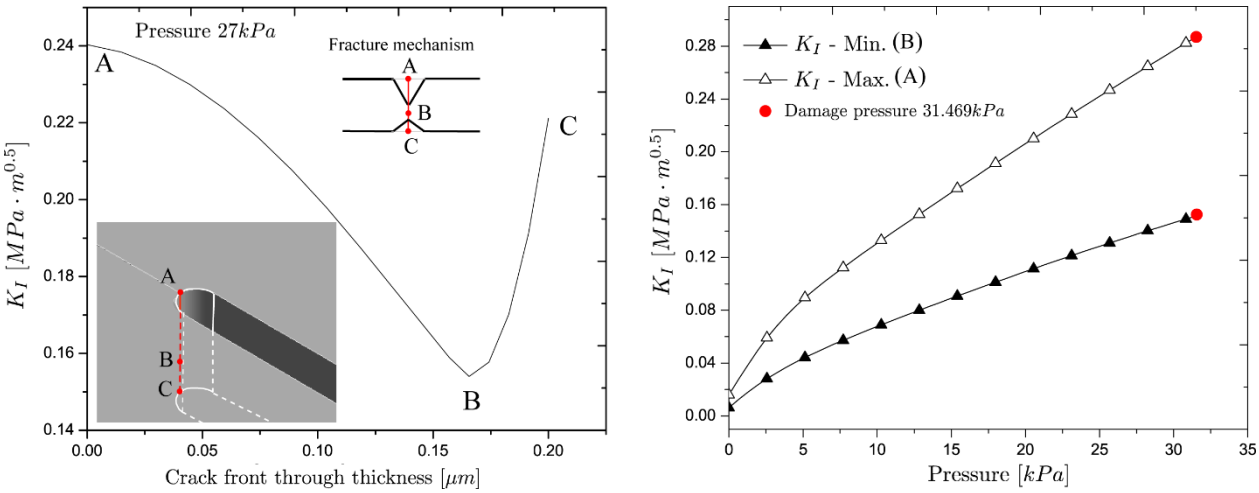

Figure 5.6. (a) Stress intensity factor through thickness obtained by ANSYS. (**b)** Stress intensity factor vs loading pressure.

Figure 5.6b shows all K_I values respect to the increment of pressure levels until that the film was broken, the last value will be taken as the fracture toughness of the gold film knowing that the damage pressure was 31.469 *kPa.* Results shows that the maximum value reached was $0.28MPa \cdot m^{0.5}$ and the minimum $0.15MPa \cdot m^{0.5}$ for the ultimate pressure. The values determined for K_I agree with those reported by Hosokawa et al. (2008) determining $0.45MPa \cdot m^{0.5}$ for gold films. Recently, Preiß et al. (2017) determined values corresponding to $2MPa \cdot m^{0.5}$ for gold film with thickness between 60 nm and 320 nm. Fracture toughness values show that the thin films generally present lower values than those determined for bulk samples as has been reported for different metal films (Wang et al., 2003; Hosokawa et al, 2008; Hirakata et al., 2011).

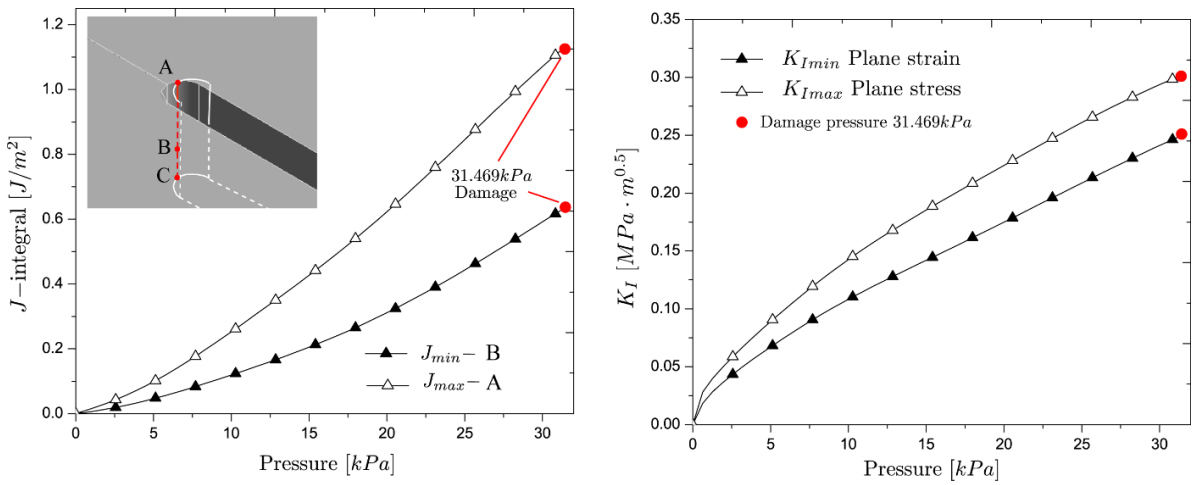

Figure 5.7. Sequential procedure for estimating Young's modulus and Poisson's ratio.

In Figure 5.7a, values of *J* -integral were computed to approximate fracture toughness from energy release rate relation exposed in Equation (5.3). There are highlighted the maximum and minimum values obtained for *J*, 0.62 and 1.13 J/m^2.

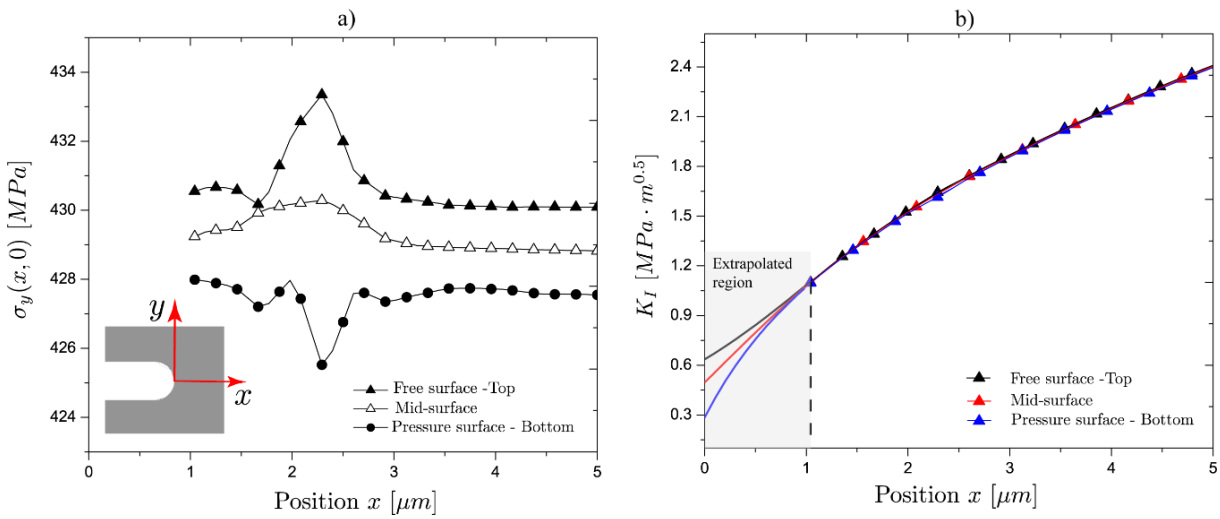

Figure 5.8. (a) Stress in *y* direction close to the crack tip for 31.469 *kPa* . (b) Estimation of K_I values from Equation (5) for 31.469 *kPa*.

Applying Equation (5.3), K_I values were calculated and these are depicted in Figure 5.8b. K_{Imin} was determined for plane strain condition and K_{Imax} for plane stress. Obtained limit values of toughness were 0.3 (K_{Imax}) and 0.25 (K_{Imin}) $MPa \cdot m^{0.5}$, these correspond with those reported in Figure 5.8b. As an additional methodology of comparison, the fracture toughness can also be obtained from stress values in *y* – direction, those close to the crack tip, as detailed in section 5.2. Figure 5.8a shows the stress values determined from 1 *um* until 5 *um* of the crack tip, since the closest values do not have numerical meaning by the uncertainty induced in the crack tip. Along the crack, stress values are between 425 and 433 *Mpa,* with a maximum stress located on the top surface at 2 *um.* Using stress values in equation (5.3), K_I values were extrapolated until the crack tip to determine the fracture

toughness. The values are $0.63 MPa \cdot m^{0.5}$ and $0.39 MPa \cdot m^{0.5}$. Figure 5.9 collects the K_I values determined by the three exposed methods.

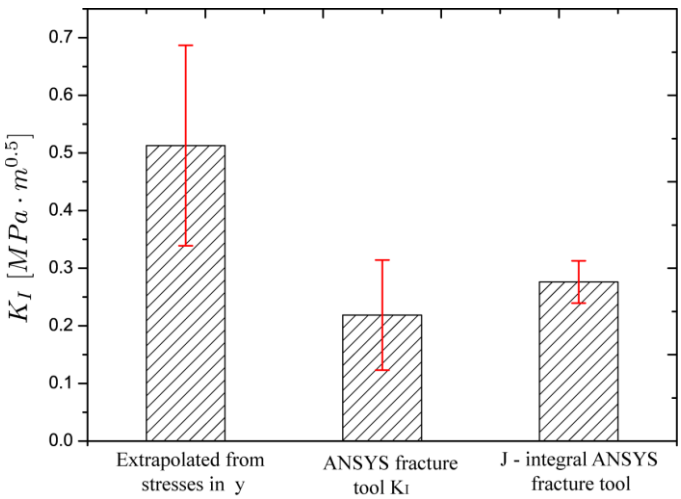

Figure 5.9. K_I values from different methods.

As final Analysis, Figure 5.10 is computed for three different notches at the crack-tip as illustrated in Figure 5.3. Figure 5.10 shows the values calculated for the fracture toughness with *J*-integral and Equation (5.3). The mean values were determined between 0.288 and 0.303 $MPa \cdot m^{0.5}$ from elastic (1.03 J/m^2) and elasto-plastic (1.136 J/m^2) *J*-integrals.

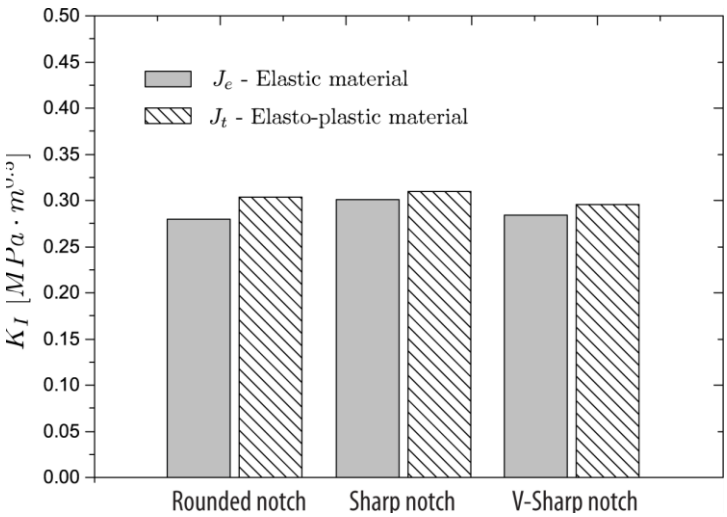

Figure 5.10. K_I values from different notches for both J- integral fracture methodology.

These results agree with the values reported by Hosokawa et al. (2008) that determined $0.45 MPa \cdot m^{0.5}$ for gold thin films with thicknesses between 200 and 300 *nm.* It is observed that the plasticity effects have influence at the crack-tip since *J*-integral values obtained from elastic problem were very close to those computed with plasticity.

5.5 Plasticity analysis for an Al thin film

In this section is applied an improved method to determine the yield stress and residual stress in a freestanding aluminum thin film by analysing experimental data obtained from the bulging test. The specimen was glued to a stainless-steel plate with a hole in the centre and mounted to the chamber via four screws. A computer-controlled industrial-grade piston operated by a syringe pump was used to increase and decrease the chamber pressure and on the membrane. The chamber pressure was monitored by a pressure transmitter with a precision of 60 Pa as described in section 5.1. The method to determine the plasticity parameters is based on the load-deflection relation that presents a linear behaviour in the elastic regime when it is scaled with the displacement parameter as discussed in Chapter 4

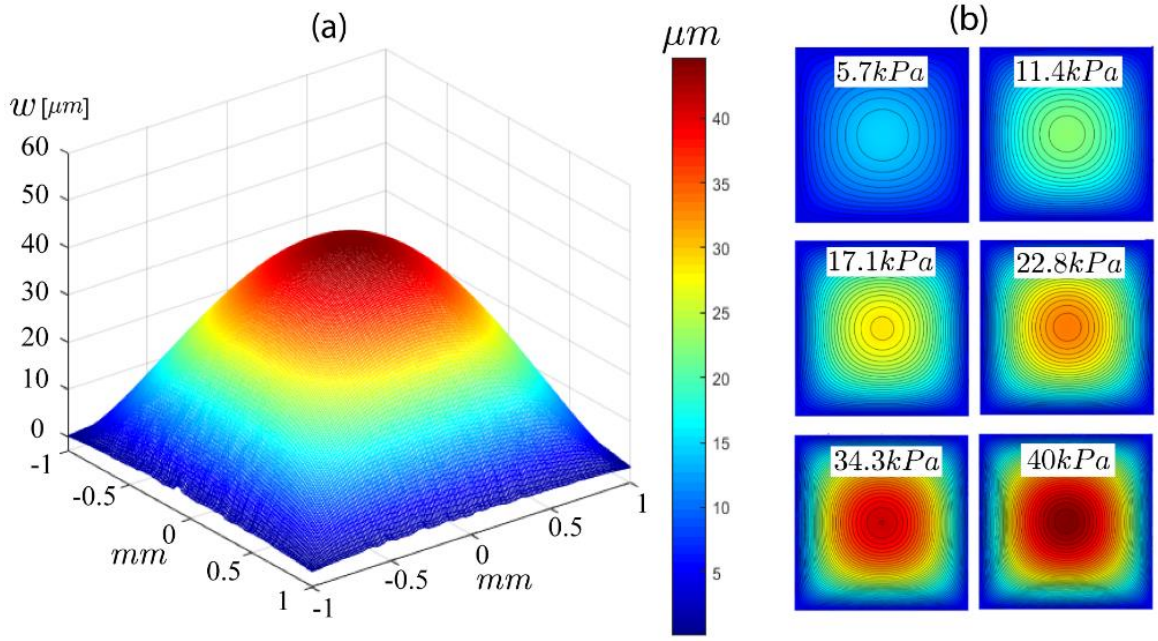

Figure 5.11. (a) Example of 3D experimental displacement field, (b) Displacement fields for different pressure states.

From the measured data, it is possible to calculate the displacement of every pixel in the normal direction to the specimen surface in relation to the pressure change, as illustrated in Figure 5.11. Further, the reconstruction of the shape of the whole membrane w(x,y) as a pressure function was computed, including the central point of the membrane as shown in the same figure. It is important to note that measurements of displacements close to the fixed boundary of the membrane are not very feasible since the camera is unable to capture this part of the film when it is bulged.

For the bulging test, an aluminum film with a thickness of 1.74 µm and size of 2×2 mm was cycled six times in loading and unloading conditions, respectively. Each loading cycle incremented the gas pressure progressively by 10 kPa, starting at a maximum pressure of 10 kPa in the first cycle, and finalizing of 60 kPa, for the last cycle. The schematics of the loading conditions are given in Figure 5.12a; the measured displacement of the central point versus gas pressure is plotted Figure 5.12b.

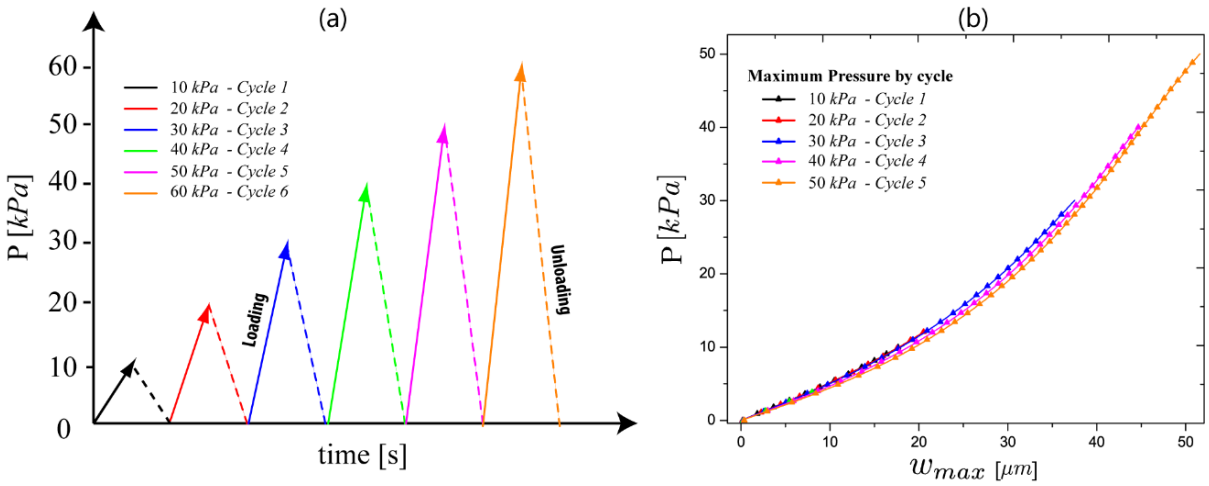

Figure 5.12 (a) The schematics of the membrane loading in six cycles; (b) pressure – deflection curves as the central point.

Figure 5.13a shows the measured data correlating the pressure and stress values at the membrane centre σ_{xx0} for the first four measured loading cycles. The stresses were computed with Equation (4.20). For the gas pressure close to zero, an initial value of stress corresponds to the residual stress σ_r, as illustrated in the magnified section A-A. The residual stress is not changing for the first three cycles; these values were used for calculation of σ_r in as-received Al film as 82.5 ± 0.2 MPa. It is also visible that residual stress is changing after subsequent cycling due to the plasticity effects.

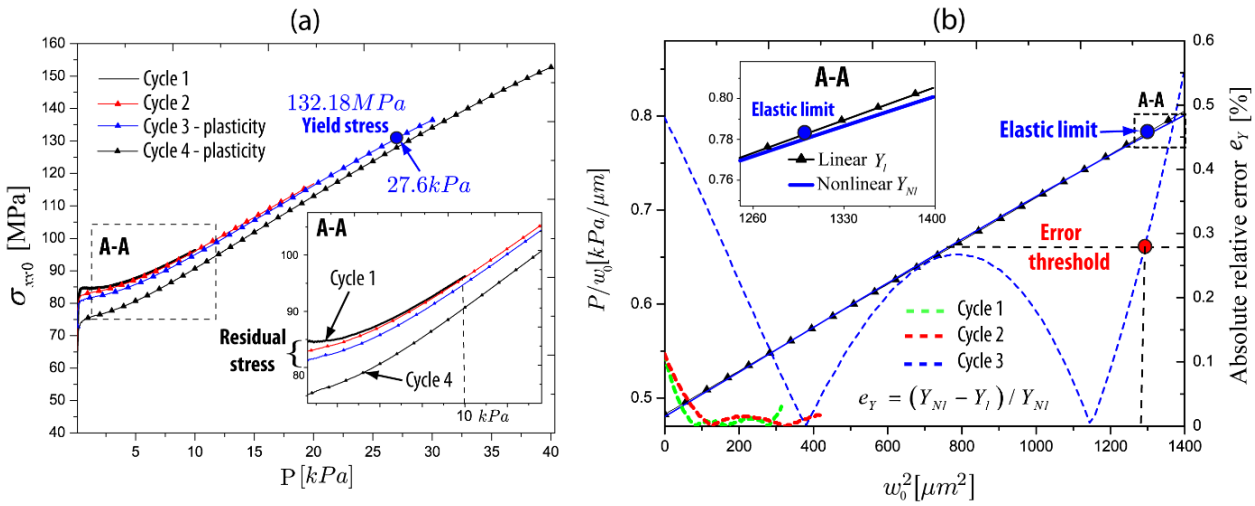

Figure 5.13. (a) Pressure-stress curve for different loading cycles. (b) Scaled load-deflection relations and relative error for the third loading cycle.

The value of σ_r was compared with values calculated from Equation (1.4) and constants C_1 listed in Table 5.1, following the procedures described in Chapter 3. Table 5.1 demonstrates that σ_r is in good agreement with the values calculated by classical models determined with Equation (1.4). The difference between the value found by other authors and this study ranges between 0.43% and 10% for the oldest approximation of C_1. Based on the above results, we consider it an advantage that residual stress can be determined without complicated calculations of C_1. In addition, the validity of Equation (4.20) developed in chapter 4 is successfully established.

Table 5.1. Residual stress computations with known C_1 values

C_1	σ_r [MPa]	**Error [%]**	**reference**
3.044	91.56	10.98	Tabata et al. (1989)
3.41	81.73	0.93	Pan et al. (1990)
3.393	82.14	0.43	Vlassak et al. (1992)
3.45	80.79	2	Maier-Schneider et al. (1995)
3.42	81.49	1.22	Bonnotte et al. (1997)
---	82.5 ±0.2	---	Present study

In Figure 5.14a, the residual stress value showed a change after the third loading cycle with a maximum pressure of 30 kPa, suggesting the membrane had irreversibly deformed. Equation (1.6) was used to determine whether plastic effects occurred during this loading cycle. $X\ [w_0^2]$ and $Y\ [P/w_0]$ were fitted by a linear elastic function (Y_l) and smoothed by a cubic polynomial function (Y_{Nl}). Both functions Y_{Nl} and Y_l are plotted in Figure 5.14b.

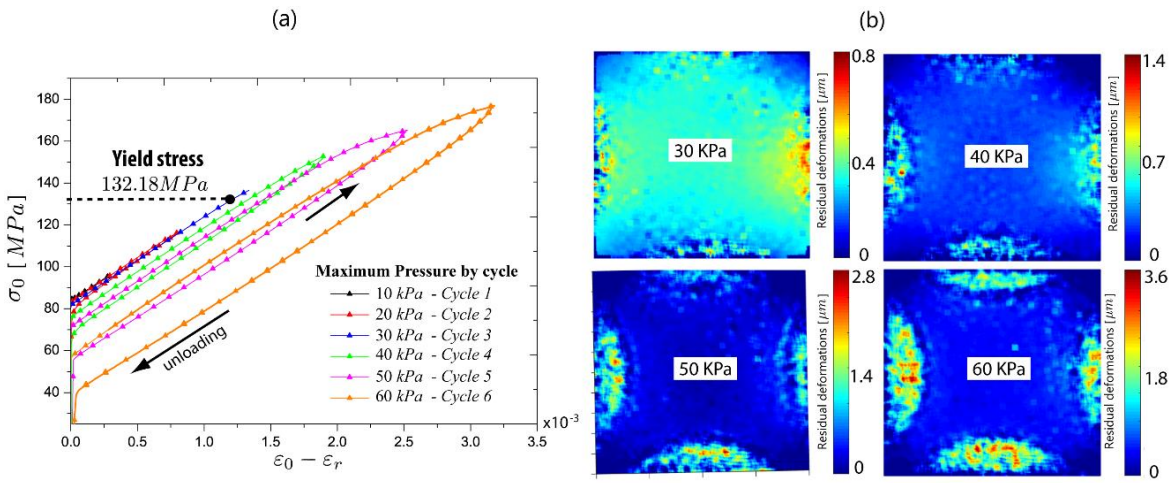

Figure 5.14. (a) Stress and strain curve for different loading cycles. (b) Residual deformations after unloading cycles.

It was calculated the relative error function e_y to determine when the linear relationship no longer followed experimental data. Comparing the results, the following criteria was chosen to define the threshold error: if the final error reaches a value higher than the errors computed through the domain, the error limit is defined on the last error peak, as shown in Figure 5.14b. The final errors on the domain do not overpass the higher errors in the first two loading cycles. In the third cycle, all the conditions are met, and an error limit of 0.27% percent has been established. This corresponds with $X = 1280\mu m^2$ which is related to the pressure $27.6kPa$, and the stress calculated is $132.18\ \text{MPa}$. This value represents the yield stress determined for the equi-biaxial stress state at the central point.

Figure 5.14a shows stress-strain curves for the six loading cycles; the strains are relative measurements, excluding the residual strain calculated according to Equation (4,21). It is noted that from the fourth cycle, the stress-strain curves start to shift down from the value of residual stress of the as-received film, and the difference of residual stress at zero strain between loading and unloading values augments. It indicates that when the plastic deformations are introduced, and the hysteresis

increased in the stress-strain curve. This effect has been reported e.g. by Kalkman et al. (1999). It means that the residual stress diminishes with each cycle showing a stress relaxation effect. In general terms, we can observe that the plasticity effects after the third cycle influenced the mechanical behavior in each bulging stage that was detected with the presented methodology. The effects caused by the plastic deformation could be explained from a microstructural analysis since it is well known that the yield strength of thin films can be affected by more mechanisms operating in the microstructure as changes in the dislocation density or (sub) grain size. Figure 5.14b illustrates how the plastic effects are visualized on the measured displacement field after the film bulged. In this case, the last four loading cycles were considered for the analysis, from 30 kPa until 60 kPa. It is observed that the film remains deflected in a non-uniform way, which shows the higher residual displacements at edges. Progressively, the residual deflections increase their values from $0.8\mu m$ to $3.6\mu m$. Usually, in plates subjected to a transversal loading pressure, the stresses are higher in the boundaries when these are in clamped conditions. Lin et al. (2014) discussed that the local curvatures induced restriction of the bending moments developed at the boundaries. As a consequence, stresses are higher at these locations.

Chapter 6. Elastic properties characterization of bilayer thin films subjected to bulge testing

This chapter describes a methodology to characterize the elastic properties of a thin film deposited over a substrate (Bilayer configuration) with known elastic properties, as a study case, a silicon nitrate film Si_3N_4 (studied in previous chapters) is used as the main substrate. When a second film is deposited on a primary film, the first effect produced by adding it is the modification of the residual stresses in both films. It is important to point out that in monolayer films, the classical load deflection equation is useful to compute residual stresses. However, in bilayer films, there are more parameters that depend on each film, therefore this model is not applicable in a simple way.
The main effect of manufacturing a bilayer film is the redistribution of the residual stresses in between layers since the equilibrium conditions on the substrate change when the second layer is added. This challenge is solved by developing a numerical method to estimate both residual stresses using new equilibrium conditions that consider the shear lag effect (Tinoco et al., 2010) between both films. As a result of determining these values, Young's modulus of the second film can be determined with a combination of the methodologies exposed in previous chapters of this thesis.

6.1 Finite element model for bulge testing in bilayer thin films

This section describes the procedure considered to simulate the bulge testing on bilayer thin films utilizing a finite element analysis. As detailed in section 2.1, some processes already explained are implemented in this chapter.

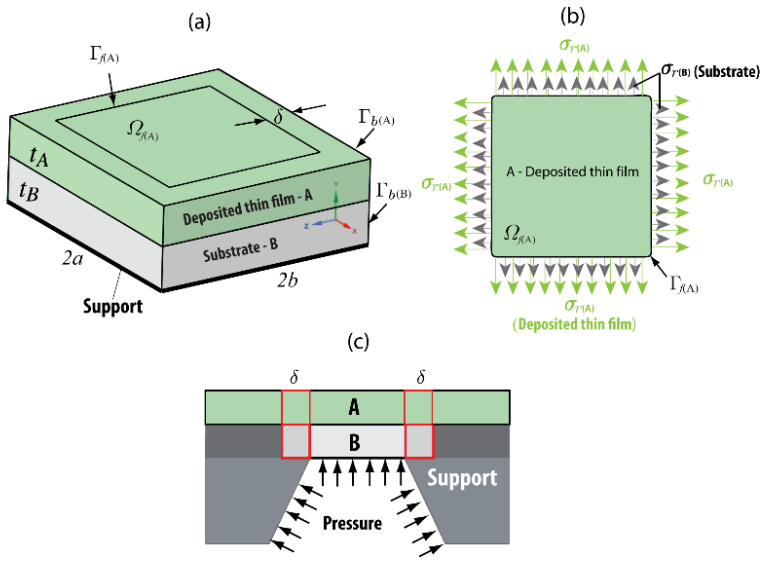

Figure 6.1. (a) Composition of a bilayer thin film. (b) residual stresses in a bilayer thin film. (c) Bulging test scheme in a bilayer thin film.

Figure 6.1a shows two films called A and B, which correspond to a substrate and deposited film. With the fabrication process, residual stresses in each film are generated internally, however, their magnitudes are different but their definition is governed by the equilibrium conditions. It is important

to denote that when the first layer is deposited (monolayer case - first stage of manufacturing), residual stresses are developed on the substrate (Engwall et al., 2016; Chason & Guduru, 2016), but when the second layer is added, these are modified by the new equilibrium conditions. It means that a new residual stress value arises. At the end of the process of manufacturing, both films remain stretched by the individual residual stress, as illustrated in Figure 6.1b. Where $\sigma_{r(A)}$ and $\sigma_{r(B)}$ represent the residual stresses of the deposited thin film and the substrate.

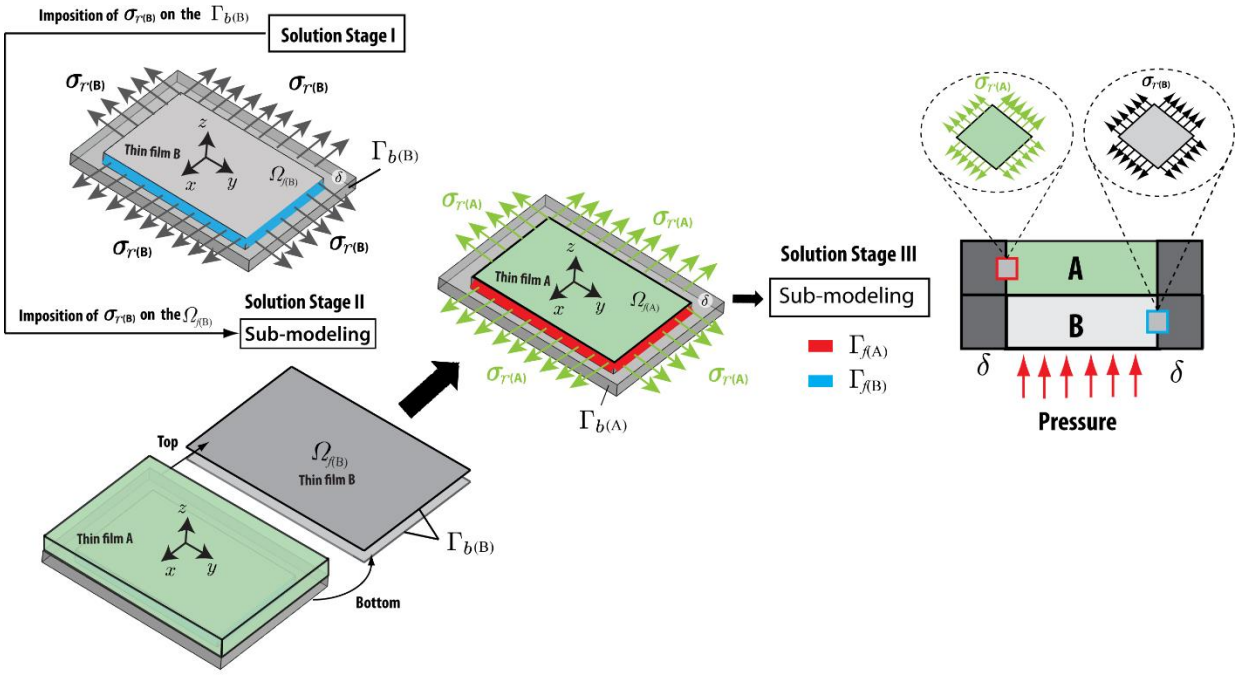

Figure 6.2. Scheme of the solution process by finite element analysis.

To model bilayer thin films subjected to a bulging test (see Figure 6.1c) through finite element analysis, it is necessary to review section 2.1. The first step is the design process of the bilayer geometry. A submodeling strategy is considered for the analysis, which means that the solution is planned in three stages as follows: stage I (residual stress for substrate at the boundary $\Gamma_{f(B)}$), stage II (Importing residual stress for the substrate in the top and bottom domains $\Omega_{f(B)}$), and stage III (pressure conditions application on both stressed films on the $\Gamma_{f(A)}$ and $\Gamma_{f(B)}$). The geometry of each film is defined by an active domain $\Omega_{f(A)}$ (real domain corresponding to the deposited thin film) and $\Omega_{f(B)}$ for the substrate. The active domain is considered the face with higher dimensions. As explained in chapters 2 and 3, a virtual boundary δ (numerical boundary) is considered to emulate the stiffness of a real boundary, a discussion about this parameter is described in sections 2.1 (chapter 2) and 3.3 (chapter 3). For the finite element model, In the solution stage I, it is carried out the modelling of the substrate, in this stage, the imposition of the residual stress $\sigma_{r(B)}$ is applied on the boundary $\Gamma_{f(B)}$. The virtual boundary is neglected in this stage, however, this boundary should be considered in stage III. The main idea to impose only $\sigma_{r(B)}$ is determine the stress distribution over the film. The second modeling is carried out on both films, the resulting stresses inside $\Omega_{f(B)}$ (bottom and top) are imported to determine the residual stresses of the thin film A. This strategy guarantee that it is necessary to know the residual stresses of the substrate since the residual stresses over film A are

determined by the equilibrium conditions on both films. Here, it is important to take into account the determination of the $\sigma_{r(A)}$ value, since this is a constant value over the film, therefore maximum and minimum principal cannot represent this value. This aspect is important since the role of the residual stresses interacts with the shear stresses at the boundary, which means that there is not a principal direction for these values. Therefore, it is important to consider the Coulomb-Mohr criterion (Labuz & Zang, 2012) for the definition of the residual stresses in both films. Then, the residual stress can be obtained from the stress intensity defined as $\sigma_r = 2\tau = (\sigma_1 - \sigma_3)$, or from averaged stress $\sigma_r = (\sigma_1 + \sigma_3)/2$, where σ_1 is the maximum principal stress and σ_3 is the minimum principal stress.

In the last stage, all geometrical characteristics should be considered, including the virtual boundary δ. In this stage, the solutions for $\Gamma_{f(A)}$ and $\Gamma_{f(B)}$ are imported into the new model which includes the stiffness of the virtual boundary, at this point, the pressure *P* is applied on the bottom active surface $\Omega_{f(B)}$ of the substrate. Finite element solutions were obtained with ANSYS 19 on a LENOVO Legion VS30-1 SICH (lntel(R) Core (TM) i7-87 SOH CPU @ 2.20GHz, 2208 Mhz, 6 Core(s)) notebook which ran in Windows 11 environment in order to compute the proposed FEA models. Details of the simulation procedures via finite element analysis can be found in the previous chapters.

6.2 Numerical strategy for determining residual stresses in bilayer thin films

6.2.1 Theoretical background for the numerical strategy

Figure 6.3a shows a structure composed of two thin films (bilayer configuration), of which one represents the substrate (thin film B), and the other the study layer (thin film A). As part of the first manufacturing process of a bilayer thin film, the substrate is deposited on the main support, this first layer is structurally defined by two important mechanical characteristics that define the bulging behavior, the residual stress $\sigma_{r(B)}$, and the elastic properties (E_B, v_B). After deposition, these parameters are considered unknown. The methodology for determining the elastic properties of a monolayer was presented in chapters 3 and 4. However, in this chapter, it is considered the case in which the elastic properties (E_B, v_B) of the first layer are known since these can be determined previously to the addition of a new layer to configure a bilayer thin film. Let's consider that a second layer is deposited over the substrate, in this case, it is assumed that their properties are unknown ($\sigma_{r(A)}, E_A, v_A$). Therefore, a characterization procedure for the following properties should be carried out for all these constants $\sigma_{r(B)}, \sigma_{r(A)}, E_A, v_A$. To understand the interaction of the forces that act in between both films when these are initially stretched by the residual stresses, it is proposed an equilibrium model. If the equilibrium conditions are evaluated in a small section dx located (as illustrated in Figure 6.3a) in any section of both thin films, there is observed that the interaction mechanism will be through the shear stress (bonding boundary). This model is called shear lag which has been applied to study joints (Abedin et al., 2019) and composite material interactions (Landis & McMeeking, 1999). The model neglect normal stresses at the z-direction (normal direction to the bonding surface), which is adequate for mechanical interaction of bilayer thin films before applying pressure for the bulging these. Considering the equilibrium conditions of the substrate B (Figure 6.3b**)** at the *x*-direction it is obtained that

$$\frac{d\sigma_{r(B)}(x)}{dx} = \tau(x)\frac{1}{t_B}, \tag{6.1}$$

Where $\sigma_{r(B)}(x)$ is the residual stress at the x-direction in the thin film B, $\tau(x)$ is the shear stress at the x-direction, and t_B the thickness of the film B. Equation (6.1) was used by Tinoco (2018b) in piezoelectric materials applications. Following the same procedure that (6.1), the equilibrium conditions are determined for the film A, which we have that

$$\frac{d\sigma_{r(A)}(x)}{dx} = -\tau(x)\frac{1}{t_A}. \tag{6.2}$$

The name of the variables is similar to the film B, it means that these are analogous for the film A.

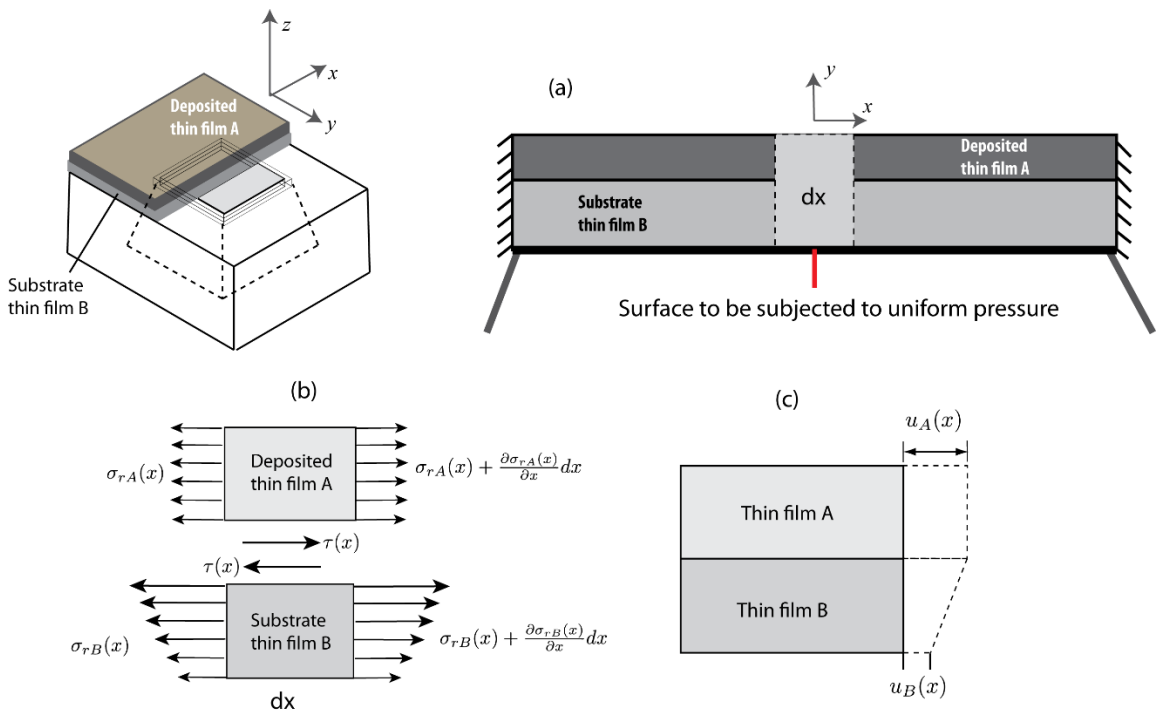

Figure 6.3. (a). Model of a thin film deposited on the substrate. (b) Equilibrium conditions for a differential element of the set are subjected to residual stress. (c) Kinematic conditions are imposed by the residual stresses (compatibility conditions)

Relating Equations (6.1) and (6.2), it is computed the following expression

$$\frac{d\sigma_{rB}(x)}{d\sigma_{rA}(x)} = -\frac{t_A}{t_B}. \tag{6.3}$$

This expression means that the changes in the residual stresses are related directly to the thicknesses relations of the films in equilibrium conditions if the stresses are related through the shear lag effect in the bonding boundary. However, there are several relations that govern the behavior of the multilayer thin films as proposed by the following equation for residual stresses expressed in the book of Schlenoff & Decher (2006), which is computed as

$$\sigma_{r(bi)} = \frac{t_B}{t_{bi}}\sigma_{rB} + \frac{t_A}{t_{bi}}\sigma_{rA}, \tag{6.4}$$

Where $\sigma_{r(bi)}$ is the equivalent residual stress for both films, t_{bi} is the total thickness of the sum of both layers. For the elastic properties, the equation is represented as

$$E_{bi} = \frac{t_B}{t_{bi}}E_B + \frac{t_A}{t_{bi}}E_A, \tag{6.5}$$

For which E_{bi}, E_B, E_A represents Young's modulus of both films (equivalent), the substrate B, and the study thin film A. Considering the parameters described above, the bulging test for a bilayer thin film can be represented in a new load-deflection model as follows (Martins et al., 2008),

$$P = C_{1(bi)}\frac{\sigma_{r(bi)}t_{bi}w_0}{a^2} + C_{2(bi)}(v)\frac{E_{bi}t_{bi}w_0^3}{a^4}, \tag{6.6}$$

Considering that the bilayer thin film is a square or rectangular bilayer thin film, the parameter a represents the length edge (short side) of both thin films. Model presented in (6.6) is commonly used for estimating the composite properties of the residual stress $\sigma_{r(bi)}$ and Young's modulus E_{bi}. However, it is necessary to know more parameters to determine the residual stress of each film. Then, the characterization of the elasticity is more simple since the properties of the substrate are known, but, the residual stresses are not due to the stress redistribution when the new film is added. To solve this challenge, a numerical methodology based on equilibrium conditions (see Eq. (6.3)) and multilayer thin film models (see Eq. (6.3) and (6.6)) is proposed. This with the aim to estimate both residual stresses after a bilayer film is tested via a bulging test. The numerical procedure to compute σ_{rB} and σ_{rA} is applied as follows:

1. First stage is to compute the parameter $C_{1(bi)}$ (see Equation 6.6), for this process a set of finite element models should be prepared with the same geometry and known mechanical parameters for both should be designed. Knowing that $E_{A,k}, E_{B,k}, \sigma_{r(B),k}$, and Poisson's ratios are input parameters. As output parameter, $\sigma_{r(B),k}$ is computed from FEA analysis as methodology is described in section 6.1. $\sigma_{(bi)}$ and $E_{(bi)}$ can be calculated with Equations (6.4) and (6.5). Using Equation (6.6), P and w_0 (obtained numerically), $C_{1(bi)}$ is determined by least square fitting. In this process, $C_{2(bi)}(v)$ is also obtained each numerical example proposed. The final value for $C^*_{1(bi)}$ is the mean value determined with all numerical experiments computed.
2. Second stage is compute $\sigma_{r(bi)}$ for the P and w_0 (obtained experimentally), again applying least square fitting, we can obtain the equivalent residual stresses $\sigma_{r(bi)}$ corresponding to the experimental data.
3. Third stage is to estimate the residual stresses σ_{rB} and σ_{rA}, applying the following algorithm:

   Step 1: Initializing variables $\sigma_{r(bi)} = \alpha$ (determined in stage 2), t_A, t_B, t_{bi} and $\sigma_{rB(0)} = 10$

   Step 2: To estimate $\sigma_{rA(0)}$ with the following equation

$$\sigma_{rA(0)} = \left(\sigma_{r(bi)} - \frac{t_B}{t_{bi}} \sigma_{rB(0)} \right) \Big/ \frac{t_A}{t_{bi}}.$$

Step 3: To estimate $\sigma_{rB(1)} = \dfrac{\sigma^2_{rB(0)}}{\sigma_{rA(0)}}$

Step 4: *Initialize a cycle WHILE until that* $R_j - 1 < 1 \times 10^{-6}$ *is satisfied*

Step 5: *Initialize a cycle while until this expression is satisfied, initialize* $j = 1$,

To calculate a new $\sigma_{rA(j)} = \left(\sigma_{r(bi)} - \frac{t_B}{t_{bi}} \sigma_{rB(j)} \right) \Big/ \frac{t_A}{t_{bi}}.$

To compute $R_j = \left| \left(\dfrac{\sigma_{rB(j)} - \sigma_{rB(0)}}{\sigma_{rA(j)} - \sigma_{rA(0)}} \right) \Big/ \left(\dfrac{\sigma_{rB(j)}}{\sigma_{rA(j)}} \right) \right|$

Step 6: *Compare the following conditions, if* $R_j > 0$, then $\sigma_{rB(j+1)} = 1.005\sigma_{rB(j)}$, else, then $\sigma_{rB(j+1)} = 0.995\sigma_{rB(j)}$

Step 7: *Compare the following conditions, if* $R_j > 0$, then $\sigma_{rB(j+1)} = 1.005\sigma_{rB(j)}$, else, $\sigma_{rB(j+1)} = 0.995\sigma_{rB(j)}$

Step 8: *Compare the following condition, if* $R_j - 1 < 1 \times 10^{-6}$, then break the while cycle

Step 9: *End the while cycle comparing the following condition, if* $R_j - 1 < 1 \times 10^{-6}$, then break the cycle.

6.2.2 Numerical validation using Finite Element Analysis

To evaluate the proposed algorithm in the above section, numerical experiments are considered through finite element analysis.

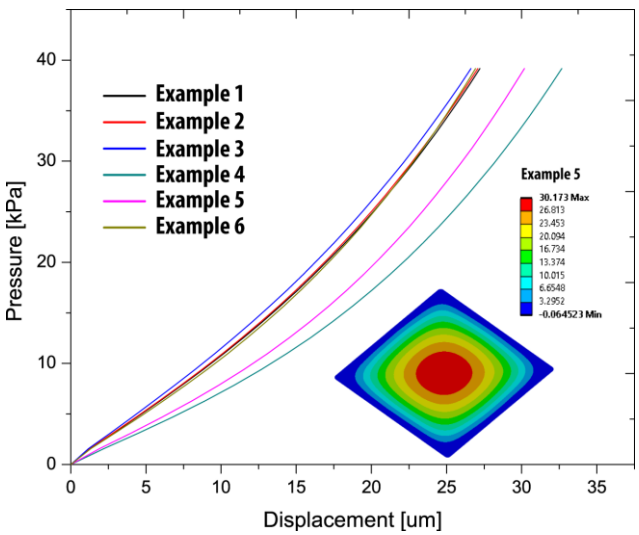

Figure 6.4. Load-deflection curves for six examples solve by finite element analysis.

It is important to denote that these are designed with aim to characterize a bilayer film made from silicon nitride (as substrate) and aluminum as study case. Therefore, the elastic properties are close

from the real properties of the material. Let's consider a bilayer thin film $2mm \times 2mm$ with the following dimensions $a = 1mm, t_A = 1760nm, t_B = 500nm.$ Six cases were designed for validating the numerical procedures proposed. Table 6.1 list the mechanical properties for all the considered examples.

Table 6.1. Mechanical properties for the six numerical examples

	Input parameters – FEM models					**FEM outputs**	
Numerical example	Poisson's ratio ν		Young's modulus [Gpa]		Input (B.C.) σ_r [MPa]	Residual stress σ_r [MPa] in the center $\sigma_r > \sigma_{r0}$ **Stress intensity**	
Item	**Substrate B**	**Film A**	**Substrate B**	**Film**	**Substrate- B** $\sigma_{r(B)}$	**Substrate- B** $\sigma_{r(B)}$	**Film** $\sigma_{r(A)}$
1	0.267	0.32	236.22	64	264.8	264.08	77.44
2	0.267	0.26	236.22	69	264.8	264.08	76.7
3	0.267	0.28	236.22	60	300	298.67	77.55
4	0.267	0.23	236.22	70	200	199.45	40.35
5	0.267	0.20	236.22	80	180	179.17	55.82
6	0.267	0.24	236.22	90	220	218.75	80.75

Applying the procedures described in the section 6.1 to simulate a bulging test, the six examples were simulated by finite element analysis. In all examples, the maximum bulge pressure was 40 kPa. The mechanical properties of the substrate are considered fix since the main objective is perform predictions over the added second film in a bilayer configuration. Only, the residual stresses $\sigma_{r(B)}$ is considered as input parameter in the first stage of solution. In the second stage is seen that the residual stress is $\sigma_{r(B)}$ higher than in the film $\sigma_{r(A)}$ due to fact that if the residual stress are lower in the substrate, compressive stresses can produce buckling which is a configuration with mechanical instabilities (Shafqat et al., 2018). The results of all virtual experiments are illustrated in Figure 6.4, which shows all load-deflections obtained from simulations as well there is plotted the displacement field for the example 5.

Following section 6.2.1, the first step was to determine the constants (C_1 and C_2) applying least square fitting to the equation (6.6), these constants depend on the associated terms in this equation. Residual stress is related to the first term, and elasticity is related to the second term as described in previous chapters. The most important step at this stage is to estimate the constant value of C_1 since it will be used for all subsequent estimations of $\sigma_{r(bi)}$. For each example a pair of C_1 and C_2 values were estimated, this using all properties of each example, the obtained results are listed in Table 6.2.

Table 6.2. Predictions determined using the numerical strategy (proposed algorithm)

Numerical example	Constants determined with Eq. (6.6)		Residual stresses [MPa] $C_1 = 3.817$ (estimated)			Prediction Error [%]	
Item	C_1	C_2	$\sigma_{r(bi)}$	**Substrate** σ_{rB} **Predicted**	**Film** σ_{rA} **Predicted**	**Substrate**	**Film**
1	3.78	2.46	117.61	265.55	75.2	0.55	2.89
2	3.83	2.38	118.82	267.19	76.28	1.17	0.54
3	3.81	2.37	126.49	286.48	81.44	4.08	5.01
4	3.94	2.45	76.20	171.35	48.92	14.08	21.23
5	3.87	2.40	84.39	189.77	54.18	5.91	2.93
6	3.64	2.37	112.98	255.38	72.88	16.74	9.74

The mean values calculated for those parameters were $C_1 = 3.817 \pm 0.1$ and $C_2 = 2.41 \pm 0.042$. Since the objective is to predict residual stresses for both films based on load-deflection data, C_2 value is not relevant at this stage. Therefore, $C_1 = 3.817 \pm 0.1$ is used in Equation (6.6) for all examples as standard value, and posteriorly $\sigma_{r(bi)}$ values were estimated applying least square fitting with the load-deflection data used as input parameters. $\sigma_{r(bi)}$ value is key in the determination of the residual stress of the substrate and the study film. Applying the algorithm described in the section 6.2.1, σ_{rA} and σ_{rB} were predicted for each example. These residual stresses are shown in the Table 6.2. It is observed that the relative errors are in between 0.5% to 21% as the maximum, which demonstrates that there is an acceptable accuracy grade. This means that the algorithm to estimate the residual stresses individually for each film can predict the residual stresses. As final point, it is pointed out that for the real application the prediction of the σ_{rB} will be used as input in the finite element model, this is an advantage since the model is dependent on the σ_{rB} parameter. σ_{rA} computed from equilibrium condition solved in the stage II of the procedure described in Section 6.1.

6.3 Experimental validation for a bilayer thin film of Si3N4 (substrate) and Al subjected a bulge testing

6.3.1 Determination of the residual stresses for Si_3N_4 (substrate) and Al

For the bulging experiments, a bilayer thin film was manufactured using supporting films supplied by Norcada (Norcada Inc., Edmonton, Canada). These are composed of a silicon frame with square hole of 2x2mm, covered by Si_3N_4 thin film, with $t_B = 500nm.$. These films were tested through bulging test as described in Chapter 2 and 3, in which the properties are known and determined by the procedures developed in this work. SEM (Scanning electron microscopy) and TEM (transmission electron microscopy) observations indicate that Si_3N_4 monolayer structure does not exhibit a diffraction pattern, therefore, it is considered that the films are amorphous and isotropic.

To configure a bilayer structure, a thin aluminum film was deposited on the substrate of Si_3N_4. A SEM image can be seen in the study published by Holzer et al. (2017b). It can be observed a single

crystalline silicon at the bottom part, and the layers of Si_3N_4 and Aluminum with thickness of 1.76 ± 0.2 µm (for this study). During magnetron sputtering, the aluminum layer grows from many nucleation centers, then becomes columnar when it overruns grains with preferential orientation. By SEM, it was observed that the surface grains were smaller than 0.5 m in direction parallel to the surface. The setup described in section 1.6 was used for the bulging tests, as described before pressure is applied from the bottom on the substrate that for this experiment is composed by the Si_3N_4 membrane.

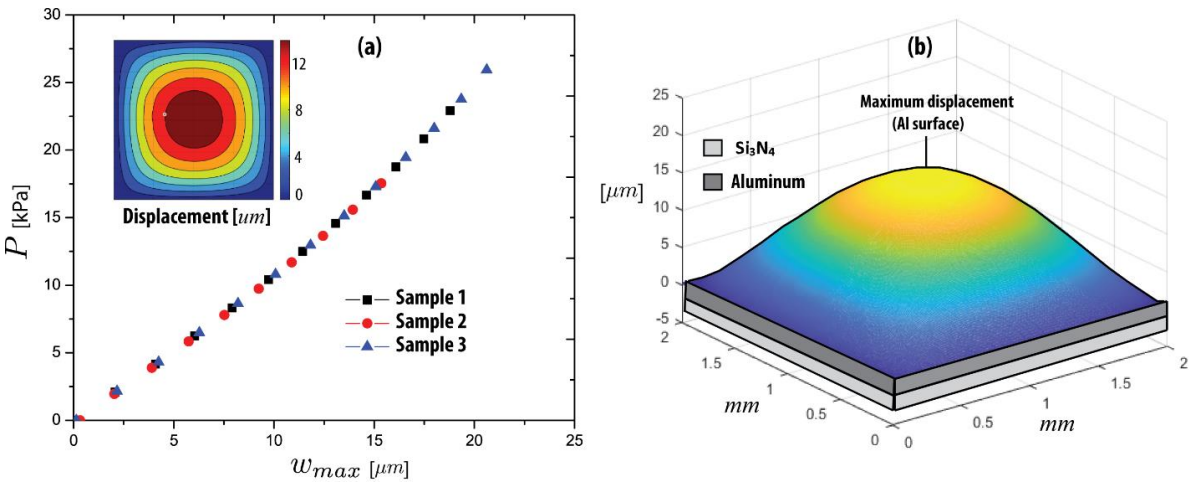

Figure 6.5. (a). Load-deflection data for three samples (Si_3N_4/ Al). (b) Measured deflection surface.

Three samples were considered for the characterization process, the load-deflection curves obtained from the maximum deflection point measured on the aluminum surface are shown in Figure 6.5a. It is observed the degree of repeatability of the tests is quite good since the data are not scattered. The interval of pressure was chosen lower than 25 kPa to avoid the plasticity influence therefore certain degree of linearity is kept in the load-deflection observations. Figure 6.5b illustrates the deflection surface measured with the interferometric system used for this study, from the central point is obtained the maximum deflection of the films.

Table 6.3. Predictions determined for σ_{rA} and σ_{rB} using the numerical strategy

Experimental case	**Residual stresses [MPa]** $C_1 = 3.817$ **(estimated)**		
Sample	$\sigma_{r(bi)}$	**Si_3N_4** σ_{rB} **Estimated (Input B.C. FEM)**	**Al** σ_{rA} **estimated**
1	117.93	267.48	75.82
2	115.77	260.33	74.32
3	117.68	265.39	75.33

Using the load-deflection data, $\sigma_{r(bi)}$ values were estimated for each sample from Equation (6.6), with those values, the developed algorithm and explained in section 6.2.1 is ran for estimating the residual

stresses of Si_3N_4 and Al, which are listed in Table 6.3. Results shows that in average the residual stress for Si_3N_4 is 264.4 ± 3.67 MPa and for the Aluminum is 75.15 ± 0.76 MPa. These values are key for characterization of the bilayer using finite element analysis. The values estimated for σ_{rB} will be the boundary conditions (B.C.) for the finite element models. It noted that for the Si_3N_4 film that the residual stresses were increased from 166 Mpa (computed for monolayer in previous chapters) to 264.4 Mpa for the bilayer case, which demostrates a new stress redistribution.

6.3.2 Determination of the elastic properties for Si_3N_4 (substrate) and Al (Aluminum)

For the determination of the elastic properties in a bilayer configuration, analytical models simplify the process, but if most of the parameters are known these can be non-useful. In the majority of cases, authors assume the properties of some parameters as Poisson's ratio and Young's modulus of the substrate. But in this particular case, the substrate properties (Si_3N_4) were calculated in previous chapters (2 and 3) with several methodologies as listed in the Table 6.4. To estimate Young's modulus, equation 6.5 is reorganized in such a way that $E_A = (t_{bi}/t_A)(E_{bi} - (t_B/t_{bi})E_B)$. The value for E_{bi} is estimated using least square fitting on the equation (6.6), experimental data of P and w_0 are neccesary for the computations as well as the residual stress $\sigma_{r(bi)}$ calculated in the Table 6.3.

Table 6.4. Silicon nitride Si_3N_4 elastic properties and Al elastic estimations

No. Sample	Methodology	ν	E_B [MPa] Si_3N_4	E_{bi} [GPa] $C_2 = 2.41$ (bilayer)	E_A [GPa] (Al)
1	Chapter 2	0.264	236.22	105.23	68.01
2				113.93	69.08
3				104.88	68.23
1	Chapter 3 (rectangular)	0.278	232.45	105.23	79.18
2				113.93	80.25
3				104.88	79.40
1	Chapter 3 (square)	0.254	235.45	105.23	67.56
2				113.93	68.63
3				104.88	67.78
1	Mean value	0.265	234.7	105.23	67.56
2				113.93	68.63
3				104.88	67.99

For each sample combined with each methodology (used for determining ν and E - Si_3N_4), E_{bi} and E_A values are estimated. $C_2 = 2.41$ constant was calculated in section 6.2.2 with the numerical experiments. To condense the Table 6.4, mean values of for the E_A were calculated with the aim to perform finite element simulations to determine which combination of properties satisfy better the experimental data of the sample 1 with higher accuracy. Four finite element solution were proposed, one for each methodology and the properties of each case are described in Table 6.5.

Table 6.5. Silicon nitride Si_3N_4 elastic properties and Al elastic estimations for FEM models.

Experimental case	**Values Table 6.3**	**Stress intensity at the center point [MPa]**		**Input FEM Poisson's ratio**		**Input FEM Young's Modulus [GPa]**		**Computed from (6.5)**
Sample 1	Input (stage I -B.C.)	Output (Stage II) FEM σ_{rB}	Output (Stage II) FEM σ_{rA}	**Si_3N_4**	**Al**	**Si_3N_4**	**Al Mean**	**Bilayer** E_{bi}
Chapter 2 - S11	267.48	268.21	66.05	0.264	0.3	236.22	68.44	105.55
Chapter 3 (R) - S12	267.48	268.21	76.33	0.278	0.3	232.45	79.61	113.42
Chapter 3 (Sq) – S13	267.48	268.21	66.88	0.254	0.3	235.45	67.99	105.03
Means value -S14	267.48	268.21	66.00	0.265	0.3	234.7	68.06	104.92

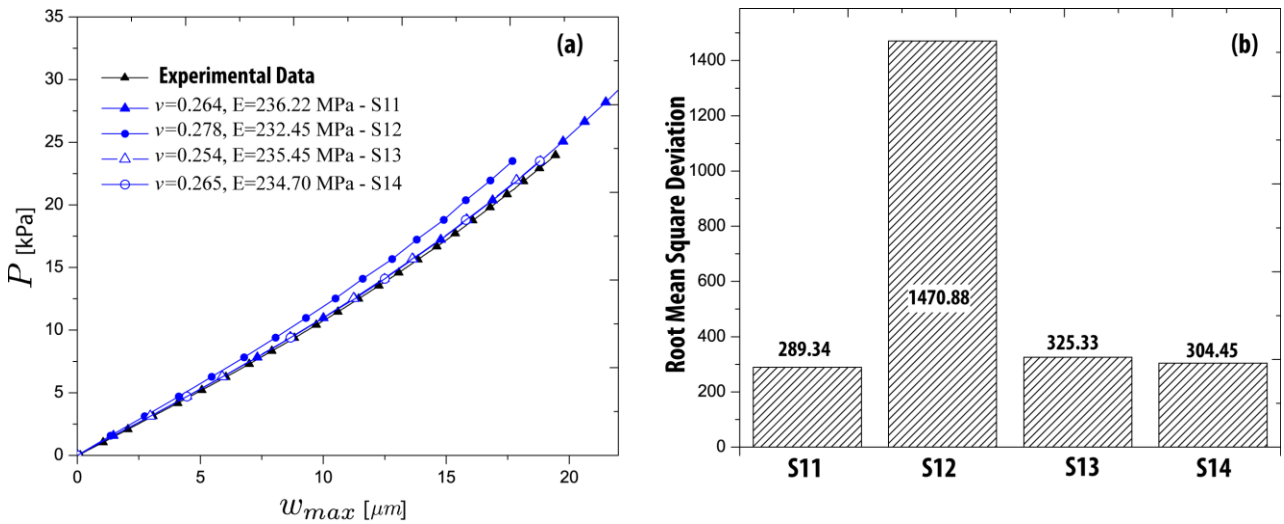

Figure 6.6. (a) Finite element approximations for the Sample 1. (b) Root mean square deviation for the FEA approximations for Sample1.

The results of all simulations are shown in Figure 6.6a. Some of the solutions are closer to the experimental values than others, for example, methodology S11, S13, and S14. In contrast to the FEM solution for case S12, the load deflection curve does not agree with these parameters. A root mean square deviation is proposed to determine which set of parameters is most compatible with the experimental data. It can be seen in Figure 6.6b. The methodology S11 provides the most accurate fit for sample 1, so all properties are appropriate except the Poisson's ratio, which was not defined correctly.

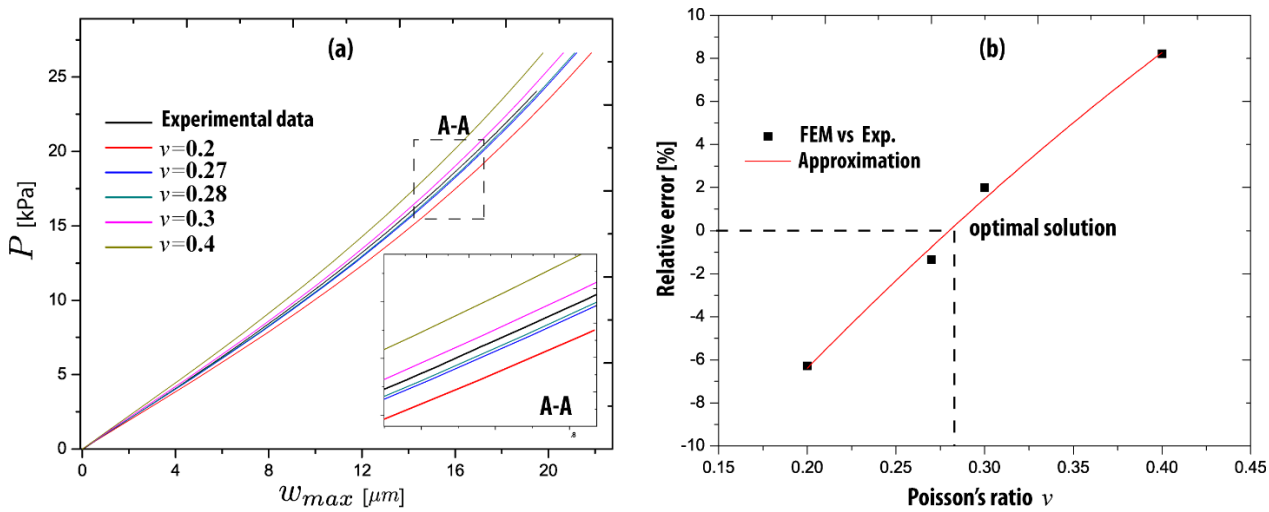

Figure 6.7. (a) Finite element approximations for the Sample 1. (b) Non-absolute relative error for the FEA approximations for the sample 1.

In order to estimate Poisson's ratio optimally, several cases were proposed. There are five Poisson's ratios defined as 0.2, 0.27, 0.28, 0.3, and 0.4. The solutions are shown in Figure 6.7a. There is a good match between the experimental curve and the closest curve within 0.27 and 0.3. A relative error function was computed to observe optimal solutions, which was found in 0.28, approximately. For the sample 2 and 3, the optimal set of parameters is used for the simulations (see Table 6.6). Figure 6.8a Illustrates the results, which show a good correlation with the experimental curve of the sample 2. The maximum principal stresses at the central point of each film were measured during pressure application, as shown in Figures 6.8b and 6.8c.

Table 6.6. Parameters for FEM models.

Experimental case		**Residual stress at the center point [MPa]**		**Poisson's ratio**		**Young's Modulus [GPa]**	
No. Sample	Input (stage I - B.C.)	Output (Stage II)	Output (Stage II)	**Si_3N_4**	**Al**	**Si_3N_4**	**Al**
1	267.48	268.21	66.07	0.264	0.28	236.22	68.44
3	265.39	261.11	62.51	0.264	0.28	236.22	68.44
2	260.33	260.99	64.27	0.264	0.28	236.22	68.44

For the Al film, the stress levels reached 102 MPa for 19.3 *um* and 320 MPa for the Si_3N_4 film. In those curves, it is possible to denote the residual stresses at the beginning of the curves, these values represent the initial stresses before submitted to the pressure conditions. From the Table 6.3, there are compared the obtained values from the residual stress predictions for each film. The FEM solution (Al thin film) yielded 77.32 MPa and the predicted value (sample 2) yielded 74.32 MPa. For the Si_3N_4 thin film the calculations evidenced 261 from FEM and 260.33 from the proposed algorithm (Input for FEM). These results confirm that the proposed methodology show a consistency in the properties estimations for this

specific case. As conclusion, the properties for the Al thin film are E=68.44 GPa, $\sigma_{rAl} = 75.15$ MPa, v=0.28. These values correspond to real values for the aluminum in bulk shape and thin films (Feng & Kang, 2008).

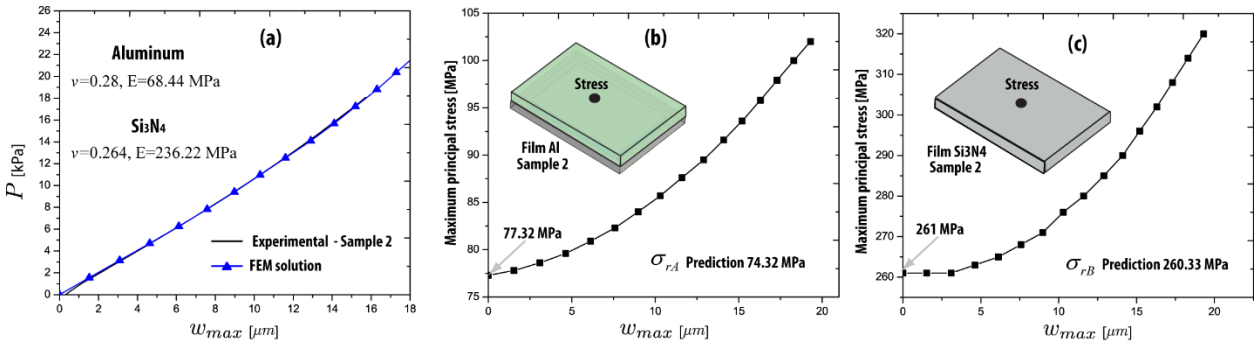

Figure 6.8. (a) Finite element approximations for the Sample 2. (b) Maximum principal stress in the central point for Al. (c) Maximum principal stress in the central point for Si_3N_4.

In general, the methodology presented in this chapter showed to be useful in the characterization of bilayer films subjected to bulging test. These procedures can be improved, but the main contribution of the methodology is the capacity to estimate the residual stresses in both films as well both elastic properties.

Chapter 7. Conclusions

In chapter two, a numerical approach to determining the elastic properties of monolayer thin films was described and applied. The bulging analysis of monolayer films was used to test two types of geometry in separate tests. Numerical solutions were obtained by combining two standard methods, namely finite element analysis and classical analytical solutions. A new way to simulate the bulging problem was discussed and used to reproduce the experimental tests. Bulging tests were conducted on silicon nitride (Si3N4) monolayer of 2×2 mm (square) and 3.5×1.5 mm (rectangular) membranes to determine their elastic properties (Young's modulus (E) and Poison's ratio (v)). Using mapping of elastic parameters for the two membranes (square and rectangular), an error function was constructed for each membrane. As a result of the intersection of both linear approximations minimized, a unique solution was obtained for E with 236 GPa and v with 0.264. According to the results, the estimated elastic properties agree with those reported in the literature. A traditional bulging test analysis can only determine one of both biaxial modulus, not a combination of E and v, which is a contribution of this thesis. As the main conclusion of this chapter, it was demonstrated that Young's modulus and Poisson's ratio are mechanically coupled in the bulging problem, allowing a unique determination of both elastic constants. Since a traditional bulging test analysis only finds one of these constants.

Chapter three presented a numerical approach for identifying the elastic properties of monolayer thin films that simplified the methodology presented in chapter two. As a result of applying part of the procedures previously presented, the methodology was improved by only using data from one monolayer film. Also, it demonstrated the validity of using a virtual boundary for the bulging test modeling by finite element analysis. Monolayer membranes made from silicon nitride and gold were studied to test the validity of the procedures designed. Based on the error functions, Young's modulus and Poison's ratio were delimited by a solution space that minimized the error function, this domain presents a correlation among both elastic properties. This proves that Young's modulus and Poison's ratio are coupled. The found solutions for silicon nitride films (square and rectangular) were E= 232.45 GPa and v= 0.278 for a square film, and E= 235.45 GPa and v= 0.254 for a rectangular film. Additionally, for the gold film, the elastic properties were E= 80.55 GPa and v= 0.425 for a rectangular film. The procedures developed showed to be useful to characterize thin films by bulge testing, due to the lack of a unique solution in the estimation of these by a traditional bulged analysis.

The purpose of chapter 4 was to describe novel modeling of stress and strain for freestanding square thin films under bulge testing, considering the elastoplastic behavior as a primary focus. Finite element simulations were conducted as virtual experiments to demonstrate the validity of the proposed analytical models. The FEA modeling procedures included a description of the application of residual stresses in thin films since the detailed description of the FEM modeling found in the literature is not clearly detailed. A more realistic simulation was achieved by including the manufacturing factor (pre-stressed film) at the boundary conditions of FEM models. The validation of the stress-strain models developed for bulge testing showed good agreement with the finite element results. These approximated the stresses better than strains, specifically in the regime where the elasticity effects were more visible in the load-deflection curves. These results validated that the proposed analytical equations predict the stress and strain in a freestanding square thin film under bulge testing. These

new results show that the proposed equations can be useful for characterizing thin square films in the elastoplastic regime.

In the chapter five was presented an elasto-plastic analysis conducted for a non-cracked and pre-cracked gold thin film applying finite element analysis. For the analysis of a pre-cracked film, a numerical solution of two stages was proposed with the aim to determine the fracture parameters at the crack tip. Elasto-plastic results correlated the load-deflection curves for non-cracked and pre-cracked films with the same material law. It indicated that the proposed models presented a good correlation and robustness. There were found values of fracture toughness (between 0.288 and 0.303 $MPa \cdot m^{0.5}$) for different notches; rounded, sharp, and V-sharp. The calculated values corresponded with other values reported in the literature.

Further, this chapter described a methodology to estimate mechanical parameters of thin films using the experimental data from the bulging test. The biaxial stress-strain curve, yield stress at the central point, and residual stress and its evolution were determined with high precision for an Aluminum (Al) square thin film. Load-deflection measurements were performed during the bulging process in conditions of cycling loading. The obtained results showed that plasticity effects were detected in the third cycle. Non-linear (plastic) behavior of the film started at the stress value of 132 MPa; this value is the yield stress of the film in a condition of biaxial tensile loading. Increasing plasticity was detected in the next applied loading cycles, showing a non-proportional shifting of the stress-strain curve in each loading cycle, which indicated that the plasticity effects were cumulative. Further, an analytical model was presented to determine the residual stress values without the necessity to apply equations. The result showed good agreement with other values obtained by using classical methods.

In chapter six, freestanding bilayer films were characterized. A challenge addressed was focused on determining residual stresses in each film after a bulging test. Based on equilibrium conditions as well as analytical models for multilayer films, an algorithm was developed to estimate both residual stresses. A virtual (finite element solution) and experimental evaluation of the algorithmic procedure was conducted. As a result of numerical experiments, residual stress predictions presented relative errors between 2% for the best case and 21% for the worst case. As part of the experiments, three samples of silicon nitride/aluminum were evaluated with the aim of determining residual stresses and elastic properties, as well as validating numerical methods. In conclusion, the Al thin film properties were determined as E=68.44 GPa, $\sigma_{rAl} =$=75.15 MPa, v=0.28. Since these values agree with standard values determined for thin aluminum films, which shows that the presented methodology can be applied to other materials.

Papers Published During the Ph.D.

Papers published in Journals related with the thesis:

- **Tinoco, H. A**., Fintova, S., Heikkila, I., Herrero, D., Vuoristo, T., Dlouhy, I., & Hutar, P. (2022). "**Experimental and numerical study of micromechanical damage induced by MnS-based inclusions**". Materials Science and Engineering: A, 144009. (Elsevier). https://doi.org/10.1016/j.msea.2022.144009
- **Tinoco, H.A**.; Pavel Hutař, Tomáš Kruml, and Jakub Holzer. 2021, "**Modeling of Elastoplastic Behavior of Freestanding Square Thin Films Under Bulge Testing**", Acta Mechanica (SPRINGER). Vol. 232, p. 2715–2731. https://doi.org/10.1007/s00707-021-02978-7
- **Tinoco, H. A**., Holzer, J., Pikálek, T., Sobota, J., Fořt, T., Matějka, M., & Hutař, P. (2021, February). **Determination of the yield stress in Al thin film by applying bulge test**. In Journal of Physics: Conference Series (Vol. 1777, No. 1, p. 012030). https://iopscience.iop.org/article/10.1088/1742-6596/1777/1/012030
- **Tinoco, H. A**.; Hutař, P., Merle, B.; Göken, M.; Kruml, T. 2020, "**Fracture Toughness Evaluation of a Cracked Au Thin Film by Applying a Finite Element Analysis and Bulge Test**", Key Engineering Materials. Vol. 827. pp.196-202. https://doi.org/10.4028/www.scientific.net/KEM.827.196
- **Tinoco, H. A**., Cardona, C. I., Vojtek, T., & Hutař, P. 2019 "**Finite element analysis of crack-tip opening displacement and plastic zones considering the cyclic material behaviour**", Procedia Structural Integrity (Elsevier), 23, 529-534. https://doi.org/10.1016/j.prostr.2020.01.140
- **Tinoco, H. A**.; Holzer, J.; Pikálek, T.; Buchta, Z.; Lazar, J.; Alice, C.; Kruml, T. 2019, "**Determination of Elastic Parameters of Si3N4 Thin Films by Means of a Numerical Approach and Bulge Tests**", Thin Solid Films (Elsevier). Vol. 672. pp.66-74.

Conferences presented related with the thesis:

- **Tinoco, H. A**.; J Holzer, T Pikálek, J Sobota, T Fořt, Matějka, T Kruml, P Hutař. **2020, "Determination of the yield stress in Al thin film by applying bulge test",** Proceedings of *9th Global Conference on Materials Science and Engineering (CMSE 2020)*. November 20-23, 2020 Online Conference. http://www.cmseconf.org/
- **Tinoco, H. A**.; Hutař, P., Merle, B.; Göken, M.; Kruml, T. **"Fracture Toughness Evaluation of a Cracked Au Thin Film by Applying a Finite Element Analysis and Bulge Test",** 18*th International Conference on Fracture and Damage Mechanics*, Rodos, Greece, 16-18 September 2019.
- **Tinoco, H.A**.; Cardona, C.I.; Vojtek, T., Hutař, P. **"Finite Element Analysis of Crack-tip Opening Displacement and Plastic Zones Considering the Cyclic Material Behavior", In:** *9th International Conference on Materials Structure & Micromechanics of Fracture*, Brno, Czech Republic, 26-29 June, 2019. ISBN: 978-80-5760-7
- **Tinoco H.A.,** Holzer, J., Pikálek, T., Buchta, Z., Lazar, J., Chlupová, A., Sobota, J., Fořt, T., Kruml, T., Hutař, P. **"Numerical modeling approach for the assessment of elastic properties of bi-layer thin films measured by bulge Test"**, In: *Tenth International Conference on Engineering Computational*, *Sitges-Barcelona*, *Spain.* pp. 1-5. 4-6, September, 2018. **DOI** http://doi.org/10.31224/osf.io/qypw4
- **Tinoco, H. A**.; Holzer, J.; Pikálek, T.; Buchta, Z.; Lazar**,** J.; Alice, C.; Kruml, T. **"Estimation of Mechanical Parameters of Thin Films Using Finite Element Analysis",** In: *Proceedings of 20th*

International Conference of applied Mechanics. Myslovice, Czech Republic. pp. 157-162, April, 2018. http://doi.org/10.31224/osf.io/3adt5 ISBN 978-80-261-0766-8

Papers published (24) non-related with the thesis:

- Tinoco, H. A., Buitrago-Osorio, J., Perdomo-Hurtado, L., Lopez-Guzman, J., Ibarra, C. A., Rincon-Jimenez, A., ... & Berrio, L. V. 2022. **Experimental Assessment of the Elastic Properties of Exocarp–Mesocarp and Beans of Coffea arabica L. var. Castillo Using Indentation Tests.** Agriculture, 12(4), 502. http://dx.doi.org/10.3390/agriculture12040502
- Buitrago-Osorio, J., Tinoco, H. A., Perdomo-Hurtado, L., Rincon-Jimenez, A., Ocampo, O., Berrio, L. V., & Lopez-Guzman, J. 2022. **Physical-mechanical characterization of coffee fruits Coffea arabica L. var. Castillo classified by a colorimetry approach**. Materialia, http://dx.doi.org/101330.10.1016/j.mtla.2022.101330
- Slávik, O., Vojtek, T., Poczklán, L., Tinoco, H. A., Kruml, T., Hutař, P., & Šmíd, M. 2022. **Improved description of low-cycle fatigue behaviour of 316L steel under axial, torsional and combined loading using plastic J-integral**. Theoretical and Applied Fracture Mechanics (Elsevier), 103212. http://dx.doi.org/10.1016/j.tafmec.2021.103212
- Cardona, C. I., Tinoco, H. A., Perdomo-Hurtado, L., López-Guzmán, J., & Pereira, D. A. 2021. **Vibrations Analysis of the Fruit-Pedicel System of Coffea arabica var. Castillo Using Time–Frequency and Wavelets Techniques.** Applied Sciences, 11(19), 9346. 10.3390/app11199346
- Jimenez, J., Tinoco, H.A.; Cardona, C.I.; Gomez, J.P.; Jimenez, F.N.; Roldan-Restrepo, S.I. 2021 **Identification of Bone Density Changes Applying Impedance Spectroscopy with a Piezo-Device Coupled to a Human Tooth**, Journal of Biomimetics, Biomaterials and Biomedical Engineering), Vol. 52, p. 1-10. 10.4028/www.scientific.net/JBBBE.52.1
- Rincon-Jimenez, A., Tinoco, H. A., Buitrago-Osorio, J., Ocampo, O., Berrio, L. V., Rodriguez-Sotelo, J. L., & Arizmendi, C. 2020. **Ripeness stage characterization of coffee fruits (coffea arabica L. var. Castillo) applying chromaticity maps obtained from digital images**. Materials Today: Proceedings (ELSEVIER). Vol. 44, p. 1271-1278. http://dx.doi.org/10.1016/j.matpr.2020.11.264
- Cardona, C.I.; Tinoco, H.A.; Maribel M.B.; Juliana, G.; Gomez, J.P.; Roldan-Restrepo, S.I.; Jimenez, J. 2020. "**Electromechanical impedance measurements for bone health monitoring through teeth used as probes of a Piezo-device**", Biomedical Physics & Engineering Express (IOP), p. 1-15. http://dx.doi.org/10.1088/2057-1976/abc099
- Tinoco, H.A.; Cardona, C.I.; Maribel M.B.; Juliana, G.; Gomez, J.P.; Roldan-Restrepo, S.I.; Adam, B.; Dominika, K.; Zikmund, T.; Kaiser, J. 2020 "**Bio-structural monitoring of bone mineral alterations through electromechanical impedance measurements of a Piezo-device joined to a tooth**", Biomedical Engineering Letters (SPRINGER), 1-15.http://dx.doi.org/10.1007/s13534-020-00170-9
- Tinoco, H.A.; Barco, D.R.; Ocampo, O.; Buitrago-Osorio, J.. 2020 "**Geometric Modeling of the Valencia Orange (Citrus sinensis L.) by Applying Bézier Curves and an Image-Based CAD Approach**", Agriculture, 10(8), 313-325. http://dx.doi.org/10.3390/agriculture10080313
- Barco, D.R; Tinoco, H.A.; Cardona, C.I.; Peña, F.M. 2019, "**Piezo-actuated device for a bio-structural monitoring application through vibration-based condition and electromechanical impedance measurements**", IOP Conference Series: Materials Science and Engineering. Vol. 657. pp. 1-7. http://dx.doi.org/10.1088/1757-899X/657/1/012031
- Vargas, C.A., Tinoco, H.A. 2019. **Electrical Performance of a Piezo-inductive Device for Energy Harvesting with Low-Frequency Vibrations. Actuators**, Vol. 8(3), pp. 55. 10.3390/act8030055

- Tinoco, H. A., & Durango, S. 2019. **Tolerance Analysis of Planar Mechanisms Based on a Residual Approach: A Complementary Method to DLM**. Mathematical Problems in Engineering, Vol. 2019, 9067624, pp. 1-13. http://dx.doi.org/10.1155/2019/9067624
- Tinoco, H.A., Peña F.M. 2019, "**Mechanical and geometrical characterization of fruits Coffea arabica L. var. Colombia to simulate the ripening process by finite element analysis**", Engineering in Agriculture, Environment and Food. (Elsevier). Vol. 12(3), pp. 367-377. http://dx.doi.org/10.1016/j.eaef.2019.04.004
- Tinoco, H.A.; Cardona, C.I.; Peña F.M.; Gomez, J.P.; Roldan-Restrepo, S.I.; Velasco-mejia, M.A.; Barco, D.R. 2019, " **Evaluation of a Piezo-Actuated Sensor for Monitoring Elastic Variations of Its Support with Impedance-Based Measurements**", Sensors. Vol. 19. No. 1, 184. http://dx.doi.org/10.3390/s19010184
- Tinoco, H.A.; Cardona, C.I.; Peña F.M.; Gomez, J.P.; Roldan-Restrepo, S.I. 2018. "**Assessment of Material Loss in a Human Teeth Support by Applying EMI Technique**", International Journal of Mechanical & Mechatronics Engineering. Vol. 18, No. 4, pp. 113-120.
- Tinoco, H.A., Peña F.M. 2018, "**Finite Element Analysis of Coffea Arabica L. var. Colombia Fruits for Selective Detachment using Forced Vibrations**", Vibration (MDPI). Vol. 1 No.1, pp. 207-219. . https://doi.org/10.3390/vibration1010015
- Tinoco, H. A. 2018. "**Modeling of piezoelectric sensors adhesively bonded on trusses using a mathematical programming approach**", Structural and Multidisciplinary Optimization (Springer). http://dx.doi.org/10.1007/s00158-018-1933-3.
- Tinoco, H.A.; Peña F.M. 2017, "**Harmonic Stress Analysis on Coffea Arabica L. var. Colombia Fruits In Order to Stimulate the Selective Detachment: A Finite Element Analysis**", Simulation (SAGE). Vol. 94, No. 1, pp. 163-174. http://dx.doi.org/10.1177/0037549717738068
- Cardona M.J., Castrillon, O. D.; Tinoco, H.A.. 2017, "**Aplicación del algoritmo Dijkstra para determinar el método óptimo de operaciones de ensamble bimanual**", Información Tecnológica. Vol. 28, No. 4, pp. 1-8. http://dx.doi.org/10.4067/S0718-07642017000400015
- Tinoco, H.A.; Gomez, J.P. 2017. "**Bone Mineral Density (BMD)**", Current Trends in Biomedical Engineering & Biosciences. Vol. 2, No. 1, pp. 1-2. https://doi.org/10.19080/CTBEB.2017.02.555576
- Tinoco, H.A.; Gomez, J.P.; Torres, J.; Velasco-Mejia; M.A. 2017, "**Identification of Stiffness Variations in Supporting Substances of a Human Tooth Canine with a Bracket-Beam-Piezoelectric Sensor and its Electromechanical Impedance**", Future Dental Journal (Elsevier). Vol. 3, No. 1, pp. 15-21. http://dx.doi.org/10.1016/j.fdj.2017.03.001
- Tinoco, H.A.; Ocampo, O.L., Diaz, C.A. 2017, "**Performance Assessment in a Voice Coil Motor for Maximizing the Energy Harvesting with Gait Motions**", World Academy of Science, Engineering and Technology, Vol. 11, No. 2, pp. 1-5.
- Tinoco, H.A. 2017, "**Modeling Elastic and Geometric Properties of Coffea arabica L. var. Colombia fruits by an Experimental-Numerical Approach**", International Journal of Fruit Science (Taylor and Francis). Vol. 17, No. 2, pp. 159-174. http://dx.doi.org/10.1080/15538362.2016.1270249
- Tinoco, H. A. 2017. "**Numerical Limit Analysis of Reinforced Concrete Slabs Using a Dual Approach and Conic Programming**", Structural and Multidisciplinary Optimization (Springer). Vol. 55, No. 4, pp. 1407-1423. http://dx.doi.org/10.1007/s00158-016-1582-3

References

Abedin, M., Maleki, S., Kiani, N., & Shahrokhinasab, E. (2019). Shear lag effects in angles welded at both legs. Advances in Civil Engineering, 2019.

Alaboodi, A. S., & Hussain, Z. (2017). Finite element modeling of nano-indentation technique to characterize thin film coatings. Journal of King Saud University-Engineering Sciences. 31(1), 61-69.

Beams, J.W. (1959). Mechanical properties of thin films of gold and silver, in Structure and Properties of Thin Films, edited by C.A. Neugebauer, J.B. Newkirk, and D.A. Vermilyea (John Wiley and Sons, New York, 1959), p. 183.

Bei, H., Shim, S., Pharr, G. M., & George, E. P. (2008). Effects of pre-strain on the compressive stress–strain response of Mo-alloy single-crystal micropillars. Acta Materialia, 56(17), 4762-4770.

Birleanu, C., Pustan, M., Merie, V., Müller, R., Voicu, R., Baracu, A., & Craciun, S. (2016). Temperature effect on the mechanical properties of gold nano films with different thickness. In IOP Conference Series: Materials Science and Engineering (Vol. 147, No. 1, p. 012021). IOP Publishing.

Boe, A., Safi, A., Coulombier, M., Pardoen, T., & Raskin, J. P. (2009). Internal stress relaxation based method for elastic stiffness characterization of very thin films. Thin Solid Films, 518(1), 260-264.

Bonnotte, E., Delobelle, P., Bornier, L., Trolard, B. and Tribillon, G. (1997). "Two interferometric methods for the mechanical characterization of thin films by bulging tests. Application to single crystal of silicon," Journal of Materials Research, vol. 12, 1997, p. 2234–2248

Bozkurt, M., Ayhan, A. O., Yaren, M. F., & Siriç, S. (2016). Finite element modeling and experimental studies on mixed mode-I/III fracture specimens. Frattura ed Integrità Strutturale, 10(35), 350-359.

Budiansky, B. (1968). Notes on nonlinear shell theory. J. Appl. Mech. 35, 393–440

Chang, J. Y., Yu, G. P., & Huang, J. H. (2009). Determination of Young's modulus and Poisson's ratio of thin films by combining sin2ψ X-ray diffraction and laser curvature methods. Thin Solid Films, 517(24), 6759-6766.

Charitidis, C. A. (2010). Nanomechanical and nanotribological properties of carbon-based thin films: a review. International Journal of Refractory Metals and Hard Materials, 28(1), 51-70.

Chason, E., & Guduru, P. R. (2016). Tutorial: Understanding residual stress in polycrystalline thin films through real-time measurements and physical models. Journal of Applied Physics, 119(19), 191101.

Chou, T. L., Yang, S. Y., & Chiang, K. N. (2011). Overview and applicability of residual stress estimation of film–substrate structure. Thin Solid Films, 519(22), 7883-7894.

Das, S., Guha, S., Ghadai, R., Kumar, D., & Swain, B. P. (2017). Structural and mechanical properties of CVD deposited titanium aluminium nitride (TiAlN) thin films. Applied Physics A, 123(6), 412.

Delfani, M. R. (2018). Nonlinear elasticity of monolayer hexagonal crystals: Theory and application to circular bulge test. European Journal of Mechanics-A/Solids, 68, 117-132.

Deuschle, J. K., Buerki, G., Deuschle, H. M., Enders, S., Michler, J., & Arzt, E. (2008). In situ indentation testing of elastomers. Acta Materialia, 56(16), 4390-4401.

Díez-Pascual, A. M., Gómez-Fatou, M. A., Ania, F., & Flores, A. (2015). Nanoindentation in polymer nanocomposites. Progress in Materials Science, 67, 1-94.

Dimiduk, D. M., Uchic, M. D., & Parthasarathy, T. A. (2005). Size-affected single-slip behavior of pure nickel microcrystals. Acta Materialia, 53(15), 4065-4077.

Doerner, M. F., & Nix, W. D. (1986). A method for interpreting the data from depth-sensing indentation instruments. Journal of Materials research, 1(4), 601-609.

Edwards, R. L., Coles, G., & Sharpe, W. N. (2004). Comparison of tensile and bulge tests for thin-film silicon nitride. Experimental Mechanics, 44(1), 49-54.

Eidel, B. (2011). Crystal plasticity finite-element analysis versus experimental results of pyramidal indentation into (0 0 1) fcc single crystal. Acta Materialia, 59(4), 1761-1771.

Engwall, A. M., Rao, Z., & Chason, E. (2016). Origins of residual stress in thin films: Interaction between microstructure and growth kinetics. Materials & Design, 110, 616-623.

Elahi, S. A., Connesson, N., Chagnon, G., & Payan, Y. (2019). In-vivo soft tissues mechanical characterization: volume-based aspiration method validated on silicones. Experimental Mechanics, 59(2), 251-261.

Eom, C. B., & Trolier-McKinstry, S. (2012). Thin-film piezoelectric MEMS. Mrs Bulletin, 37(11), 1007-1017.

Ezhilvalavan, S., & Tseng, T. Y. (1999). Preparation and properties of tantalum pentoxide (Ta 2 O 5) thin films for ultra large scale integrated circuits (ULSIs) application–a review. Journal of Materials Science: Materials in Electronics, 10(1), 9-31.

Feng, C., & Kang, B. S. (2008). Young's modulus measurement using a simplified transparent indenter measurement technique. Experimental Mechanics, 48(1), 9-15.

Freund, L.B. & Suresh, S. (2003). THIN FILM MATERIALS – Stress, Defect Formation and Surface Evolution, University of Cambridge Press, UK, 2003.

Fu, Y., Du, H., Huang, W., Zhang, S., & Hu, M. (2004). TiNi-based thin films in MEMS applications: a review. Sensors and Actuators A: Physical, 112(2-3), 395-408.

Gan, L., Ben-Nissan, B., & Ben-David, A. (1996). Modelling and finite element analysis of ultra-microhardness indentation of thin films. Thin Solid Films, 290, 362-366.

Gao, L., Guo, H., Wei, L., Li, C., Gong, S., & Xu, H. (2015). Microstructure and mechanical properties of yttria stabilized zirconia coatings prepared by plasma spray physical vapor deposition. Ceramics International, 41(7), 8305-8311.

Ghanem, M., Göken, M., & Merle, B. (2017). Plane-strain bulge testing of thin films under compressive residual stresses. Surface and Coatings Technology, 327, 167-173.

Ghazi, N., & Kysar, J. W. (2016). Experimental investigation of plastic strain recovery and creep in nanocrystalline copper thin films. Experimental Mechanics, 56(8), 1351-1362.

Giorleo, L., Ceretti, E., & Giardini, C. (2016). Optimization of laser micromachining process for biomedical device fabrication. The International Journal of Advanced Manufacturing Technology, 82(5), 901-907.

Green, M. A. (2007). Thin-film solar cells: review of materials, technologies and commercial status. Journal of Materials Science: Materials in Electronics, 18(1), 15-19.

Grieveson, E. M., Armstrong, D. E. J., Xu, S., & Roberts, S. G. (2012). Compression of self-ion implanted iron micropillars. Journal of Nuclear Materials, 430(1-3), 119-124.

Gunda, M., Kumar, P., & Katiyar, M. (2017). Review of mechanical characterization techniques for thin films used in flexible electronics. Critical Reviews in Solid State and Materials Sciences, 42(2), 129-152.

Guo, Z., Feng, Z., Fan, S., Zheng, D., & Zhuang, H. (2009). Research development of measuring methods on the tribology characters for movable MEMS devices: a review. Microsystem Technologies, 15(3), 343-354.

Hagerty, P. (2016). Physical Vapor Deposition of Materials for Flexible Two Dimensional Electronic Devices (Doctoral dissertation, University of Dayton).

Haggag, F. M. (1993). In-situ measurements of mechanical properties using novel automated ball indentation system. In Small specimen test techniques applied to nuclear reactor vessel thermal annealing and plant life extension. ASTM International.

Hill, R. (1950). C. A theory of the plastic bulging of a metal diaphragm by lateral pressure. The London, Edinburgh, and dublin Philosophical Magazine and Journal of Science, 41(322), 1133–1142

Hirakata, H., Nishijima, O., Fukuhara, N., Kondo, T., Yonezu, A., & Minoshima, K. (2011). Size effect on fracture toughness of freestanding copper nano-films. Materials Science and Engineering: A, 528(28), 8120-8127.

Hirth, J. P., Lothe, J., & Mura, T. (1983). Theory of dislocations. Journal of Applied Mechanics, 50(2), 476.

Holzer, J.; Pikálek, T.; Buchta, Z.; Lazar, J.; Tinoco, H. A.; Chlupová, A; Kruml, T. (2017a). Development of the bulge test equipment for measuring mechanical properties of thin films", In: Proceedings of 26th International Conference on Metallurgy and Materials. Brno, Czech Republic. pp. 1-6. Brno, Czech Republic. (2017, May).

Holzer, J., Pikálek, T., Buchta, Z., Lazar, J., Tinoco H.A., Chlupová, A., Náhlík, L., Sobota, J., Fořt, T., Kruml, T. (2017b). Detecting Plasticity in al Thin Films by Means of Bulge Test, In: 16 Conference on Coating and Layers 2017, pp. 1-6. 23. Brno, Czech Republic. (2017, Oct).

Hosokawa, H., Desai, A. V., & Haque, M. A. (2008). Plane stress fracture toughness of freestanding nanoscale thin films. Thin Solid Films, 516(18), 6444-6447.

Huang, J. H., Haffey, K., Arefin, A., Akhadov, L. E., Harris, J. F., Iyer, R., & Nath, P. (2018). A microfluidic method to measure bulging heights for bulge testing of polydimethylsiloxane (PDMS) and polyurethane (PU) elastomeric membranes. RSC advances, 8(38), 21133-21138.

Huang, X., & Pelegri, A. A. (2006). Mechanical characterization of thin film materials with nanoindentation measurements and FE analysis. Journal of Composite Materials, 40(15), 1393-1407.

Huang, S., Woodson, M., Smalley, R., & Liu, J. (2004). Growth mechanism of oriented long single walled carbon nanotubes using "fast-heating" chemical vapor deposition process. Nano Letters, 4(6), 1025-1028.

Huang, C. K., Lou, W. M., Tsai, C. J., Wu, T. C., & Lin, H. Y. (2007). Mechanical properties of polymer thin film measured by the bulge test. Thin Solid Films, 515(18), 7222-7226.

Irwin G.R (1968). Linear fracture mechanics, fracture transition, and fracture control. Engineering Fracture Mechanics, 1:2 (1968), 241-257.

Javed, H., Merle, B., Preiß, E., Hivet, R., Benedetto, A., & Göken, M. (2016). Mechanical characterization of metallic thin films by bulge and scratch testing. Surface and Coatings Technology, 289, 69-74.

Kalkman, A. J., Verbruggen, A. H., Janssen, G. C. A. M., & Groen, F. H. (1999). A novel bulge-testing setup for rectangular free-standing thin films. Review of Scientific instruments, 70(10), 4026-4031.

Karimi, A., Shojaei, O. R., Kruml, T., & Martin, J. L. (1997). Characterisation of TiN thin films using the bulge test and the nanoindentation technique. Thin Solid Films, 308, 334-339.

Kraft, O., & Volkert, C. A. (2001). Mechanical testing of thin films and small structures. Advanced Engineering Materials, 3(3), 99-110.

Kim, B. J., & Meng, E. (2015). Review of polymer MEMS micromachining. Journal of Micromechanics and Microengineering, 26(1), 013001.

Kim, K. K., Hsu, A., Jia, X., Kim, S. M., Shi, Y., Hofmann, M., ... & Kong, J. (2011). Synthesis of monolayer hexagonal boron nitride on Cu foil using chemical vapor deposition. Nano letters, 12(1), 161-166.

Kysar, J. W., Saito, Y., Oztop, M. S., Lee, D., & Huh, W. T. (2010). Experimental lower bounds on geometrically necessary dislocation density. International Journal of Plasticity, 26(8), 1097-1123.

Labuz, J. F., & Zang, A. (2012). Mohr–Coulomb failure criterion. Rock mechanics and rock engineering, 45(6), 975-979.

Laconte, J., Iker, F., Jorez, S., André, N., Proost, J., Pardoen, T., ... & Raskin, J. P. (2004). Thin films stress extraction using micromachined structures and wafer curvature measurements. Microelectronic engineering, 76(1-4), 219-226.

Landis, C. M., & McMeeking, R. M. (1999). A shear-lag model for a broken fiber embedded in a composite with a ductile matrix. Composites Science and Technology, 59(3), 447-457.

Larsen, M. B. B. S. (2015). Chemical Vapour Deposition of Large Area Graphene (Doctoral dissertation, DTU Nanotech).

Lau, W. J., Ismail, A. F., Misdan, N., & Kassim, M. A. (2012). A recent progress in thin film composite membrane: A review. Desalination, 287, 190-199.

Lee, H. K., Ko, S. H., Han, J. S., & Park, H. (2007). Mechanical properties measurement of silicon nitride thin films using the bulge test. In Microelectronics: Design, Technology, and Packaging III (Vol. 6798, pp. 337-344). SPIE.

Leskelä, M., & Ritala, M. (2002). Atomic layer deposition (ALD): from precursors to thin film structures. Thin solid films, 409(1), 138-146.

Liang, C., & Prorok, B. C. (2007). Measuring the thin film elastic modulus with a magnetostrictive sensor. Journal of Micromechanics and Microengineering, 17(4), 709.

Lin, Y., Long, S. G., & WANG, Z. H. (2014). Accuracy analysis of plane-strain bulge test for determining mechanical properties of thin films. Transactions of Nonferrous Metals Society of China, 24(10), 3265-3273.

Linder, C., Paratte, L., Gretillat, M. A., Jaecklin, V. P., & De Rooij, N. F. (1992). Surface micromachining. Journal of Micromechanics and Microengineering, 2(3), 122.

Liu, Y., Koep, E., & Liu, M. (2005). A highly sensitive and fast-responding SnO2 sensor fabricated by combustion chemical vapor deposition. Chemistry of materials, 17(15), 3997-4000.

Liu, B., Fathi, M., Chen, L., Abbas, A., Ma, Y., & Zhou, C. (2015). Chemical vapor deposition growth of monolayer WSe2 with tunable device characteristics and growth mechanism study. ACS nano, 9(6), 6119-6127.

Lu, T., Chen, C., Zhao, K., Zhang, W., & Wang, T. J. (2013). Bulge test at nano-scale: The surface effects. Applied Physics Letters, 103(5), 053110.

Maier-Schneider, D., Maibach, J., & Obermeier, E. (1995). A new analytical solution for the load-deflection of square membranes. Journal of microelectromechanical systems, 4(4), 238-241.

Marandi, F. A., Jabbari, A. H., Sedighi, M., & Hashemi, R. (2017). An Experimental, analytical, and numerical investigation of hydraulic bulge test in two-layer Al–Cu Sheets. Journal of Manufacturing Science and Engineering, 139(3), 031005.

Marchiori, G., Lopomo, N., Boi, M., Berni, M., Bianchi, M., Gambardella, A., ... & Marcacci, M. (2016) Optimizing thickness of ceramic coatings on plastic components for orthopedic applications: A finite element analysis. Materials Science and Engineering: C, 58, 381-388.

Martins, P., Delobelle, P., Malhaire, C., Brida, S., & Barbier, D. (2009). Bulge test and AFM point deflection method, two technics for the mechanical characterisation of very low stiffness freestanding films. The European Physical Journal-Applied Physics, 45(1).

Martins, P., Malhaire, C., Brida, S., & Barbier, D. (2008). On the determination of Poisson's ratio of stressed monolayer and bilayer submicron thick films. In 2008 Symposium on Design, Test, Integration and Packaging of MEMS/MOEMS (pp. 197-200). IEEE.

Matějka, M., Krátký, S., Řiháček, T., Knápek, A., & Kolařík, V. (2020). Functional nano-structuring of thin silicon nitride membranes. Journal of Electrical Engineering, 71(2), 127-130.

Mattevi, C., Kim, H., & Chhowalla, M. (2011). A review of chemical vapour deposition of graphene on copper. Journal of Materials Chemistry, 21(10), 3324-3334.

Mattox, D. M. (2010). Handbook of physical vapor deposition (PVD) processing. William Andrew.
Mehregany, M., Tong, L., Matus, L. G., & Larkin, D. J. (1997). Internal stress and elastic modulus measurements on micromachined 3C-SiC thin films. IEEE Transactions on Electron Devices, 44(1), 74-79.
Mei, H., Huang, R., Chung, J. Y., Stafford, C. M., & Yu, H. H. (2007). Buckling modes of elastic thin films on elastic substrates. Applied Physics Letters, 90(15), 151902.
Merle, B., & Göken, M. (2011). Fracture toughness of silicon nitride thin films of different thicknesses as measured by bulge tests. Acta Materialia, 59(4), 1772-1779.
Merle, B., & Göken, M. (2014). Bulge fatigue testing of freestanding and supported gold films. Journal of Materials Research, 29(2), 267-276.
Min, J., Stoughton, T. B., Carsley, J. E., Carlson, B. E., Lin, J., & Gao, X. (2017). Accurate characterization of biaxial stress-strain response of sheet metal from bulge testing. International Journal of Plasticity, 94, 192-213.
Mitchell, J. S., Zorman, C. A., Kicher, T., Roy, S., & Mehregany, M. (2003). Examination of bulge test for determining residual stress, Young's modulus, and Poisson's ratio of 3C-SiC thin films. Journal of Aerospace Engineering, 16(2), 46-54.
Mitzi, D. B. (2001). Thin-film deposition of organic− inorganic hybrid materials. Chemistry of Materials, 13(10), 3283-3298.
Moharrami, N., & Bull, S. J. (2014). A comparison of nanoindentation pile-up in bulk materials and thin films. Thin Solid Films, 572, 189-199.
Morosanu, C. E. (2016). Thin films by chemical vapour deposition (Vol. 7). Elsevier.
Narvydas, E., & Puodziuniene, N. (2014). Applications of sub-modeling in structural mechanics. In Proceedings of 19th International Conference. Mechanika, Kaunas, Lithuania (pp. 172-6).
Neggers, J., Hoefnagels, J. P., & Geers, M. G. (2012a). On the validity regime of the bulge equations. Journal of materials research, 27(9), 1245-1250.
Neggers, J., Hoefnagels, J. P. M., Hild, F., Roux, S., & Geers, M. G. D. (2012b). A global digital image correlation enhanced full-field bulge test method. Procedia IUTAM, 4, 73-81.
Neggers, J., Hoefnagels, J. P. M., Hild, F., Roux, S., & Geers, M. G. D. (2014). Direct stress-strain measurements from bulged membranes using topography image correlation. Experimental Mechanics, 54(5), 717-727.
Nicola, L., Xiang, Y., Vlassak, J. J., Van der Giessen, E., & Needleman, A. (2006). Plastic deformation of freestanding thin films: experiments and modeling. Journal of the Mechanics and Physics of Solids, 54(10), 2089-2110.
Nix, W. D. (1989). Mechanical properties of thin films. Metallurgical transactions A, 20(11), 2217-2245.
Norman, R. E., Flanagan, J. G., Sigal, I. A., Rausch, S. M., Tertinegg, I., & Ethier, C. R. (2011). Finite element modeling of the human sclera: influence on optic nerve head biomechanics and connections with glaucoma. Experimental eye research, 93(1), 4-12.
Obraztsov, A. N., Obraztsova, E. A., Tyurnina, A. V., & Zolotukhin, A. A. (2007). Chemical vapor deposition of thin graphite films of nanometer thickness. Carbon, 45(10), 2017-2021.
Nuismer, R. J. (1975). An energy release rate criterion for mixed mode fracture. International journal of fracture, 11(2), 245-250.
Ohring, M. (2001). Materials science of thin films. Elsevier.
Oliver, W. C., & Pharr, G. M. (1992). An improved technique for determining hardness and elastic modulus using load and displacement sensing indentation experiments. Journal of materials research, 7(6), 1564-1583.
Orthner, M. P., Rieth, L. W., & Solzbacher, F. (2010). High speed wafer scale bulge testing for the determination of thin film mechanical properties. Review of Scientific Instruments, 81(5), 055111.
Overman, N. R., Overman, C. T., Zbib, H. M., & Bahr, D. F. (2009). Yield and deformation in biaxially stressed multilayer metallic thin films. Journal of engineering materials and technology, 131(4).
Pan, J. Y., Lin, P., Maseeh, F., & Senturia, S. D. (1990). Verification of FEM analysis of load-deflection methods for measuring mechanical properties of thin films. In: Solid-State Sensor and Actuator Workshop, 1990. 4th Technical Digest., IEEE (pp. 70-73).
Paul, O., & Gaspar, J. (2007). Thin-Film Characterization Using the Bulge Test. Reliability of MEMS: Testing of Materials and Devices, 67-121.
Pecholt, B., Vendan, M., Dong, Y., & Molian, P. (2008). Ultrafast laser micromachining of 3C-SiC thin films for MEMS device fabrication. The International Journal of Advanced Manufacturing Technology, 39(3-4), 239-250.
Peckys, Diana B., Gabriel M. Veith, David C. Joy, and Niels De Jonge. (2009). "Nanoscale imaging of whole cells using a liquid enclosure and a scanning transmission electron microscope." PloS one 4, no. 12 (2009): e8214.
Pharr, G. M., Oliver, W. C., & Brotzen, F. R. (1992). On the generality of the relationship among contact stiffness, contact area, and elastic modulus during indentation. Journal of materials research, 7(3), 613-617.

Poelma, R. H., Sadeghian, H., Noijen, S. P. M., Zaal, J. J. M., & Zhang, G. Q. (2011). A numerical experimental approach for characterizing the elastic properties of thin films: application of nanocantilevers. Journal of Micromechanics and Microengineering, 21(6), 065003.

Preiß, E. I., Merle, B., & Göken, M. (2017). Understanding the extremely low fracture toughness of freestanding gold thin films by in-situ bulge testing in an AFM. Materials Science and Engineering: A, 691, 218-225.

Prevost, T. P., Jin, G., De Moya, M. A., Alam, H. B., Suresh, S., & Socrate, S. (2011). Dynamic mechanical response of brain tissue in indentation in vivo, in situ and in vitro. Acta biomaterialia, 7(12), 4090-4101.

Prins, M. W. J., Grosse-Holz, K. O., Müller, G., Cillessen, J. F. M., Giesbers, J. B., Weening, R. P., & Wolf, R. M. (1996). A ferroelectric transparent thin-film transistor. Applied physics letters, 68(25), 3650-3652.

Puma, G. L., Bono, A., Krishnaiah, D., & Collin, J. G. (2008). Preparation of titanium dioxide photocatalyst loaded onto activated carbon support using chemical vapor deposition: a review paper. Journal of hazardous Materials, 157(2-3), 209-219.

Qian, G., González-Albuixech, V. F., Niffenegger, M., & Giner, E. (2016). Comparison of KI calculation methods. Engineering Fracture Mechanics, 156, 52-67.

Reichelt, K., & Jiang, X. (1990). The preparation of thin films by physical vapour deposition methods. Thin solid films, 191(1), 91-126.

Reuber, C., Eisenlohr, P., Roters, F., & Raabe, D. (2014). Dislocation density distribution around an indent in single-crystalline nickel: Comparing nonlocal crystal plasticity finite-element predictions with experiments. Acta Materialia, 71, 333-348.

Rice, J. R. (1968). A path independent integral and the approximate analysis of strain concentration by notches and cracks. Journal of applied mechanics, 35(2), 379-386.

Rontu, V., Nolvi, A., Hokkanen, A., Haeggström, E., Kassamakov, I., & Franssila, S. (2018). Elastic and fracture properties of free-standing amorphous ALD Al2O3 thin films measured with bulge test. Materials Research Express, 5(4), 046411.

Santos, A. D., Teixeira, P., Barata da Rocha, A., & Barlat, F. (2010). On the determination of flow stress using bulge test and mechanical measurement. In AIP Conference Proceedings (Vol. 1252, No. 1, pp. 845-852). American Institute of Physics.

Saraswati, T. S., Sritharan, T., Pang, C. I., Chew, Y. H., Breach, C. D., Wulff, F., ... & Wong, C. C. (2004). The effects of Ca and Pd dopants on gold bonding wire and gold rod. Thin solid films, 462, 351-356.

Schalko, J., Beigelbeck, R., Stifter, M., Schneider, M., Bittner, A., & Schmid, U. (2011). Improved load-deflection method for the extraction of elastomechanical properties of circularly shaped thin-film diaphragms. In Smart Sensors, Actuators, and MEMS V (Vol. 8066, pp. 463-470). SPIE.

Schlenoff, J. B., & Decher, G. (2006). Multilayer thin films: sequential assembly of nanocomposite materials. John Wiley & Sons.

Schweitzer, E. W., & Göken, M. (2007). In situ bulge testing in an atomic force microscope: Microdeformation experiments of thin film membranes. Journal of Materials Research, 22(10), 2902-2911.

Setter, N., Damjanovic, D., Eng, L., Fox, G., Gevorgian, S., Hong, S., ... & Stolitchnov, I. (2006). Ferroelectric thin films: Review of materials, properties, and applications. Journal of applied physics, 100(5), 051606.

Shafqat, S., van der Sluis, O., Geers, M., & Hoefnagels, J. (2018). A bulge test based methodology for characterizing ultra-thin buckled membranes. Thin Solid Films, 660, 88-100.

Shan, Z. W., Mishra, R. K., Asif, S. S., Warren, O. L., & Minor, A. M. (2008). Mechanical annealing and source-limited deformation in submicrometre-diameter Ni crystals. Nature materials, 7(2), 115.

Sheng, J. Y., Zhang, L. Y., Li, B., Wang, G. F., & Feng, X. Q. (2017). Bulge test method for measuring the hyperelastic parameters of soft membranes. Acta Mechanica, 228(12), 4187-4197.

Shih, V. C. Y., Harder, T. A., & Tai, Y. C. (2003). Yield strength of thin-film parylene-C. In Symposium on Design, Test, Integration and Packaging of MEMS/MOEMS 2003. (pp. 394-398). IEEE.

Shojaei, O. R., & Karimi, A. (1998). Comparison of mechanical properties of TiN thin films using nanoindentation and bulge test. Thin Solid Films, 332(1-2), 202-208.

Small, M. K., Daniels, B. J., Clemens, B. M., & Nix, W. D. (1994). The elastic biaxial modulus of Ag–Pd multilayered thin films measured using the bulge test. Journal of materials research, 9(1), 25-30.

Small, M. K., & Nix, W. D. (1992). Analysis of the accuracy of the bulge test in determining the mechanical properties of thin films. Journal of materials research, 7(6), 1553-1563.

Stoney, G. G. (1909). The tension of metallic films deposited by electrolysis. Proceedings of the Royal Society of London. Series A, Containing Papers of a Mathematical and Physical Character, 82(553), 172-175.

Tabata, O., Kawahata, K., Sugiyama, S., & Igarashi, I. (1989). Mechanical property measurements of thin films using load-deflection of composite rectangular membranes. Sensors and actuators, 20(1-2), 135-141.

Tabata, O. & Tsuchiya, T. (1996). Poisson's ratio evaluation of LPCVD silicon nitride film, IEEJ Transactions on Sensors and Micromachines. 116(1) (1996) 34-35. https://doi.org/10.1541/ieejsmas.116.34

Timoshenko, S., & Woinowsky-Krieger, S. (1959). Theory of plates and shells (Vol. 2, pp. 240-246). New York: McGraw-hill.

Tinoco, H. A., Serpa, A. L., & Ramos, A. M. (2010). Numerical study of the effects of bonding layer properties on electrical signatures of piezoelectric sensors. Mecánica Computacional, 29(86), 8391-8409.

Tinoco, H. A.; Holzer, J.; Pikálek, T.; Buchta, Z.; Lazar, J.; Alice, C.; Kruml, T. (2018a). "Estimation of Mechanical Parameters of Thin Films Using Finite Element Analysis", In: Proceedings of 20th International Conference of applied Mechanics. Myslovice, Czech Republic. pp. 157-162, April, 2018. DOI http://doi.org/10.31224/osf.io/3adt5

Tinoco, H. A. (2018b). Modeling of piezoelectric sensors adhesively bonded on trusses using a mathematical programming approach. Structural and Multidisciplinary Optimization, 58(3), 903-918.

Tinoco, H. A., Holzer, J., Pikálek, T., Buchta, Z., Lazar, J., Chlupová, A., ... & Hutař, P. (2019). Determination of elastic parameters of Si3N4 thin films by means of a numerical approach and bulge tests. Thin Solid Films, 672, 66-74.

Tinoco, H. A., Hutař, P., Merle, B., Göken, M., & Kruml, T. (2020). Fracture toughness evaluation of a cracked Au thin film by applying a finite element analysis and bulge test. In Key Engineering Materials (Vol. 827, pp. 196-202). Trans Tech Publications Ltd.

Uchic, M. D., Dimiduk, D. M., Florando, J. N., & Nix, W. D. (2002). Exploring specimen size effects in plastic deformation of Ni 3 (Al, Ta). MRS Online Proceedings Library Archive, 753

Ventsel, T. Krauthammer, T. (2001). Thin plates and shells: theory: analysis, and applications. CRC press, 2001.

Vlassak, J. J., & Nix, W. D. (1992). A new bulge test technique for the determination of Young's modulus and Poisson's ratio of thin films. Journal of Materials Research, 7(12), 3242-3249.

Vucetic, M., Bouguecha, A., Peshekhodov, I., Götze, T., Huinink, T., Friebe, H., ... & Behrens, B. A. (2011). Numerical validation of analytical biaxial true stress—true strain curves from the bulge test. In AIP Conference Proceedings (Vol. 1383, No. 1, pp. 107-114).

Walmsley, B. A., Liu, Y., Hu, X. Z., Bush, M. B., Dell, J. M., & Faraone, L. (2007). Poisson's ratio of low-temperature PECVD silicon nitride thin films. Journal of Microelectromechanical Systems, 16(3), 622-627.

Wang, H. W., Kang, Y. L., Zhang, Z. F., & Qin, Q. H. (2003). Size effect on the fracture toughness of metallic foil. International Journal of Fracture, 123(3-4), 177-185.

Wang, X., Gong, Y., Shi, G., Chow, W. L., Keyshar, K., Ye, G., ... & Tay, B. K. (2014). Chemical vapor deposition growth of crystalline monolayer MoSe2. ACS nano, 8(5), 5125-5131.

Wang, J., Yang, C., & Hodgson, P. D. (2016). Strain gradients in Cu–Fe thin films and multilayers during micropillar compression. Materials Science and Engineering: A, 651, 146-154.

Wei, Z., Zhang, G., Chen, H., Luo, J., Liu, R., & Guo, S. (2009). A simple method for evaluating elastic modulus of thin films by nanoindentation. Journal of Materials Research, 24(3), 801-815.

Xiang, Y., Chen, X., & Vlassak, J. J. (2005). Plane-strain bulge test for thin films. Journal of materials research, 20(9), 2360-2370.

Xiang, Y., & Vlassak, J. J. (2006). Bauschinger and size effects in thin-film plasticity. Acta Materialia, 54(20), 5449-5460.

Xiao, Y., Wehrs, J., Ma, H., Al-Samman, T., Korte-Kerzel, S., Göken, M., ... & Wheeler, J. M. (2017). Investigation of the deformation behavior of aluminum micropillars produced by focused ion beam machining using Ga and Xe ions. Scripta Materialia, 127, 191-194.

Xu, Z. H., & Rowcliffe, D. (2004). Finite element analysis of substrate effects on indentation behaviour of thin films. Thin Solid Films, 447, 399-405.

Xu, D., & Liechti, K. M. (2010). Bulge testing transparent thin films with moiré deflectometry. Experimental mechanics, 50(2), 217-225.

Yanfei, C., Shigang, A., Jingda, T., Yongmao, P., Liqun, T., & Daining, F. (2017). Characterizing the viscoelastic properties of hydrogel thin films by bulge test. Journal of Applied Mechanics, 84(6), 061005.

Yang, J., Gaspar, J., & Paul, O. (2008). Fracture Properties of LPCVD Silicon Nitride and Thermally Grown Silicon Oxide Thin Films From the Load-Deflection of Long $\hbox {Si} _ {3}\hbox {N} _ {4} $ and $\hbox {SiO} _ {2}/\hbox {Si} _ {3}\hbox {N} _ {4} $ Diaphragms. Journal of microelectromechanical systems, 17(5), 1120-1134.

Youssef H. (2011). Développement d'un banc de test par gonflement de membranes destiné à la caractéri- sation mécanique de matériaux déposés en films minces. Micro et nanotechnologies/Microélectronique. Université Paul Sabatier - Toulouse III, 2011. Français.

Youssef, H., Ferrand, A., Calmon, P., Pons, P., & Plana, R. (2010). Methods to improve reliability of bulge test technique to extract mechanical properties of thin films. Microelectronics Reliability, 50(9-11), 1888-1893.

Zhang, Rongjing (2006). Mechanical characterization of thin films with application to ferroelectrics. Dissertation (Ph.D.), California Institute of Technology.

Zhang, Y. (2008). Extended Stoney's Formula for a Film-Substrate Bilayer With the Effect of Interfacial Slip. ASME. Journal of Applied Mechanics. 75(1): 011008.

Zhang, J. J., Sun, Y. Y., Li, D. S., Cao, Y., Wang, Z., Ma, J., & Zhao, G. Z. (2015). Modeling the mechanics of graphene-based polymer composite film measured by the bulge test. Journal of Physics D: Applied Physics, 48(42), 425302.

Zhang, Y. (2016). Large deflection of clamped circular plate and accuracy of its approximate analytical solutions. Science China Physics, Mechanics & Astronomy, 59(2), 1-11.

Zhao, C., Lavasan, A. A., & Schanz, T. (2019). Application of submodeling technique in numerical modeling of mechanized tunnel excavation. International Journal of Civil Engineering, 17(1), 75-89.

Zheng, Z., Sun, W., Suo, X., Wong, L. L., Sun, Z., & Yeow, J. T. (2015). A novel deflection shape function for rectangular capacitive micromachined ultrasonic transducer diaphragms. Sensing and bio-sensing research, 5, 62-70.

Zhou, W., Yang, J., Sun, G., Liu, X., Yang, F., & Li, J. (2008). Fracture properties of silicon carbide thin films by bulge test of long rectangular membrane. Journal of Microelectromechanical Systems, 17(2), 453-461.